Photo- and thermally-induced electronic and structural dynamics in perovskites and transition metal oxides

Oliviero CANNELLI

EPFL

■ École
polytechnique
fédérale
de Lausanne

2021

A Silvia

Acknowledgements

First of all, I would like to sincerely thank my thesis advisor Prof. Majed Chergui, for welcoming in his group and for giving me the opportunity to travel across the world facing challenging experiments and make great science. He has always transmitted serenity and enthusiasm for our research, perhaps the two most desirable qualities to build a working environment where to harvest human and scientific exchanges. Another very special thank goes to my co-supervisor Prof. Giulia Fulvia Mancini for her close supervision during these years. She made me grow from both a personal and a professional point of view, making me an "adult" scientist.

I am grateful to Dr. Nicola Colonna, not only for the wonderful work he did, but also for the patience and the perseverance he demonstrated during these years for our lead halide perovskites projects. I would like to thank our collaborators Prof. Julia Wiktor and Prof. Alfredo Pasquarello for performing molecular dynamics calculations, and Dr. Franziska Krieg and Prof. Maksym V. Kovalenko for providing excellent quality perovskite samples. Thank also to Dr. Natacha Ohannessian and Dr. Daniele Pergolesi for growing our wonderful Co_3O_4 thin films, which we have been measuring with all possible spectroscopic techniques with considerable satisfaction.

In the numerous X-ray beamtimes I joined, I had the chance to collaborate with many great scientists all across the world. I would like to thank Dr. Daniel Grolimund, Dr. Grigory Smolentsev, Dr. Tetsuo Katayama, Dr. Anne Marie March, Dr. Gilles Doumy, Dr. Andre Al Haddad, Dr. Frederico A. Lima, Dr. Wojciech Gawelda, Dr. Dmitry Khakhulin, Dr. Claudio Cirelli, Dr. Gregor Knopp. Among them a special thank goes to Dr. Christopher J. Milne, who initiated me to the secrets of the high repetition rate DAQ at the SLS, which represented my first contact with the X-ray world.

Even though I was officially based in Lausanne during my PhD, most of my scientific activity consisted in beamtimes at X-ray large scale facilities. These experiments were extremely challenging from a technical point of view and had to be performed under a significant amount of stress. None of them would have been successful without a formidable team to

Abstract

The interactions between the correlated degrees of freedom in a system determine its structure and function. The mechanisms driving these couplings can be investigated upon a controlled perturbation of the environment, using time-resolved experiments to monitor over time the systems' evolution towards its original state. These methods employ an ultrashort laser pulse to excite a material into an out-of-equilibrium state and a second pulse to probe its configuration at a defined time delay. Multiple spectroscopic techniques can be combined together to provide a comprehensive picture of the interacting forces acting at the microscopic level.

In this thesis, we exploited optical and X-ray pump-probe methods in a synergistic approach to study the interplay of the electronic, spin and structural degrees of freedom in two class of complex systems relevant for solar energy conversion applications: lead-halide perovskites and transition metal oxides.

$CsPbBr_3$ perovskites are promising optoelectronic materials characterized by a flexible ionic inorganic network that strongly interacts with the charge carriers. Upon photoexcitation, the lattice response leads to the polaronic distortions affecting the optical properties of the system. In our study, we combined time-resolved X-ray absorption spectroscopy and accurate simulations to quantify the structural deformations induced in the lattice through electron-phonon coupling. Complementing our pump-probe results with temperature-dependent X-ray absorption measurements, we disentangled the photodynamics of the system from thermally-induced effects. Additionally, we clarified the thermal response of $CsPbBr_3$ comparing temperature-dependent X-ray investigations with first principles computations. A consistent atomic level picture is provided, in which the role of thermal fluctuation and phonon anharmonicity are rationalized with the experimental evidence.

Spinel Co_3O_4 represents a model system for the investigation of the correlated electronic-spin-nuclear degrees of freedom in transition metal oxides. By combining femtosecond broadband reflectivity and ultrafast time-resolved X-ray emission spectroscopy, we monitored the material's photoresponse upon selective excitations of the ligand-to-metal and metal-to-metal charge transfer optical transitions. In the former case, sub-picosecond spin and electronic

Abstract

dynamics occurs together with a displacive excitation of coherent phonons, in the latter a slower electronic relaxation is measured in presence of impulsively stimulated Raman scattering phonons. We propose a possible explanation in terms of excitation-selective ultrafast intersystem crossing. We also present the preparation of parallel time-resolved X-ray emission and X-ray diffraction experiments, which will harness the structural- and spin-sensitivity of these techniques to disentangle the interactions determining the photodynamics of the system.

In the last part of the thesis, we show a preliminary study aiming at extending the temperature-jump pump-probe method to the X-ray domain. In this experiment, a near-infrared pump is used to vibrationally excite the water molecules of the solvent, which undergo ultrafast relaxation causing a sudden increase of the temperature in the bulk of the solution. This process triggers a thermal chemical reaction of the dissolved solutes, which is monitored in a time-resolved fashion. We studied a multistep ligand substitution reaction of a hexacoordinated Cobalt ion complex in chlorinated water solution, showing the great sensitivity of the X-ray absorption technique to subtle structural changes. This work opens new perspectives for the investigation of thermally-driven reactions with element-selective and site-specific X-ray methods.

Keywords: ultrafast X-ray spectroscopy, temperature dependent X-ray spectroscopy, temperature dependent X-ray diffraction, ultrafast optical spectroscopy, temperature jump, polarons, electron-phonon coupling, inorganic lead-halide perovskites, spinel cobalt oxide

Sommario

Le interazioni tra i gradi di libertà interagenti all'interno di un sistema ne deteminano la struttura ed il suo funzionamento. I meccanismi che causano questi accoppiamenti possono essere studiati attraverso una controllata perturbazione dell'ambiente, utilizzando esperimenti risolti nel tempo per monitorare l'evoluzione temporale del sistema verso il suo stato originario. Questi metodi impiegano un impulso laser ultrabreve per portare un materiale in uno stato di non-equilibrio e un secondo impulso per sondarne la configurazione ad un ritardo temporale definito con precisione. Per ottenere una descrizione microscopica completa delle forze interagenti nel sistema è possibile e auspicabile combinare diverse tecniche spettroscopiche.

In questa tesi abbiamo sfruttato dei metodi *pump-probe* nell'ottica e nei raggi X con un approccio sinergico, al fine di studiare l'influenza reciproca dei gradi di libertà elettronici, di spin e nucleari in due classi di materiali particolarmente complessi che trovano applicazioni nell'ambito della conversione dell'energia solare: le perovskiti piombo-alogeno e gli ossidi di metalli di transizione.

Le perovskiti $CsPbBr_3$ sono dei promettenti materiali optoelettronici caratterizzati da una struttura inorganica ionica molto flessibile, che interagisce fortemente con i portatori di carica. A seguito di una fotoeccitazione, la risposta del reticolo porta a distorsioni polaroniche che influenzano le proprietà ottiche del sistema. Nei nostri studi abbiamo associato spettroscopia di assorbimento X risolta nel tempo con delle simulazioni molto accurate per quantificare le deformazioni strutturali indotte nel reticolo attraverso effetti di accoppiamento elettrone-fonone. Unendo i risultati dell'indagine *pump-probe* con misure di assobimento X in funzione della temperatura siamo riusciti a distinguere gli effetti della fotodinamica del sistema da quelli puramente termici. Inoltre, attraverso un confronto tra misure con i raggi X in funzione della temperatura e calcoli teorici *ab-initio* abbiamo fatto chiarezza sulla natura della risposta termica nel $CsPbBr_3$. Ne risulta uno scenario microscopico coerente in cui si riescono a spiegare il ruolo delle fluttuazioni termiche e dell'anarmonicità dei fononi sulle osservabili sperimentali.

Sommario

Il Co$_3$O$_4$ con struttura a spinello costituisce un sistema modello per lo studio dei tre gradi di libertà interagenti elettronici, di spin e nucleari all'interno della famiglia degli ossidi di metalli di transizione. In questa indagine abbiamo seguito la risposta fotoindotta del sistema a seguito di eccitazioni selettive delle transitioni di tipo trasferimento di carica ligando-metallo e metallo-metallo con tecniche congiunte di riflettivita' ultraveloce ad ampio spettro e spettroscopia di emissione X risolta nel tempo. Nel primo caso abbiamo osservato una rapida dinamica elettronica e di spin al di sotto del picosecondo, accompagnata da oscillazioni coerenti legate alla generazione di un fonone di tipo displacivo. Nel secondo caso abbiamo misurato una risposta elettronica più lenta in presenza di un fonone attivato per effetto Raman impulsato. Per spiegare queste osservazioni abbiamo proposto la presenza di un processo di *intersystem crossing* ultrarapido e selettivo rispetto al tipo di eccitazione elettronica. Abbiamo inoltre riportato la preparazione di esperimenti di diffrazione a raggi X e assorbimento X risolti nel tempo da condurre in simultanea per sfruttare al meglio la sensibilita' strutturale e di spin di queste tecniche, e per separare i contributi delle varie interazioni che guidano la fotodinamica del sistema.

Nella parte finale della tesi, presentiamo uno studio preliminare volto ad estendere la tecnica *pump-probe* del salto di temperatura nel dominio dei raggi X. In questa tipologia di esperimento si utilizza un impulso nel vicino infrarosso per eccitare vibrazionalmente delle molecole d'acqua che costituiscono il solvente della soluzione sotto indagine. Queste ultime seguono un processo di rilassamento ultraveloce che comporta un aumento improvviso della temperatura della soluzione stessa. Tale processo stimola l'inizio di una reazione termica tra i soluti disciolti in soluzione che viene seguita con tecniche risolte nel tempo. Nello specifico abbiamo studiato una reazione di sostituzione multipla dei ligandi su complessi di cobalto esacoordinati in una soluzione d'acqua clorurata, dimostrando che la tecnica di assobimento X riesce a monitorare con precisione anche modeste variazioni strutturali. Nel suo insieme questo lavoro getta le basi per futuri studi sulle reazioni termicamente indotte con metodi nei raggi X che sondano selettivamente gli elementi ed i siti da investigare.

Parole chiave: spettroscopia a raggi-X ultraveloce, spettroscopia a raggi-X dipendente dalla temperatura, diffrazione a raggi-X dipendente dalla temperatura, spettroscopia ottica ultraveloce, salto di temperatura, polaroni, accoppiamento elettrone-fonone, perovskiti piombo-alogeno inorganiche, ossido di cobalto spinello

Contents

List of Figures

List of Tables

List of Acronyms

ADC	Analog-to-Digital Converter
APS	Advanced Photon Source
ARPES	Angle-Resolved Photoelectron Spectroscopy
BBO	β-barium Borate
CAP	Coherent Acoustic Phonon
CB	Conduction Band
CMOS	Complementary Metal-Oxide-Semiconductor
CXRO	Center for X-Ray Optics
DECP	Displacive Excitation of Coherent Phonons
DFT	Density Functional Theory
DOS	Density Of States
EXAFS	Extended X-ray Absorption Fine Structure
EXFEL	European X-ray Free Electron Laser
FA$^+$	Formamidinium
FEL	Free Electron Laser
FT	Fourier Transform
FWHM	Full Width at Half Maximum
FXE	Femtosecond X-ray Experiments
GLA	Global Lifetime Analysis
GSB	Ground State Bleach
GVD	Group Velocity Dispersion
HAADF-STEM	High-Angle Annular Dark-Field Scanning Transmission Electron Microscopy
HERIX	High Energy Resolution Inelastic X-ray Scattering
HHG	High Harmonic Generation
IR	Infrared
IRF	Instrument Response Function
ISC	Intersystem Crossing
ISRS	Impulsive Stimulated Raman Scattering
LMCT	Ligand-to-Metal Charge Transfer
LO	Longitudinal Optical
MA$^+$	Methylammonium
MD	Molecular Dynamics
MMCT	Metal-to-Metal Charge Transfer

List of Acronyms

NC	Nanocrystal
NIR	Near-Infrared
NOPA	Non-collinear Optical Parametric Amplifier
PA	Photoinduced Absorption
PBE	Perdew-Burke-Ernzerhof
PDF	Pair Distribution Function
p-DOS	projected Density Of States
PES	Potential Energy Surface
PL	Photoluminescence
PSI	Paul Scherrer Institute
RT	Room Temperature
SASE	Self-Amplified Spontaneous Emission
SDD	Silicon Drift Detector
SLS	Swiss Light Source
SNR	Signal-to-noise Ratio
SPC	Single Photon Counting
TEM	Transmission Electron Microscopy
TFY	Total Fluorescence Yield
TMO	Transition Metal Oxide
TRR	Time-Resolved Reflectivity
TR-XAS	Time-Resolved X-ray Absorption Spectroscopy
TR-XES	Time-Resolved X-ray Emission Spectroscopy
TR-XRD	Time-Resolved X-ray Diffraction
T-jump	Temperature jump
UV	Ultraviolet
VB	Valence Band
XANES	X-ray Absorption Near Edge Structure
XAS	X-ray Absorption Spectroscopy
XCH	Excited-Electron Plus Core-Hole
XES	X-ray Emission Spectroscopy
XRD	X-ray Diffraction
XRS	X-ray Solution Scattering
XUV	Extreme Ulatraviolet

Introduction

The understanding of a natural system entails the investigation of its function, which is intimately related to the temporal evolution of its structure. The driving force of an operating system is the presence of an external perturbation, which triggers dynamical processes among its correlated degrees of freedom, attempting to restore the thermodynamic equilibrium. As such, the comprehension of the fundamental interactions that underlie the response of a system to external stimuli represents an essential step towards realizing its control at the microscopic level.

The optimization and manipulation of the properties of a material upon optical excitation is at the heart of the technological development of semiconductor-based devices in the fields of photoelectrochemistry, photodetection and solar energy conversion. The actual implementation of a device requires an in-depth knowledge of the coupled degrees of freedom that ultimately lead to the generation, relaxation, and recombination of the charge carriers by absorption of light. To date, traditional covalent semiconductors such as silicon represent the standard reference not only for electronic chips but also for sensing and photovoltaic applications, thanks to the intense effort in understanding their fundamental physics and to the corresponding technological development. In the field of energy-conversion systems, emerging alternatives to these materials, which require expensive preparation and purification methods, are lead-halide perovskites and transition metal oxides.

These two families are characterized by a remarkable complexity due to a rich chemical composition and to a nature of their chemical bonds, which is intermediate between covalent and ionic. The latter implies the presence of strong electron-phonon coupling, which significantly influences the materials' photodynamics. In lead-halide crystals, the lattice flexibility of the inorganic framework and the pronounced anharmonicity of the soft lead-halide bonds makes the perovskite structural response upon external perturbations of primary importance. In the case of transition metal oxides, the co-presence of ionic bonds and localized d-orbitals on metallic centres generates two different electronic gaps. These insulators are defined as

charge-transfer or Mott-Hubbard whether the smallest gap corresponds to a charge transfer excitation between anions and metals, or a d-d electronic transition localized on the metallic centres.

For these complex systems, a comprehensive description of their photophysics calls for combined investigations of the correlated electronic, spin and structural responses. In this framework, synergistic approaches should combine techniques sensitive to electronic and collective excitations of the material, with element-selective methods to investigate local structural distortions and electronic and spin changes on specific sites. Spectroscopic techniques represent valuable investigation tools, relying on the quantum interaction between light and matter. In the steady-state implementation, they provide microscopic scale information on the time-averaged properties of a material. However, the study of dynamical phenomena requires accessing the time evolution of the spectroscopic observables, disentangling along the time dimension degenerate processes acting on different time scales. A powerful strategy to access the ultrafast dynamics of semiconductor materials consists in the so-called pump-probe method, in which an ultrashort laser pulse brings the system out-of-equilibrium and a second pulse monitors, at a controlled time delay, its relaxation towards the original equilibrium. When implemented in a broadband fashion, time-resolved spectroscopies allow to probe competing nondegenerate processes that act simultaneously in the material.

In this thesis, tabletop time-resolved optical spectroscopy and large scale facilities X-ray studies are combined to get a better understanding of the fundamental interactions in two complex semiconductors that are respectively promising for optoelectronic and photoelectrochemical applications: $CsPbBr_3$ perovskites and spinel Co_3O_4.

In $CsPbBr_3$ perovskites, the light-induced generation of photocarriers determines significant crystal distortions related to polaron formation on ultrafast time scales. On the other hand, the thermal activation of the lattice vibrations causes a modulation of their optoelectronic properties. Combining temperature-dependent X-ray techniques, such as X-ray diffraction and X-ray absorption spectroscopy, with time-resolved X-ray absorption spectroscopy, we mapped the lattice dynamics of $CsPbBr_3$ nanocrystals upon thermal and light perturbation, bringing a deeper understanding of the perovskite's response upon external stimuli. Co_3O_4 is a transition metal oxide with a spinel structure, in which the lattice stoichiometry dictates the presence of two different oxidation states for the Cobalt ions (Co^{2+} and Co^{3+}), respectively in tetrahedral and octahedral configurations. These local symmetries imply two different crystal field splittings for the Cobalt sites and different electronic occupations and spin states. This configuration produces a rich optical spectrum which reflects the complexity of the correlated degrees of freedom of the system, determining the presence of Mott and charge-transfer gaps close in energy. We employed femtosecond broadband visible spectroscopy and time-resolved X-ray emission spectroscopy to inspect the electronic, spin and nuclear responses of Co_3O_4 thin films upon different pump wavelengths, observing that the relaxation pathways are strongly dependent on the specific electronic transition.

Finally, in this thesis we show a first attempt at extending pump-probe X-ray spectroscopic techniques to the investigation of non-light-driven chemical reactions. Specifically, we present a proof-of-principles experiment that combines the temperature-jump method with a X-ray

absorption spectroscopy probe at the Co K-edge to follow the time evolution of a ligand substitution reaction in water solution. This represents an unexplored field for studying thermal phenomena in a time-resolved fashion at synchrotrons and Free-electron lasers. The element-selectivity and structural-, electronic- and spin-sensitivity of X-ray spectroscopic techniques would bring an unprecedented level of detail on the mechanisms of non-light-driven processes in water solution, which represent the large majority in Nature.

The thesis structure brings the reader through the scientific projects on $CsPbBr_3$ nanocrystals, Co_3O_4 thin films and Cobalt complexes in water solution. The description of the experimental methods, which represent challenging but established state-of-the-art techniques, is directly provided in the chapters where they were exploited.

Chapter 1 focuses on the light-induced response of ligand-stabilized $CsPbBr_3$ nanocrystals in toluene solution. The photodriven electronic and nuclear changes in the picosecond and nanosecond regime were mapped with time-resolved X-ray absorption spectroscopy at the Br K- and Pb L_3-edges. We quantified with atomic-level precision the photoinduced structural changes caused by the polaron formation, thanks to refined *ab-initio* simulations accurately reproducing the experiment. Combining time-resolved investigations with temperature-dependent X-ray absorption spectroscopy studies, we ruled out dominant photothermal effects as the primary source of the structural distortions. The photodynamics of the system shows a simultaneous decay of the transient signals around the Br and Pb sites, which occurs without intermediate states. We interpreted the results in terms of charge carrier recombination, which unlocks the structural distortion of the lattice caused by the electron-phonon coupling between the photocarriers and the polar lattice, clarifying the perovskite response under light-induced out-of-equilibrium conditions.

Chapter 2 provides a comprehensive molecular scale description of the thermal dynamics of $CsPbBr_3$ dry nanocrystals across its phase diagram. We performed parallel temperature-dependent powder diffraction and X-ray absorption spectroscopy steady-state measurements at the Br K-edge, monitoring the long- and short-range responses of the lead-halide lattice. The direct comparison of the experiments with *ab-initio* MD simulations shows for the first time that the $CsPbBr_3$ X-ray diffraction pattern changes upon temperature rise are related to dynamical disorder rather than to a symmetry increase of the crystal. This observation is confirmed with the X-ray absorption spectroscopy local structural characterization of the nanocrystals, which locally deviates both from an orthorhombic and a cubic symmetry. The structural changes predicted by the theory across the phase transitions are rationalized in terms of temperature-dependent phonon anharmonicity effects, offering a unified picture of the lead-halide lattice thermal response, which was still missing. The results discussed in Chapters 1 and 2 provide insights on the mechanisms underlying light and thermal activation of $CsPbBr_3$, offering different strategies to control its vibrational degrees of freedom with external stimuli.

In Chapter 3 we studied the photophysics of spinel Co_3O_4 thin films. A femtosecond broadband reflectivity set-up in the visible was implemented and transient measurements were performed pumping the system at 400 nm and 800 nm, respectively exciting the ligand-to-metal charge transfer and the metal-to-metal charge transfer transitions. We observe strongly

different pathways in the ultrafast incoherent electronic dynamics and in the associated co-herent nuclear lattice response, suggesting that optical control of the Co_3O_4 charge carrier relaxation can be implemented upon selective above-band gap excitations. Additionally, we present preparation and preliminary results of a combined X-ray emission spectroscopy and time-resolved X-ray diffraction measurement campaign on Co_3O_4 performed at the European X-ray free electron laser. Upon 400 nm excitation, the element-selectivity and spin-sensitivity of X-ray emission spectroscopy was exploited to track the spin state of the Cobalt centres during the electronic relaxation process of the system.

In Chapter 4 we report the results of a proof-of-principles temperature-jump/X-ray absorption spectroscopy probe experiment at the Co K-edge on Cobalt ions in chlorinated water solution. The 1064 nm pump excites the overtone of the water solvent vibrational levels, which dissipate their energy on ultrafast time scales inducing a temperature change of the irradiated bulk solution. The sudden temperature change launches a multistep substitution chemical reaction of water molecules with the chlorinated ions dissolved in solution. Fingerprints of the reaction intermediates are identified, paving the way for the extension of the temperature-jump method with structural-sensitive and element-selective probes.

Finally, the conclusions of this thesis are drawn, presenting the perspectives that these studies open for the investigated systems and for the X-ray research field.

1 Quantifying photoinduced polaronic distortions in inorganic lead halide perovskites nanocrystals

1.1 Abstract

The development of next generation perovskite-based optoelectronic devices relies critically on the understanding of the interaction between charge carriers and the polar lattice in out-of-equilibrium conditions. While it has become increasingly evident for $CsPbBr_3$ perovskites that the Pb-Br framework flexibility plays a key role in their light-activated functionality, the corresponding local structural rearrangement has not yet been unambiguously identified. In this work, we demonstrate that the photoinduced lattice changes in the system are due to a specific polaronic distortion, associated with the activation of a longitudinal optical phonon mode at 18 meV by electron-phonon coupling, and we quantify the associated structural changes with atomic-level precision. Key to this achievement is the combination of time-resolved and temperature-dependent studies at Br K-edge and Pb L_3-edge X-ray absorption with refined *ab-initio* simulations, which fully account for the screened core-hole final state effects on the X-ray absorption spectra. From the temporal kinetics, we show that carrier recombination

reversibly unlocks the structural deformation at both Br and Pb sites. The comparison with the temperature-dependent XAS results rules out thermal effects as the primary source of distortion of the Pb-Br bonding motif during photoexcitation. Our work provides a comprehensive description of the $CsPbBr_3$ perovskites photophysics, offering novel insights on the light-induced response of the system and its exceptional optoelectronic properties.

1.2   Introduction

Lead halide perovskites are rapidly emerging as excellent candidates for optoelectronic applications, such as photovoltaics, light-emitting diodes [8], lasers [9], photodetectors [10], polariton devices [11] and quantum light sources [12], thanks to their outstanding performances and low fabrication costs [13]. These materials are characterized by facile processing routes, leading to defect-tolerant systems with widely tuneable band gaps, high photoluminescence (PL) quantum yields and narrow emission lines. Their potential stems from their extraordinarily long carrier lifetimes and diffusion lengths [14; 15], which are in apparent contrast with previously reported low charge mobility [16] and lattice dynamical disorder [17]. The $APbX_3$ perovskite structure comprises a Pb-X (X=Cl$^-$, Br$^-$, I$^-$) inorganic framework made of flexible corner-sharing octahedra, with Pb^{2+} cations surrounded by six halide anions, characterized by low-frequency phonons and a pronounced anharmonicity [18–20]. The A^+ cations, either inorganic (Cs^+) or organic (methylammonium, MA^+, or formamidinium, FA^+), fill the voids between PbX_6 octahedra. Distinct orthorhombic, tetragonal and cubic phases were identified in these systems, with phase transition temperatures varying with the cation composition [21–24]. In $CsPbBr_3$ nanocrystals (NCs), the phase diagram is characterized by a room temperature orthorhombic $Pnma$ crystalline group, with a transition to a tetragonal $P\frac{4}{m}bm$ group between 50 °C and 59 °C, and a higher temperature transition to a cubic $Pm\bar{3}m$ group between 108 °C and 117 °C [21].

Recent temperature-dependent studies showed competitive mechanisms underlying the thermal response in lead halide perovskites. Pair distribution function (PDF) analysis from X-ray powder diffraction in organic perovskites at room temperature showed significant internal local distortions of the PbX_6 octahedra [25]. The degree of these distortions was shown to increase with the temperature in $MAPbBr_3$ [26]. In $CsPbX_3$ NCs, structural defectiveness was revealed and ascribed to twin boundaries, whose density increases with temperature and leads to an apparent higher-symmetry structure that does, however, not correspond to the $Pm\bar{3}m$ cubic phase [19]. High energy resolution inelastic X-ray scattering and PDF studies on $MAPbI_3$ pointed to the presence of thermally-active anharmonic soft modes at 350 K [18], and local polar fluctuations among different non-cubic structures were confirmed in a low-frequency Raman study on $MAPbBr_3$ and $CsPbBr_3$ perovskites [27].

The peculiar lattice flexibility of lead halide perovskites also critically underpins their photodynamics. Time-resolved optical studies were conducted to understand key aspects of the early dynamics of the system [28–30]. Several works suggested the presence of polarons, *i.e.* charge

carriers dressed by lattice distortions, in order to explain the time-resolved optical signals [20; 31–34] and transport properties [35]. The polaron formation was shown to generally occur through the Fröhlich mechanism [36], which corresponds to a Coulomb interaction between the charge carriers and the macroscopic electric field created by the activation of longitudinal optical (LO) phonons [37; 38].

Although the polaron hypothesis was frequently inferred to rationalize experimental observations in both organic and inorganic perovskites, the quantification of the associated local structural rearrangement is still missing. In hybrid organic-inorganic lead-halide perovskites, local distortions around the Pb [39] and Br [40] sites were separately reported in time-resolved X-ray absorption spectroscopy (TR-XAS) studies and ascribed to polaron formation, but an unambiguous identification of the associated structural fingerprint was not provided. Ultrafast electron diffraction on a $MAPbI_3$ thin film showed evidence of local rotational disorder of the PbI_6 octahedra arising from optical excitation, as a consequence of hot carrier-phonon coupling [41]. Only recently, was the presence of a dynamically expanding polaronic strain structurally identified in $MAPbBr_3$ single crystal with time-resolved diffusive X-ray scattering [42]. In all-inorganic lead halide perovskites the picture is still unclear. In a previous TR-XAS study of photoexcited $CsPbBr_3$ and $CsPb(BrCl)_3$ NCs at the Br K-, Pb L_3-, and Cs L_2-edges [43] carried out at a synchrotron, it was suggested that hole polarons form within the time resolution of the experiment (≤ 100 ps), around Br centres, with the halide ion turning into a neutral halogen, while electrons would be delocalized in the conduction band (CB). Additionally, the Cs sites did not show any response to photoexcitation. In a more recent time-resolved X-ray diffraction study (TR-XRD) at similar fluences, namely between 2.5 mJ/cm^2 and 12 mJ/cm^2, the lattice response upon photoexcitation was interpreted in terms of transient amorphization from a crystalline structure [2]. In both studies, however, the local structural distortion was invoked to rationalize experimental data in a qualitative way, rather than a quantitative one. A recent angle-resolved photoelectron spectroscopy (ARPES) study demonstrated an increase of the hole effective mass in $CsPbBr_3$ single crystals caused by electron-phonon coupling, and identified a specific LO phonon at 18 meV as the most coupled mode with the charge carriers [44].

In this work we demonstrate that, in $CsPbBr_3$ NCs, the 18 meV LO phonon mode is underpinning the structural distortion induced upon photoexcitation and we quantify the polaronic nuclear displacements with atomic precision. Specifically, we conducted a TR-XAS study at the Br K- and Pb L_3- absorption edges and we found that photoexcitation indeed induces polaron formation around Br centres, which also determines the response of Pb centres. We performed band structure calculations in which - to our knowledge for the first time in TR-XAS studies - the possible structural distortions are *a-priori* selected on a physical basis, fully accounting for core-hole final state effects on the XAS spectra. By comparing these accurate simulations to our experimental results, we identify the local PbX_6 octahedra bond distortions that contribute to the polaronic photoresponse. Additionally, we clarify the fundamental difference underlying optical and thermal activation in $CsPbBr_3$ NCs: our temperature-dependent XAS experiments result in quantitatively different spectral modifications compared to the optical activation, thereby excluding heat as the primary source of distortion of the Pb-Br bonding

motif upon photoexcitation.

1.3 Methods

Br K-edge and Pb L_3-edge spectra have been recorded in the pre-edge and the XANES (X-ray absorption near edge structure) regions upon light or thermal activation of $CsPbBr_3$ NCs. The pre-edge region contains bound-bound core-to-valence transitions and is therefore sensitive to the density of unoccupied valence orbitals. The XANES includes the region just above the ionization limit (*i.e.* the edge). It is characterised by single and multiple scattering events of the photoelectron and, hence, it contains information about the bond distances and angles to the nearest-neighbour atoms around the probed site [45; 46]. In its time-resolved implementation, the photoinduced changes of the TR-XAS spectrum reflect transient structural and electronic modifications at the probed sites and in their local environment [47].

The TR-XAS experiments were conducted at the 7ID-D beamline at the Advanced Photon Source (APS) of the Argonne National Laboratory [48; 49]. A schematic representation of this experiment is shown in Figure 1.1. The sample consisted of long-chain zwitterion-capped $CsPbBr_3$ perovskite NCs with cuboidal shape (side length 10±2 nm) and high PL quantum yields [50]. Above band-gap photoexcitation was performed using a Duetto laser at a photon energy of 3.49 eV (*i.e.* 1.1 eV above the direct band gap excitation), a repetition rate of 1.304 MHz, 10 ps pulse duration and with a fluence of 8.8 mJ/cm^2, in the linear response regime. The photoinduced changes in the sample were probed at the Br K-edge (13.45-13.57 keV) and Pb L_3-edge (13.00-13.14 keV), with ~80 ps time resolution. Comparative temperature-dependent Br K-edge and Pb L_3-edge static XAS was conducted at the SuperXAS beamline of the Swiss Light Source (SLS). The experiments were performed on dry $CsPbBr_3$ NCs enclosed in a thermostated cell holder. The thermal response of the system was monitored in the temperature range between 25 °C and 140 °C, where effects ascribed to either an increase in the NCs local structural disorder [19], or the occurrence of orthorhombic-tetragonal-cubic phase transitions [21; 24] had previously been reported. Moreover, we acquired for each temperature step XRD patterns at 12.9 keV, below both absorption edges, to track longer-range structural changes and to assess the overall quality of the sample.

We performed accurate first-principles calculations using the Quantum ESPRESSO distribution [51; 52], based on density functional theory (DFT) and plane-wave and pseudopotentials technique. The Perdew-Burke-Ernzerhof functional [53] was used to describe electronic exchange-correlation effects. The electron-ion interaction was modelled using ultrasoft pseudopotentials from the PS-library [54]. The projected density of states (p-DOS) was computed across the band gap. XANES Br K-edge spectra were simulated with the XSpectra code [55; 56] of Quantum ESPRESSO, explicitly accounting for the screened core-hole effect in separate supercell calculations for each non-equivalent Br atom, and calculating the average Br K-edge spectra. XANES Pb L_3-edge calculations were not carried out due to the limitations in the explicit inclusion of a screened core-hole in describing holes with non-zero orbital momentum
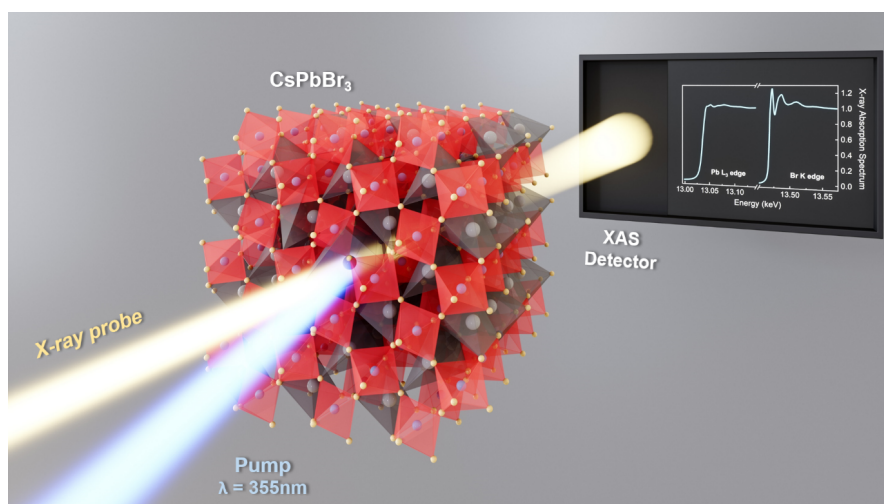
Figure 1.1: Ultrafast element-selective probing of optically-induced polaronic distortions in $CsPbBr_3$ perovskite NCs. Schematic layout of the experiment. TR-XAS was conducted on long-chain zwitterion-capped $CsPbBr_3$ NCs dispersed in toluene solution with a concentration of 5.8 mg/ml and flowed through a flat jet. The laser pump (355 nm) and the X-ray probe, Br K-edge (13.450-13.570 keV) and Pb L_3-edge (13.000-13.140 keV), were in almost collinear geometry.

[57], as in the case of the Pb $2p_{3/2}$ orbital. Details about all experimental methods, the data acquisition scheme, and the computational methods and DOS calculations, are described in the Supplementary information section 1.7.

1.4 Results

1.4.1 Time-resolved X-ray absorption spectroscopy

The steady-state Br K-edge and Pb L_3-edge spectra, normalized to the last data point of the post-edge region, are shown in Figures 1.2a and 1.2b (black solid line). Our calculations of the p-DOS show that the top of the valence band (VB) is composed of Br 4p orbitals, with a non-negligible proportion of Pb 6s orbitals and a minor contribution of Pb 6p orbitals, while the CB is largely dominated by the Pb 6p orbitals (see Figure 1.10 in the supplementary information section 1.7.8).

The photoinduced changes are reflected in the transient spectra, defined as the difference of the excited minus un-excited XAS spectra, and shown for UV pump/X-ray probe time delays of 100 ps (red), 10.1 ns (yellow) and 163.5 ns (grey). The Br transient spectra (Fig. 1.2a) were scaled by the inverse of the absolute area underlying the curves, *i.e.* x155 (100 ps), x363 (10.1 ns), x976 (163.5 ns). The same scaling factors were used for the Pb transients (Fig. 1.2b, details in the supplementary information section 1.7.2.1. Notably, even though the amplitude of the TR-XAS decays over time, the profiles of both Br and Pb transient spectra remain unchanged. The Br K-edge transients show prominent peaks at the pre-edge (13.4675 keV), main-edge (13.472 keV) and post-edge (13.4765 keV) regions. The first feature was ascribed to the opening

of a new 1s-4p channel following the creation of holes in the VB upon photoexcitation [43]. Such a scenario also implies a blue shift of the edge and, indeed, the second and third features could partially be reproduced in the difference spectrum of the blue-shifted ground state spectrum minus the unshifted one. However, this qualitative approach does not account for all the modulations that show up in the above-edge region, which generally point to photoinduced structural changes, as elaborated in the supplementary information section 1.7.7. We shall address these later, using *ab-initio* calculations, and demonstrating their connection with photoinduced structural changes. The Pb L_3-edge steady-state spectrum exhibits featureless edge and XANES regions. The transients are characterized by two positive features in the pre-edge region (13.031 keV and 13.038 keV), a negative peak at the edge position (13.043 keV) and a positive peak in the post-edge region (13.060 keV). The reduction of Pb centres upon photoexcitation of the electrons in the CB, which is mainly composed by Pb p-orbitals, is not compatible with the transient line shape, as discussed by Santomauro *et al.* [43]. The appearance of pre-edge features in the transient traces can only be explained by the opening of new channels from the 2p core orbitals. Indeed, due to hybridization, depleting the VB not only affects the Br centres but also the Pb ones, according to the computed p-DOS (see Figure 1.10 in the supplementary information section 1.7.8). Core-to-valence transitions can occur into the Pb 6s orbitals, which have a non-negligible contribution towards the top of the VB. Above the edge, the transient features are due to photoinduced structural changes. Because the Pb atoms are affected by the structural distortion around the Br centres (see below), it is likely that the above-edge features of the Pb L_3 absorption transient in part reflect these lattice deformations. The decay kinetics at both Br and Pb main edges are shown in Figure 1.2c. The traces were normalized to their maximum value, allowing a straightforward comparison of the time-resolved signal of both centers. It is clear that both traces show the same temporal evolution within the noise level. The data were analyzed following a global fit procedure for both traces. The best fit results were obtained with a bi-exponential decay function and a flat offset, which persists up to the time limit explored in our time traces (130 ns), as shown in Figure 1.6 in the supplementary information section 1.7.2.1. The fit function was convoluted with a Gaussian profile (σ=45 ps), representing the instrument response function of our measurements. The recorded time constants (pre-exponential factors) are τ_1=120±20 ps (60%), τ_2=900±300 ps (21%) and an offset (infinite times of 19% amplitude). Specifically, the fast time component τ_1 is compatible with Auger recombination, where an electron in the CB and a hole in the VB recombine, in a non-radiative process, transferring their energy to a third carrier. Supporting this interpretation, recent fluence-dependent PL and transient absorption studies on $CsPbBr_3$ NCs reported Auger recombination acting on this time scale [58; 59]. τ_2 is ascribed to the radiative recombination of the photoexcited charge carriers, *i.e.* holes from the VB and electrons from the CB, in general agreement with PL studies [50; 60].
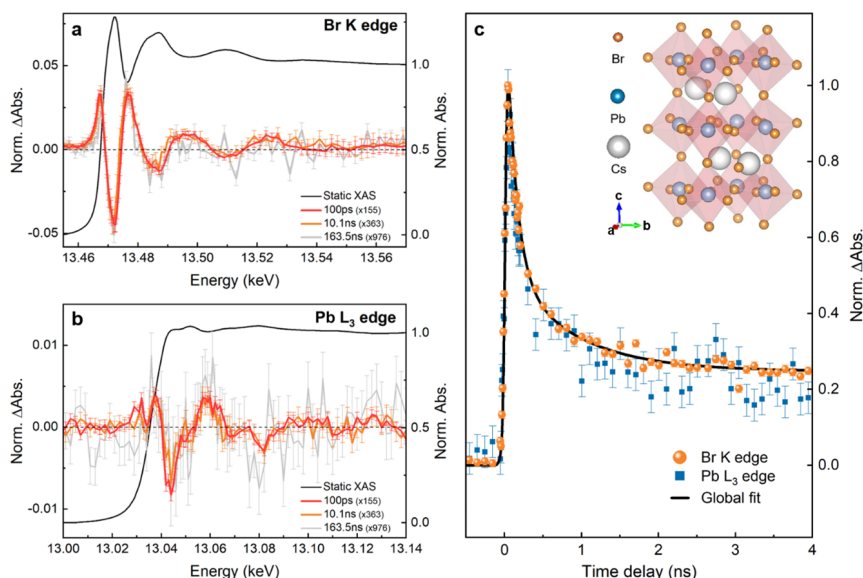
Figure 1.2: X-ray Absorption Energy and Time Traces. (a) Br K-edge and (b) Pb L_3-edge XAS spectra: steady-state (black) and energy transients at 100 ps (red, x155), 10.1 ns (yellow, x363), 163.5 ns (grey, x976) time delays. The error bars correspond to the standard error of the measurements. (c) TR-XAS time traces at the Br K-edge (13.472 keV, orange), Pb L_3-edge (13.043 keV, light-blue) and the exponential fit (black). The error bars were computed as the error propagation of the pumped and unpumped scans, calculated as the square root of the total single photon counts. Inset: a graphical representation of *Pnma* orthorhombic $CsPbBr_3$ [1]. The Br, Pb and Cs atoms are respectively reported as orange, light-blue and grey spheres.

1.4.2 Thermal X-ray absorption spectroscopy

Given the on-going debate about photoinduced electronic and thermal effects [2] and considering that our pump pulse deposits an excess energy of the photocarriers of ~1 eV, it is important to disentangle electronic from thermal effects in the photoinduced response presented here.

In our pump-probe experiment, the hot carriers generated by the pumping process dissipate their excess energy through carrier thermalization in the sub-100 fs regime [30] and, immediately after, by charge carrier cooling on sub-ps time scales [61]. These events determine impulsive heating of the crystalline lattice. If the energy deposited on the system is sufficiently high, therefore, this process might translate into impulsively activated orthorhombic-tetragonal-cubic phase transitions [21]. At later time scales, the hot lattice relaxes through heat transfer to the solvent and/or the ligands. In ligand-stabilized colloidal NCs in solution this process should be completed in sub-ns time scales [62], due to the efficient vibrational coupling between the NC, the ligands and the solvent molecules. Our TR-XAS experiment looks at the system relaxation in time scales from 80 ps onwards after photo-excitation, *i.e.* when the thermal equilibration of the lattice with the surrounding bath has already initiated. At these time scales, the photoinduced relaxation of the system and its purely thermal and temperature-dependent responses can be directly compared. This assumption can be har-
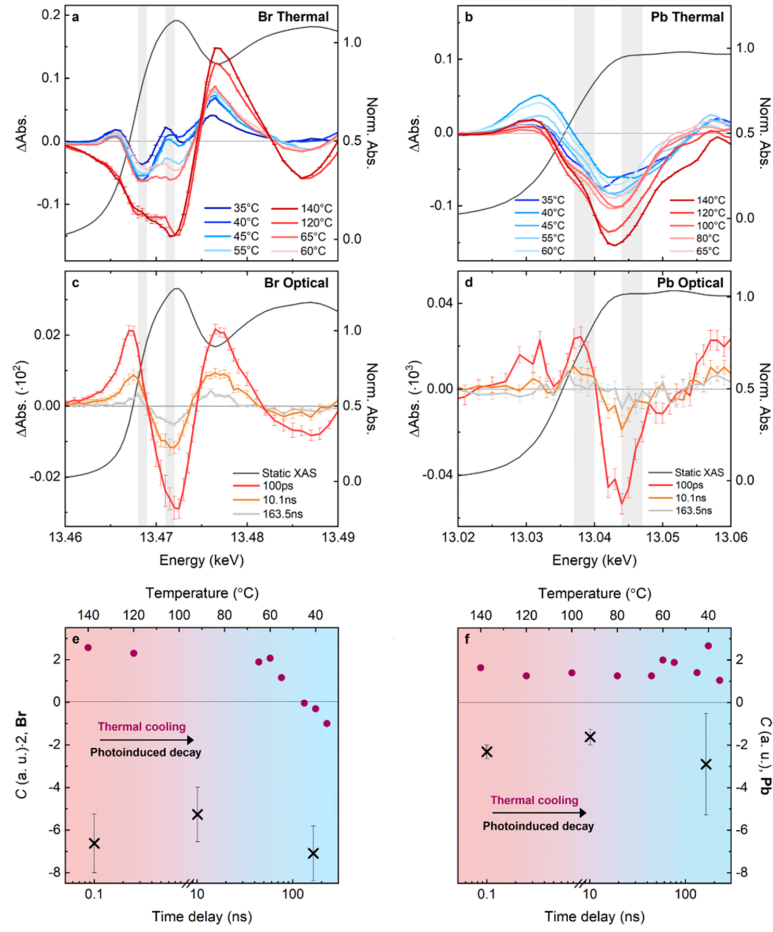
Figure 1.3: Comparison between photoinduced and thermally-activated XAS transition in CsPbBr$_3$ at the Br K-edge and Pb L$_3$-edge. (a) Br K-edge steady-state (dark grey) and temperature-dependent XAS differences from 35 °C to 140 °C (respectively from blue to red) and (b) Pb L$_3$-edge steady-state (dark grey) and temperature-dependent XAS differences from 35 °C to 140 °C (respectively from blue to red). In both panels, the XAS differences were computed by performing a 3-point adjacent averaging and by subtracting the 25 °C spectrum from the temperature-dependent XAS spectra. (c) Br K-edge steady-state (dark grey) and pump-probe spectra at 100 ps (red), 10.1 ns (yellow) and 163.5 ns (grey) and (d) Pb L$_3$-edge steady-state (dark grey) and pump-probe spectra at 100 ps (red), 10.1 ns (yellow) and 163.5 ns (grey). (e) Br K-edge comparison parameter C as a function of the temperature (purple dots, top axis) and pump-probe time delay (black crosses, bottom axis), defined as the ratio of the averaged XAS difference in the energy interval 13.471-13.472 keV and 13.468-13.469 keV, corresponding to the shaded areas in panels (a),(c). (f) Pb L$_3$-edge comparison parameter C as a function of the temperature (purple dots, top axis) and pump-probe time delay (black crosses, bottom axis), defined as the ratio of the averaged XAS difference in the energy interval 13.044-13.047 keV and 13.037-13.040 keV, corresponding to the shaded areas in panels (b),(d). Br C values for both thermal and optical data sets were multiplied by a factor x2 in order to enable a straightforward comparison between Br and Pb results in panels (e),(f).

nessed to verify whether the optically-induced relaxation coincides with thermodynamic lattice cooling. Figures 1.3(a,b) show the thermal difference spectra at the Br K and the Pb

L_3 edges (full thermal spectra are available in Figure 1.12 in the supplementary information section 1.7.9.1. These are obtained by subtracting the 25 °C spectrum from the T-dependent XANES spectra. Figures 1.3(c,d) show the unscaled pump-probe difference spectra at 100 ps (red), 10.1 ns (yellow) and 163.5 ns (grey) for each absorption edge. The thermal difference spectra at the Br K-edge (Fig. 1.3a) display an intensity change through the thermal gradient, with an overall area decrease in the energy range 13.466–13.478 keV lowering the temperature from 140 °C to 25 °C. Particularly, the features at 13.468 keV and 13.472 keV have two different temperature dependences, the former becoming dominant for temperatures below 65 °C. Main differences between photoinduced and thermal data sets can be found in the Br K pre-edge region. Specifically, the negative feature at 13.468 keV found in the thermal data set is absent in the pump-probe spectra, which instead are characterized by a positive peak centered around 13.4675 keV. In the case of Pb, thermal difference spectra in Figure 1.3b display a broad negative feature covering the 13.035-13.053 keV spectral range, whose intensity uniformly decreases lowering the temperature, and a single pre-edge feature centred at 13.032 keV, with intensity increasing upon temperature decrease. In contrast and as already discussed, the pump-probe Pb spectra show two pre-edge peaks, respectively at 13.031 keV e 13.038 keV, whose intensity decreases as a function of time delay.

To quantify overall spectral changes as a function of either temperature or optical excitation, at both edges, we introduce a comparison parameter C defined as:

$$C = \frac{\sum_{E_i} I(E_i)}{\sum_{E_j} I(E_j)} \tag{1.1}$$

with $I(E_i)$ and $I(E_j)$ being the spectral intensities at the energy points E_i, E_j in the main-edge and pre-edge regions, respectively. In Figures 1.3a-d (grey areas), $E_i(Br) = [13.471\text{-}13.472]$ keV; $E_j(Br) = [13.468\text{-}13.469]$ keV; $E_i(Pb) = [13.044\text{-}13.047]$ keV; $E_j(Pb) = [13.037\text{-}13.040]$ keV. The indicated intervals comprise equally-spaced energy points. Figures 1.3(e,f) show the parameter C for Br and Pb, respectively: it expresses the relative intensity ratio between two spectral regions of the same data set, and it describes the entity of XAS spectral shape changes through a temperature gradient (purple dots) or upon photoexcitation (black crosses).

Within the error bars, C values are constant in the pump-probe case for either Br and Pb, in agreement with the spectral evolution of the TR-XAS signal. Indeed, we observe a synchronous systems's response throughout the TR-XAS spectrum in its decay to the ground state. We remark that negative values of C are due to the presence of the pre-edge and main-edge features that have opposite signs, respectively at the energies 13.4675 keV and 13.472 keV for the Br K-edge, and at 13.038 keV and 13.044 keV for the Pb L_3-edge. Starting from 140 °C, the C parameter for the Br thermal differences has stable positive values for temperatures down to 60 °C, and undergoes a progressive change from positive to negative values lowering the temperature in the interval 60-35 °C, due to line shape modifications in the edge region. Instead, Pb thermal differences show positive C values at all temperatures, which originate from the negative sign of pre-edge and main-edge features. Since both features decrease in

amplitude upon temperature decrease, Pb C values remain essentially unchanged with the thermal gradient.

Based on the radically different behaviour of the C parameter for the optical and thermal data sets, we can safely conclude that the photoresponses at the Pb and Br edges reported here are not affected by thermal effects, which likely occur on shorter time scales than our temporal window, as discussed in the following. Thus, we rule out the hypothesis that the photoexcited state corresponds to thermally-driven lattice changes [2].

1.4.3 Theoretical simulations: photoinduced polaronic distortion

The XAS spectrum reflects the probability of an electronic excitation from a core orbital to the unoccupied states of the system that lie at higher energies than the Fermi level. Hence, the first-principles description of XANES spectra requires the computation of highly-localized initial orbitals and of the unoccupied conduction states, the latter in the presence of a screened core-hole, since it reflects the possible final states with a missing core electron.

In condensed matter systems, this level of accuracy is retrieved relying on band structure calculations, where the effect of the screened core-hole is explicitly accounted for as, *e.g.*, in supercell simulations [63; 64]. Band structure calculations also allow access to the phonon spectrum of the system, the atomic displacements occurring upon phonon mode activation, and the electron-phonon coupling between the charge carriers and the lattice degrees of freedom. To date XAS spectra of several solid state systems have been computed using *ab-initio* methods, which rely on real-space atomic clusters, especially for the simulation of excited state spectra [39; 65; 66]. In these cases, the interest was focused on determining the local structural distortions in the photoexcited system, as in the case of charge carrier trapping, rather than understanding the origin of its structural response in the presence of charge carriers, which requires electron-phonon coupling calculations.

First principles computations of pump-probe spectra are generally simulated either using *a-posteriori* strategies, *i.e.* gradually modifying the local structure of a small atomic cluster until the best agreement between the simulation and the experiment is achieved [39; 65], or selecting *a-priori* specific subsets of configurations, where stricter constraints are imposed on a physical basis [66]. Here, to our knowledge for the first time in TR-XAS, we adopt an approach based on *ab-initio* calculations performed under periodic boundary conditions with an *a-priori* selection of the structurally distorted states. Consistent with the phase diagram of $CsPbBr_3$ perovskite [21; 24], we computed the ground state considering the atomic positions of the *Pnma* orthorhombic cell, as derived from room-temperature XRD [24]. The lattice perturbation caused by the optical pump was then simulated following two possible scenarios. First we consider the scenario, ruled out experimentally, in which a thermally-induced phase transition to an ordered $Pm\bar{3}m$ cubic state might occur. In fact, we estimated an upper limit of $\Delta T \sim 120\,°$ to the impulsive heating generated by our pump pulse (see supplementery information section 1.7.9.2) which, in the absence of lattice cooling and consistent with the $CsPbBr_3$ phase diagram, would lead the system from the orthorhombic to the cubic phase. For our simulation we use the atomic coordinates available in the literature [24]. Second,
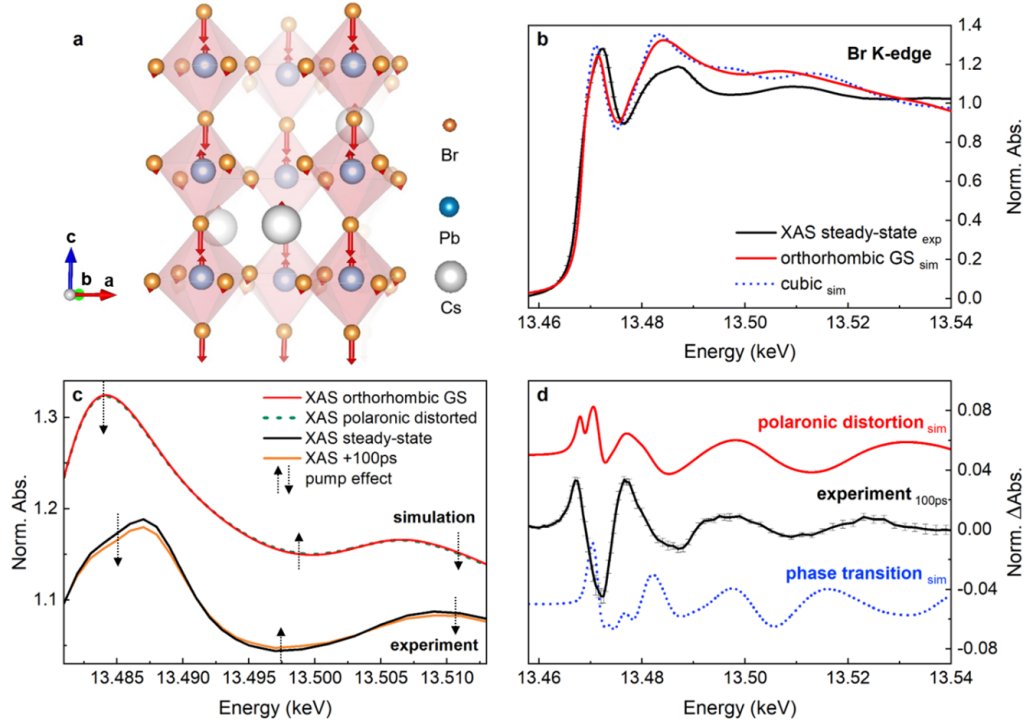
Figure 1.4: Theoretical *ab-initio* calculations of Br K-edge XAS spectra for the ground and structurally distorted states in $CsPbBr_3$. (a) Schematics of the atomic displacements related with the 18 meV LO phonon mode. (b) Steady-state experiment (black, normalized for the last energy point), ground state orthorhombic simulation (red solid line, scaling factor x2550) and cubic simulation (blue dashed line, scaling factor x2550). (c) ground state orthorhombic simulation (red, scaling factor x2550), orthorhombic distorted along the 18 meV LO phonon mode (green dashed line, scaling factor x2550), unpumped (black, normalized for the last energy point) and pumped (yellow, 100 ps time delay, normalized for the last energy point) experimental spectra. (d) Experimental transient at 100 ps (black) and simulated pump-probe obtained as distorted orthorhombic minus pristine orthorhombic spectra (polaronic distortion, red) and cubic minus orthorhombic spectra (phase transition, blue dashed line). All spectra were scaled by the absolute area underlying the curves and the simulated pump-probe additionally multiplied by a factor 70 to enable the comparison with the experiment.

we consider a polaronic distortion induced by electron-hole pair excitation, introducing a structural modification along the 18 meV phonon mode, which is the most strongly coupled to the charge carriers via electron-phonon coupling [44]. The structural modification caused by the aforementioned process is schematized in Figure 1.4a. Key to this method is the adoption of a band structure calculation, which allows to: *(i)* identify the phonon mode with the strongest electron-phonon coupling and; *(ii)* to introduce the phonon distortion in the periodic lattice, thereby approximating the large polaron spatial extension over multiple unit cells, in agreement with the literature [20; 44]. Electronic non-equilibrium effects following the optical excitation were not included in the calculations, being too computationally intensive in the presence of an explicit core-hole description. Figure 1.4b compares the simulated Br

Chapter 1. Quantifying photoinduced polaronic distortions in inorganic lead halide perovskites nanocrystals

K-edge absorption spectra for the orthorhombic ground state (red solid) and the cubic state (blue dots) with the experimental steady-state spectrum (black solid). The three X-ray absorption spectra are characterized by a first peak arising from the Br 1s-4p electronic transition around 13.472 keV. The above-edge spectral modulations for the calculated orthorhombic ground state best reproduce the experiment, as expected from the $CsPbBr_3$ perovskite phase diagram, which is characterized by a *Pnma* orthorhombic symmetry at room temperature. The simulated spectrum for the cubic phase shows a modulation mismatch with respect to the experiment which is prominent in the 13.492-13.505 keV energy range.

Figure 1.4c zooms into the above-edge region beyond 13.480 keV of the experimental pumped and unpumped spectra (respectively, yellow and black traces), and for the simulated orthorhombic ground state and the polaronic distorted state (respectively, red and dashed-green traces). Even though the photoinduced changes are more pronounced in the experiment, the simulation faithfully follows the photo-induced spectral modification, with intensity depletions of the 13.485 keV and 13.508 keV maxima and an intensity increase of the 13.497 keV minimum.

Figure 1.4d shows the simulated pump-probe signals obtained by subtracting the XAS spectrum of the orthorhombic ground state from the XAS spectrum due to the polaronic distortion (red solid) as well as from the cubic phase XAS spectrum (blue dots). The comparison of the difference curves allows to remove possible systematic errors of our *ab-initio* calculation for both ground and excited states. Above the edge, the experimental pump-probe spectrum at 100 ps shows very good agreement in both position and relative amplitude assuming a polaronic lattice distortion generated by the optical activation of the 18 meV LO phonon within the polar inorganic lattice. On the other hand, there is a clear disagreement with the simulation that assumes the phase transition to the $Pm\bar{3}m$ cubic structure. We highlight that the XAS simulation for the orthorhombic-cubic phase transition does not reproduce the spectral line shape of the 120 °C minus 25 °C thermal difference reported in Figure 1.4a either. This result is analysed in a separate work. We remark that the residual deviations between the simulated polaronic distortion and the experimental pump-probe spectra (Fig. 1.4d) can be rationalized considering that electronic effects caused by the optical pump are absent in the calculation. Indeed, the edge region is particularly sensitive to photoinduced changes of the unoccupied DOS of the system. Relying on the one-electron approximation, in Br K-edge transitions the initial and final states differ by the presence of a core-hole in a 1s Br orbital and a photoelectron above the Fermi level. Due to the localization of the 1s orbitals on Br atoms, the Br K-edge transition probability is non-negligible only for final states where the photoelectron has a significant character of the Br absorbing atom, which are present both in the VB and CB (see Figure 1.10 in the supplementary information section 1.7.8). When the band occupancy is perturbed by the optical pump, the Br XANES in the edge-region is also modified.

16

1.5   Discussion

The comparison of optical XAS study with temperature-dependent XAS measurements rules out a dominant photoinduced thermal effect in the TR-XAS response. Indeed, if the evolution of the pump-probe spectral line shape reflected the lattice cooling following impulsive heating, a change in the TR-XAS signal intensity and line shape similar to Figures 1.3(a,b) should be expected. However, this is not observed in the transients reported in Figures 1.3(c,d). Furthermore, this discrepancy is confirmed by the differences in the C parameters of Figures 1.3(e,f) between the thermal and optical data sets. Thus, even though a significant heat deposition could occur under our experimental conditions (see supplementary information section 1.7.9.2 for calculations), a thermal origin of the transient signal can hardly justify the strong difference between the time evolution of the pump-probe signal and the changes expected for thermal cooling.

In ligand-stabilized colloidal NCs, heat transport is known to be determined by the organic/inorganic interface rather than the thermal conductivity of the inorganic core of the NC [67]. In CdSe NC systems, the heat loss from the ligand-NC complex to the bath was observed in 150-320 ps, depending on the solvent [62]. Considering the similarity of the ligand-capped CdSe system and our NCs in size, ligand composition, low-energy NC phonon spectrum, fast thermalization dynamics [62; 68], and the main role of the ligand-solvent coupling to the cooling process, analogous time scales are expected for our $CsPbBr_3$ NCs in solution. Relying on Newton's law to describe the NC lattice cooling and assuming a relatively slow $\tau_{cooling}$ of 300 ps, an initial $\Delta T \sim 120\,°C$ temperature would quickly drop to smaller values, *e.g.* T_{NC}(t=600 ps)$\sim 40\,°C$.

This prediction is in stark contrast with the persistency of the TR-XAS signal over time, which preserves the same line shape at the Br and Pb edges up to the longest time delay measured in our pump-probe experiment, namely 163.5 ns. We conclude that heat dissipation in zwitterion-capped $CsPbBr_3$ perovskite NCs should be complete in shorter time scales than our TR-XAS time resolution, not affecting the pump-probe measurements. Notably, similar results were reported in a Pb L_3-edge TR-XAS investigation on $MAPbBr_3$ ligand-capped NCs in solution [39], where the significant heat load caused by the pump energy deposition into the NC lattice was argued to be dissipated in time scales shorter than 100 ps.

The light-activated structural modification is not compatible with a cubic crystalline structure, nor is it due to disorder, amorphization, or melting caused by thermal effects. Our theoretical analysis clarifies key aspects of the photoinduced response of $CsPbBr_3$ perovskite NCs, ascribing the excited state structural changes to the presence of distinct polaronic distortions that the XAS simulation specifically identifies. Indeed, the atomic displacements of the Pb-Br framework are traced to the distortion of the 18 meV LO phonon mode, which is the most strongly responsive to the charge carriers via electron-phonon coupling. Strong electron-phonon coupling in lead-halide perovskites was demonstrated in the electronic structure of $CsPbBr_3$ single crystals, where signatures of large hole polarons were identified by ARPES and attributed to the activation of the same LO phonon mode [44]. Moreover, previous time-domain results based on the optical Kerr effect [20], electronic resonant and non-resonant impulsive vibra-

tional spectroscopy [31], ultrafast THz studies [32] and 2D electronic spectroscopy [33], were rationalized in terms of polaron formation in organic and inorganic perovskites. Polaronic strain was also invoked as the primary driving force of light-induced phase separation in multi-halide perovskites, explaining the reversibility of the process, its dependence on the number of photocarriers and the self-limiting size of the domains[69]. The importance of electron-phonon coupling on the $CsPbBr_3$ electronic response was also confirmed by PL investigations [37] and time-resolved 2D electronic spectroscopy [34], pointing to a relevant influence of LO phonon modes with energies between 16 meV and 19 meV, and attributed to the lead-halide inorganic framework, consistently with our findings.

Thanks to the agreement with the TR-XAS exprimental results, our simulations provide a compelling atomic-level description of the polaronic distortion. As depicted in Figure 1.4a, the distortion along the 18 meV phonon mode implies that the Pb-Br bonds are asymmetrically shortened along the orthorhombic c-axis, moving Pb cations out of the octahedral inversion centre, and substantially displacing the axial Br nuclei from their equilibrium position, whereas the equatorial Br centres and the Cs ions are marginally affected. Specifically, the photoinduced displacement of the axial Br atoms along the c-axis (Pb-Br$_{axial}$ equilibrium bond distance = 2.958 Å) is 6 times larger than the equatorial Br atoms (Pb-Br$_{equatorial}$ equilibrium bond distance = 2.964 Å) and 2.5 times more pronounced than the Pb off-centre displacement. The post-edge modulations observed in the Pb L_3-edge transients can thus be explained by the displacements of the Pb and Br centres caused by the photogenerated polaronic distortion. Notably, the absence of a photoinduced structural response from the Cs centres reported in [43] also agrees with this finding. Indeed, in all-inorganic perovskites the A$^+$ cation allocated in the lattice cuboctahedral voids is largely mobile and its dynamics is essentially decoupled from the inorganic Pb-X framework [17]. Further supporting the above description is that the kinetic traces and transient XAS energy profiles point to a concerted behaviour of Br and Pb in response to the optical excitation. The time scales of the intensity decays are fully in line with the Auger [58; 59] and PL recombination lifetimes [50; 60] in $CsPbBr_3$ perovskites. The relaxation occurs with a direct recovery of the perovskite's ground state, as confirmed by the retention of the TR-XAS line shapes in the decay process and by the time evolution of the C parameter.

The high PL quantum yields reported for $CsPbBr_3$ NCs [50] and the fact that the transients do not change line shape profile, *i.e.* there is no evidence for intermediate states, point to a recovery of the system largely dominated by charge carrier recombination. The presence of polaronic distortions is consistent with this scenario: after the photocarriers have induced the lattice displacements dictated by the strong electron-phonon coupling of the system, the subsequent electron-hole recombination causes the reversible unlocking of the structural distortions of the Pb-Br framework, back to the ground state configuration. Notably, spectral line changes as a function of time delay were detected in $Cs_3Bi_2Br_9$ perovskites with Br K-edge TR-XAS as a consequence of their asynchronous electronic and structural relaxation upon optical excitation [70], with long-persisting lattice disorder after charge carrier recombination. The observation of short-lived valence holes in $Cs_3Bi_2Br_9$, compared to the post-edge signatures of lattice distortion, indicates that composition and structure of the inorganic sublattice

in halide perovskites, either Bi_2Br_9 or $PbBr_3$, can strongly influence the photodynamics of the system and thus its optoelectronic performances.

This work also highlights the importance of local structural techniques in unraveling the nature of electronic and structural changes in perovskites, triggered by different external perturbations. In diffraction, structural modifications are obtained using approaches that go beyond standard Rietveld refinement methods. One of these methods relies, for example, on the computation of the Fourier transform of the total scattering structure factor to retrieve the PDF, which expresses a probability of finding pairs of atoms separated by a distance r [71]. PDF analysis from X-ray powder diffraction in a host of organic perovskites showed significant internal local distortions of the octahedra at room temperature [25]. Later, total scattering structural characterization, relying on a joint Debye scattering equation/atomic PDF approach, clarified that in $CsPbBr_3$ NCs the structural defectiveness is due to twin boundaries, whose density increase with temperature leads to an apparent higher-symmetry structure that does however not correspond to the $Pm\bar{3}m$ cubic phase [19]. A recent high energy resolution inelastic X-ray scattering and PDF study on $MAPbI_3$ pointed to the presence of thermally-active anharmonic soft modes at 350 K, corresponding to in-phase and out-of-phase rotations of the PbI_6 octahedra [18]. Shortly after, local polar fluctuations were also confirmed in $MAPbBr_3$ and $CsPbBr_3$ perovskites in a temperature-dependent Raman study, where the presence of a zero-frequency Raman peak was assigned to anharmonic thermal fluctuations among different non-cubic structures [27]. All these studies underline that correlating medium-to-long range structural methods with local probes helps distinguishing subtle changes in the perovskite lattice. In this respect, XAS represents a correlative short-range structural tool to probe disordered or dynamically changing systems such as lead halide perovskite NCs. In its time-resolved implementation, TR-XAS offers the advantage of combining electronic and local structural sensitivity, making it an ideal technique to probe lattice modifications induced by the presence of photocarriers, as in the case of polaron formation [39; 40; 43; 70] or charge trapping [66; 72], and to discern them from thermally-induced changes.

1.6 Conclusions

We presented results of light- and temperature-induced changes at the Br K-edge and Pb L_3-edge of $CsPbBr_3$ NCs dispersed in toluene solution or as dry powders. Our results show strong differences between the thermal and optical response of the system, excluding dominant photothermal effects in the observed pump-probe dynamics. The photoinduced spectral changes at the Br K-edge, stemming from a polaron distortion, are here quantified for the first time using advanced band structure calculation, including an *a-priori* selection of the excited state and fully accounting for core-hole effects on the TR-XAS spectra. The comparison between our experiment and theory identifies the lattice changes at the origin of the transient Br postedge modulations with a distortion along a LO phonon mode at 18 meV. These simulations represent an atomic-level description of the light-induced nuclear displacement, dominated by an asymmetric Pb-Br bond shortening along the orthorhombic c-axis. This is supported

by the identical kinetic evolution of the transient Br K-edge and Pb L_3-edge transients, which show that the latter is a direct consequence of the polaronic distortion around Br centres. This is also consistent with the high PL quantum yields reported for $CsPbBr_3$ NCs [50] and provides new microscopic insights in the Pb-Br sublattice dynamics, clarifying the perovskite response under light-induced out-of-equilibrium conditions.

1.7   Supplementary Information

1.7.1   Samples and characterization

Table 1.1 summarizes specifications about the sample 1 employed in the APS TR-XAS experiment and the sample 2 employed in the SuperXAS T-dependent XAS and XRD measurements. Figure 1.5 shows the absorption and emission spectra of the two samples, their transmission electron microscopy (TEM) images, and the high-angle annular dark-field scanning transmission electron microscope (HAADF-STEM) image of a single NC.

Name	Sample 1	Sample 2
Solvent	NC in toluene	Dry NCs
Concentration (mg/ml)	5.8 (in toluene), 23 (dried)	-
Absorption (355 nm, 200 μm path)	1.7 OD	-
Absorption edge	508 nm	503 nm
Luminescence Maximum (FWHM)	516 (18) nm	511 (22) nm
Quantum Yield (%)	>90% (solution)	77.4
Particle Size (number of particles in TEM)	10±2 nm (61)	8.1±1.6

Table 1.1: Samples characterization for APS TR-XAS and SLS T-dependent XAS experiments.

1.7.2   Experimental methods

1.7.2.1   Time-resolved X-ray absorption spectroscopy

The sample consisted of long-chain zwitterion-capped $CsPbBr_3$ perovskite cuboidal NCs with side length 10±2 nm. Their preparation is described in [50]. The 5.8 mg/ml solution of $CsPbBr_3$ NCs dispersed in toluene was kept under stirring conditions and flowed through a sapphire nozzle to produce a 200 μm flat sheet jet, ca. 5 mm wide, ensuring that a fresh spot was excited at each pump pulse. The flat jet was oriented at 45° relative to the X-ray propagation direction. TR-XAS signals were collected at the 7ID-D beamline at the APS of the Argonne National Laboratory (U.S.A.), at the Br K-edge (13.450-13.570 keV) and Pb L_3-edge (13.000-13.140 keV), using a crystal diamond (111) monochromator and employing the ~80 ps (FWHM) pulses provided by the facility in 24-bunch mode, with a repetition rate of 6.52 MHz. The X-ray energy was calibrated using Pb foil. A high repetition rate Duetto laser system (10 ps FWHM pulses, pump wavelength 355 nm) was used to excite the sample at 8.8 mJ/cm^2. The laser repetition rate of 1.304 MHz was set to 1/5 of the 6.52 MHz repetition rate of the
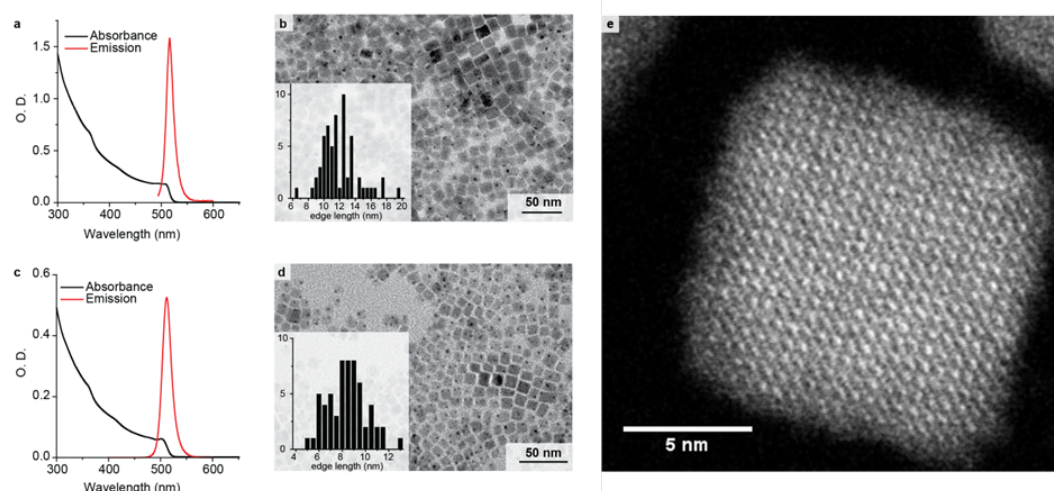
Figure 1.5: Absorption and Emission Visible Spectra and the TEM image of (a,b) sample 1, and (c,d) sample 2, respectively. The insets in (c,d) show the distribution of the average edge length (nm) of the cuboidal NCs, with the y-axis corresponding to the number of counts. (e) HAADF-STEM image of a single $CsPbBr_3$ NC.

synchrotron source.

A nearly-collinear geometry between the X-rays (5 μm spot-size) and laser (45 μm x 50 μm spot-size) was employed, detecting the X-ray fluorescence signal in orthogonal geometry with Avalanche Photodiodes. Br K-edge and Pb L_3-edge spectra were collected both in total fluorescence yield (TFY), with two acquisition methods: analog averaging using a MHz boxcar average (Zurich Instruments) and single photon counting (SPC) using homemade FPGA-based gating electronics. Energy traces were recorded at 100 ps and 10.1 ns time delays at both edges. At every time delay, X-ray absorption spectra were recorded scanning each edge as a function of energy. A non-uniform grid of energy steps was chosen to optimize the acquisition times while still preserving an energy resolution better than 0.5 eV, with finer steps in the edge region and wider steps in the above-edge region. Additional scans were retrieved at 163.5 ns time delay exploiting the higher repetition rate of the synchrotron (6.52 MHz) with respect to the pump (1.304 MHz), which implies that 5 X-ray pulses consecutively probe the sample before a second pump pulse arrives. Considering the small X-ray probe spot size and the average speed of the flat jet (~4 m/s), the second X-ray pulse after the pump still probes a uniformly pumped region, arriving with an additional time delay of 153.4 ns (1/6.52 MHz). Thus, energy transients at 163.5 ns time delay were obtained subtracting the XAS signal of the unpumped sample from the XAS signal recorded with the second X-ray pulse after the pump, when the time delay between the pump and the first X-ray pulse was set to 10.1 ns.

A total accumulation time between 48 s and 66 s per energy point was employed for the averaged energy Br transients, such that the signal-to-noise ratio (SNR) of the measurements is mainly dictated by the signal strengths at the different time delays. At 100 ps the Br K-edge pump-probe signal at 13.472 keV is around 2% of the static signal. For the Pb L_3-edge, the pump-probe signal at 13.043 keV is around 0.4%. Thus, at the Pb L_3-edge, data acquisitions 5
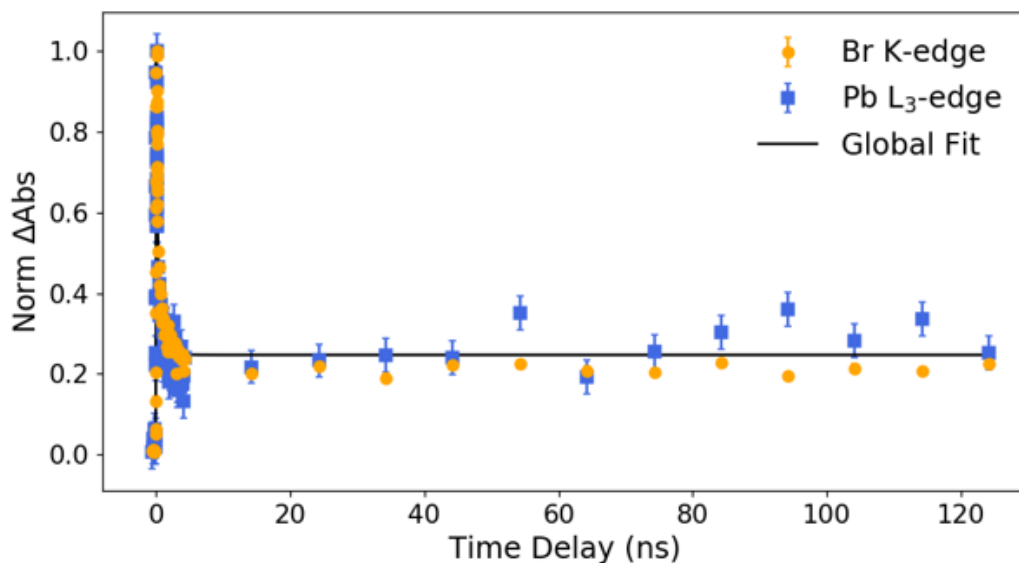
Figure 1.6: Pump-probe kinetics at the Br K-edge (orange) and Pb L_3-edge (blue) up to 130 ns time delays.

and 9 times longer than Br transients were required to get a good statistics, respectively for 100 ps and 10.1ns/163.5ns. Despite the longer acquisition times, the Pb SNR remains lower than at the Br edge. The weak pump-probe response of the Pb centres can be partially attributed to the 1:3 stoichiometric ratio between Pb and Br sites in the sample and to the core-hole broadening of the heavy Pb element, which reduces the energy resolution of the measurement. Additionally, it could reflect the weaker response of the Pb sites to the optical pump. The static spectra in Figure 1.2(a,b) in the main manuscript were normalized for the last point of the post-edge, whereas Br transient spectra were scaled by the inverse of the absolute area underlying the curves, *i.e.* x155 (100 ps), x363 (10.1 ns), x976 (163.5 ns). The error bars were changed accordingly. Due to the higher SNR of Br transients and the correlation between the Br and Pb time responses (see main manuscript), the same scaling factors were used for the Pb spectra. Time traces were obtained recording the spectral intensity at each X-ray absorption edge while scanning the delay between the optical pump and the X-ray probe. The traces were acquired over a range of 130 ns on Br K-main-edge (13.472 keV) and Pb L_3-main-edge feature (13.043 keV), as reported in Figure 1.6. The acquisition times were optimized to obtain comparable SNR levels between the two traces, requiring 36 s per time point at the Br edge and 6 times longer accumulation times at the Pb edge. The dataset in the main manuscript was analyzed following a global fit procedure, where the minimization of the residuals between the fitting curve and the Br and Pb datasets was performed simultaneously

1.7.2.2 Temperature-dependent X-ray absorption spectroscopy

The temperature-dependent XAS and XRD measurements were performed at the SuperXAS beamline at the SLS of the Paul Scherrer Institute (Switzerland). The sample consisted in a powder of $CsPbBr_3$ NCs, allocated into a cell holder between two graphite layers with 0.254 mm thickness. The internal temperature of the cell was calibrated and monitored with a thermocouple. The XAS signal was acquired using a 5-element silicon drift detector (SDD) for fluorescence detection at a 90° geometry. The spectra were collected using a Si(111) monochromator and exploiting the complete filling pattern of the synchrotron delivered at 1.064 MHz repetition rate. Br K-edge (13.450-13.569 keV) spectra were recorded at the temperatures 25, 35, 40, 45, 55, 60, 65, 120, 140 °C, whereas smaller temperature steps were chosen for the Pb L_3-edge (13.000-13.140 keV) spectra, namely 25, 35, 40, 45, 55, 60, 65, 80, 100, 120, 140 °C. XRD measurements were performed with the sample at 0° with respect to the incidence monochromatic X-ray beam (12.9 keV). The signal was collected using a Pilatus 100k detector (94965 pixels, 172x172 μm^2 pixel area) in transmission geometry. The sample-detector distance was 24.10 cm, with the detector laterally displaced of 4.53 cm, avoiding its exposure to the direct X-ray beam. XRD patterns were recorded at the same temperatures as XAS. The background XRD signal generated by the graphite sheets was isolated in a separate measurement.

1.7.3 Fluence scans data analysis

Figure 1.7 reports the fluence dependence of the pump-probe signal intensity at 100 ps time delay, in the range 0.5 to 12.4 mJ/cm^2. In the figure, the Br (13.472 keV, left axis in orange) and Pb (13.043 keV, right axis in blue) main-edges are displayed as a function of the 355 nm pump intensity. The linear fit of the Br data, with better SNR, is showed by the grey solid line, and overlaid to the Pb response. Both signals show a linear regime up to ~10 mJ/cm^2, followed by the onset of a saturation plateau. Our pump-probe measurements were performed at 8.83 mJ/cm^2, approaching the highest fluence within the linear regime. Pb and Br data were recorded in TFY mode at 100 ps time delays. The TFY signals were divided by the incident X-ray flux, monitored with an ungated ion chamber. Laser-on scans were corrected by the offset with respect to the corresponding laser-off scans. The offset was determined as the average of the difference between laser-on and laser-off for the first two points in fluences (correction within the error bars amplitude). In order to compensate for possible concentration fluctuations among different scans, laser-off and laser-on scans were scaled by the mean intensity value of the corresponding laser-off scan. These two corrections were necessary to compensate the large variation in the static signal arriving at the detector in different scans. Laser-on and laser-off scans were averaged and their standard errors were computed as standard deviation scaled by the square root of the number of scans. Pump-probe scans were calculated as the difference of laser-on minus laser-off averages and the pump-probe error was computed through error propagation of the laser-on and laser-off errors.
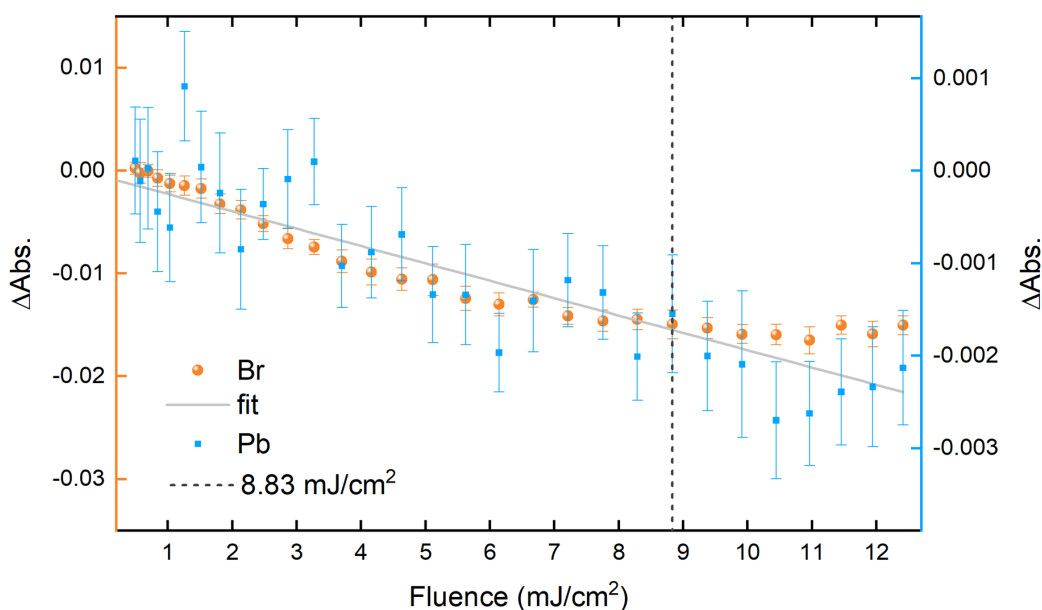
Figure 1.7: Pump-probe fluence dependence intensities at the Br (13.472 keV, left axis in orange) and Pb (13.043 keV, right axis in blue) main-edges. The error bars represent the standard error of the measurements. The dashed vertical line corresponds to the fluence employed in the pump-probe experiments. The grey solid line corresponds to the linear fit of the Br TR-XAS fluence-dependent signal in the linear regime.

1.7.4 Energy scans data analysis

XAS spectra were collected in TFY with the two acquisitions modes mentioned above, which required different data processing procedures. Analog signals averaged in the MHz boxcar were normalized by the incident X-ray flux, monitored with an ungated ion chamber, and the laser-off pre-edge offset was substracted from consecutive laser-off and laser-on scans. Each pair of offset-corrected scans was scaled by the laser-off edge integral and the pump-probe spectra were computed subtracting laser-off from laser-on scans. The pump-probe signal was obtained by averaging the pump-probe scans and the corresponding standard error was calculated from the error propagation of the laser-on and laser-off spectra. The offset correction and edge-integral scaling were employed to correct the scan-to-scan fluctuations, probably due to jet instabilities. The SPC laser-off and laser-on signals were corrected for the probability of having multiple photons hitting the detector and summed over all scans. The corresponding errors were computed as the square root of the total number of counts. Both the signal counts and their errors were scaled by the total incoming flux signal. Separate flat pre-edge offsets were removed from the laser-on and laser-off spectra and the signals were scaled by their edge-integral intensities. Their errors were also scaled by the same scaling factor (but no offset was subtracted, being the error proportional to the square root of the total number of counts). The pump-probe spectrum resulted from the difference of the laser-on and laser-off signals and its error was computed from the error propagation of the laser-on and laser-off errors. Br transients at 100 ps and 10.1 ns were obtained in TFY, averaging 9 and

11 scans respectively, whereas the spectrum at 163.5 ns was recorded in SPC, considering the counts accumulated in 8 scans. Pb energy transients were collected in SPC mode, summing the counts of 56 scans (100 ps) and 87 scans (10.1 ns and 163.5 ns).

1.7.5 Time scans data analysis

Both Br and Pb time traces were collected in SPC mode. The SPC counts were corrected for the probability of having multiple photons hitting the detector and a sum over all the scans was performed for laser-on and laser-off scans separately. The errors were computed as the square root of the number of counts. Both signals and errors were scaled by the total incoming flux intensity and separate offsets were subtracted from laser-off and laser-on spectra, retrieving an average zero intensity of the pump-probe signal at negative time delays. The pump-probe time trace was obtained from the difference of the laser-on and laser-off scans and its error was computed from the error propagation of the laser-off and laser-on errors.

1.7.6 Estimation of the number of photocarriers

Under the fluence conditions of the TR-XAS measurements, we estimate an initial number of photocarriers per NC of about 1000, as predicted by the formula:

$$N = F \cdot \mu \cdot V \tag{1.2}$$

where F is the average 355 nm pump fluence absorbed by the solution in absence of light scattering ($7.6 \cdot 10^{19}$ ph/m^2), μ is the intrinsic absorption coefficient of CsPbBr$_3$ NCs at 355 nm ($1.3 \cdot 10^7$ m^{-1}) [73] and V is the average NC volume (10^{-24} m^3). This average number corresponds to an upper limit and could considerably overestimate the actual number of charge carriers present in the system at the probed time delays. More precise calculations, that are beyond the scope of this study, should consider additional factors, such as light scattering, NC size inhomogeneity, and the statistical (Poisson) distributions of the absorbed photons in the NCs.

1.7.7 Photoinduced blue shift of the Br K-edge

The line shape of the Br K-edge transients consists of three prominent peaks at the pre-edge (13.4675 keV), main-edge (13.472 keV) and post-edge (13.4765 keV) regions and pronounced above-edge modulations at higher energies. Following the approach proposed in [43], we attempted a description of the pump-probe spectra in terms of photoinduced oxidation of the Br sites. The change of the oxidation state of the Br sites would imply a rigid shift of the edge towards higher energies. In Figure 1.8, we compare the Br K-edge TR-XAS at 100 ps (red) and the spectrum obtained by subtracting the unshifted static XAS (black) to the same static XAS rigidly shifted of +5 eV (value which gives the best agreement with the experimental data,
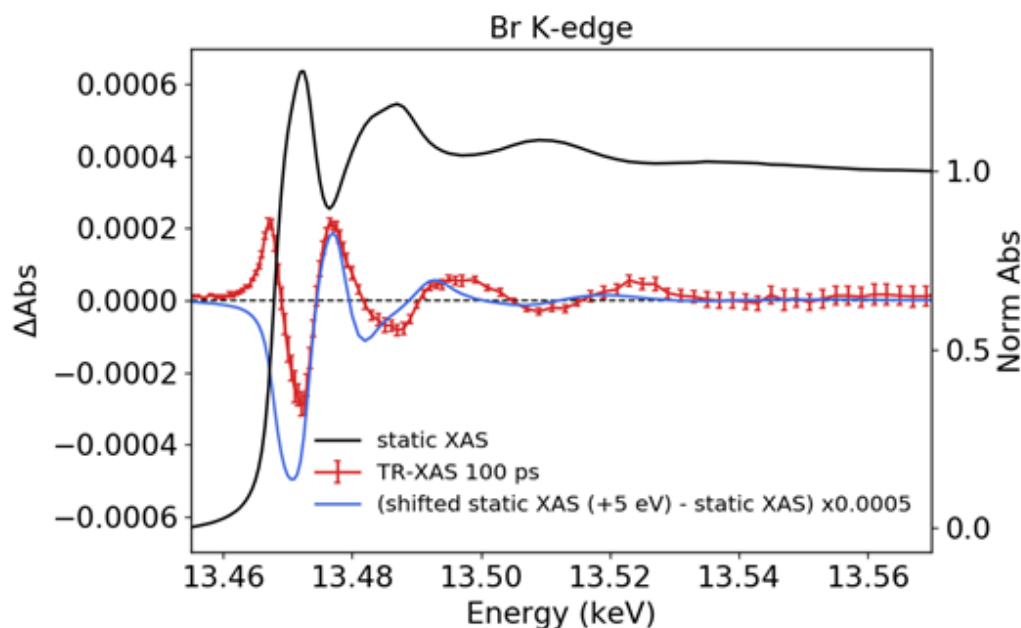
Figure 1.8: Experimental static (black) and transient spectra at the Br K-edge. The experimental pump-probe spectrum at 100 ps time delays (red) is compared with the spectrum obtained by the difference of the blue-shifted (+5 eV) static spectrum minus the unshifted spectrum (blue). The latter was multiplied by a factor $5 \cdot 10^{-4}$ to enable a direct comparison of the spectral line shapes.

in red). The spectra significantly differ for the relative position of the main features, with discrepancies in the energy differences up to 5 eV. Similar results are obtained for other shifting values, with +5 eV giving the best outcome. As reported in section 1.4.1, the absence of the pre-edge positive peak at 13.4675 keV is explained in terms of the opening of a new 1s-4p channel following the creation of holes in the valence band upon photoexcitation. However, the failure in reproducing the pronounced modulations in the above-edge region points towards the presence of structural changes that are not considered in this simplified comparison. The disagreement with the pump-probe experiment makes it essential to perform dedicated ab-initio calculations for the quantitative description of the photoinduced structural changes in the system.

1.7.8   Computational methods and density of states calculation

In this section we discuss the computational approach used to simulate the XANES spectra at the Br K-edge. All the calculations were performed using the Quantum ESPRESSO distribution [51; 52], an open-source tool for electronic structure simulations based on density functional theory (DFT) and plane-wave and pseudopotentials technique. The Perdew-Burke-Ernzerhof (PBE) functional [53] was used to describe exchange-correlation effects. The electron-ions interaction was modelled using ultrasoft pseudopotentials from the PS-library [54]. Semicore 3d, 5d, and 5s plus 5p electrons are treated as valence states for Br, Pb, and Cs, respectively.

The Kohn-Sham wave functions and the charge density were expanded in plane-waves up to a kinetic energy cut-off of 50 and 300 Ry, respectively. A threshold of 10^{-10} Ry/atom on the total energy is set to define the convergence. The equilibrium structures for the orthorhombic and the cubic phases were taken from experiments [24]. The distorted orthorhombic structure was determined starting from the equilibrium one and following the atomic displacement corresponding to the phonon with the largest coupling to the electronic degrees of freedom. The lattice vibration eigenmodes were calculated using the matrix of force constant taken from ref. [44]. The most strongly coupled mode was identified by looking at the effective Fröhlich electron-phonon coupling [44] and corresponds to the Pb-Br stretching mode at 18.2 meV (see Figure 4 in ref. [44]). The strength of the displacement was chosen in such a way to give a change of the order of $K_B T$ in the DFT energy of the orthorhombic unit cell (20-atoms cell). We verified that the results are independent of this parameter by performing additional simulations for the distorted orthorhombic structure doubling the strength of the displacement, as shown in Figure 1.9. No significant changes in the XANES line shape are observed, other than amplitude changes, which have negligible effects on the spectral differences. The XAS cross section $\Sigma(\omega)$ is given by:

$$\Sigma(\omega) = 4\pi^2 \alpha_0 \hbar \sum_{f,\mathbf{k},\sigma} |\langle \phi_{f,\mathbf{k}}^\sigma | D | \phi_{i,\mathbf{k}}^\sigma |\rangle^2 \delta(\epsilon_{f,\mathbf{k}}^\sigma - \epsilon_{i,\mathbf{k}}^\sigma - \hbar\omega) \tag{1.3}$$

where α_0 is the fine structure constant, $\hbar\omega$ the energy of the incoming photons, $\phi_{i,\mathbf{k}}^\sigma$ and $\epsilon_{i,\mathbf{k}}^\sigma$ the wavefunction and energy of the initial state, and $\phi_{f,\mathbf{k}}^\sigma$ and $\epsilon_{f,\mathbf{k}}^\sigma$ the wavefunction and energy of the final state. $D = \mathbf{e} \cdot \mathbf{r}$ is the operator describing the light-matter interaction in the dipole approximation, with $\mathbf{e}$ and $\mathbf{r}$ being, respectively, the polarization vector of the incoming light and the electron position. The absorption cross-sections were calculated in the dipole approximation using an efficient Lanczos recursive method that avoids the expensive calculation of the empty states, as implemented in the XSpectra package [55; 56] of Quantum ESPRESSO. For Br K-edge spectra, the initial state $\phi_{i,\mathbf{k}}^\sigma$ is the 1s wavefunction of the emitting Br atom and the final states wavefunctions $\phi_{f,\mathbf{k}}^\sigma$ and $\epsilon_{f,\mathbf{k}}^\sigma$ were calculated within the so-called excited-electron plus core-hole (XCH) approach [63]. This approach requires a DFT calculation where one excited Br atom with a full core-hole in the 1s state is included in a supercell.

A pseudopotential for the Br atom in this excited configuration was generated with the LD1 module of the Quantum ESPRESSO package. An extra electron was added at the bottom of the conduction band leaving a charge-neutral excitation [63]. Separate XCH supercell calculations are performed for each non-equivalent Br atom in the structure and the final XANES spectrum is obtained from their average. A large enough supercell is needed to avoid spurious interaction of the excited atom with its replicas in periodic boundary conditions.

We verify that a unit cell containing 160 atoms, corresponding to a 2x2x2 supercell of the 20-atoms orthorhombic primitive cell, is enough to get converged results. To converge the Br K-edge spectra, the Brillouin zone of the supercell was sampled with a Γ-centred uniform grid of 3x3x2 $\mathbf{k}$-points. The XAS intensities were averaged over three values of the polarization of
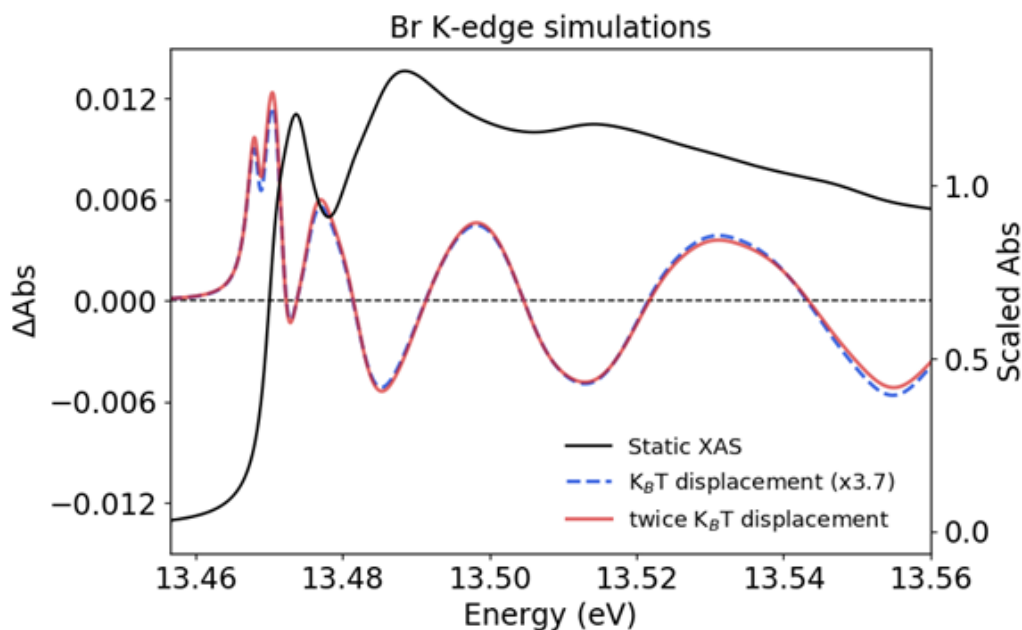
Figure 1.9: Calculated static (black) and pump-probe spectra at the Br K-edge. Two different distortions along the 18.2 meV phonon mode were considered: an atomic displacement corresponding to a DFT energy change of the order of $K_B T$ (dashed blue) and a distortion corresponding to twice that atomic displacement (solid red). The former spectrum was multiplied by a factor 3.7 to enable a direct comparison of the spectral line shapes.

the incoming light, namely along the [001], [010], [100] crystallographic directions. Pb L_3-edge calculations were not carried out due to the limitations of the XCH approach in describing holes with non-zero orbital momentum [57]. The averaged spectra were further convoluted with a Lorentzian having an energy-dependent broadening [74], which starts from 0.3 eV and reaches a maximum value of 6.00 eV, with an arctan-type behaviour and inflection point at 16 eV above the top of the valence-band. The projected density of states (p-DOS) for Br and Pb s, p orbitals are reported in Figure 1.10, showing a dominant contribution of the Br 4p orbitals and the Pb 6p orbitals in the valence and conduction bands, respectively. In Figure 1.11 the calculated Br K-edge spectrum is compared to the experimental data.

A good agreement with the experiment is achieved after the raw data (blue solid line) were convoluted with a Lorentzian function, as described above (red solid line). In the low energy region, the raw data shows two distinct peaks at 2.7 eV and 5.0 eV. After the convolution those merge into a single peak at ~5 eV. The shoulder just before this main peak is visible both in the theoretical and experimental spectra and originates from the first peak at 2.7 eV. These two peaks are directly connected to the p-DOS and come from Br 4p states, as highlighted in the right panel of Figure 1.11.
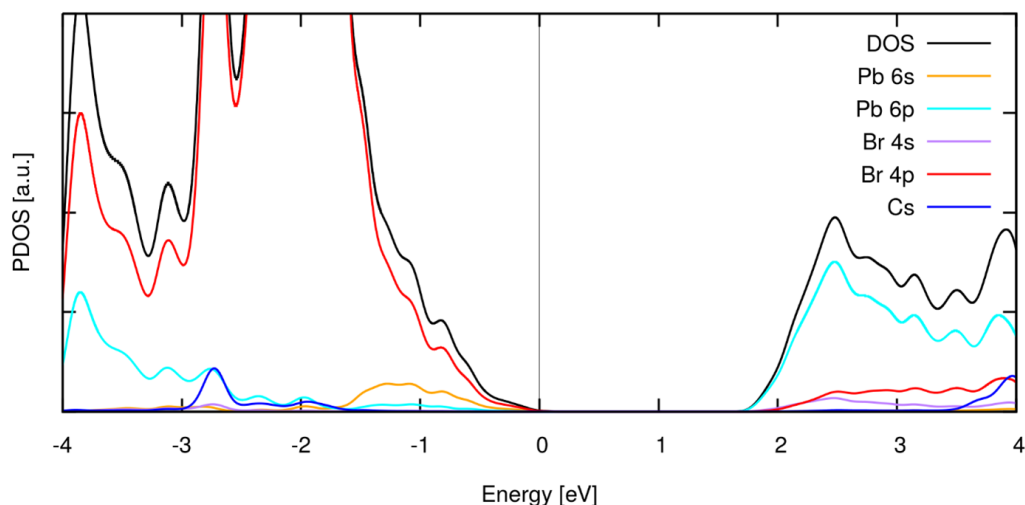
Figure 1.10: p-DOS in the band gap region. The zero of the energy is set at the top of the valence band, mainly constituted of 4p Br orbitals and with a small contribution of the Pb 6s orbitals. The conduction band is dominated by the Pb 6p orbitals, with minor contributions of the Br 4s and 4p orbitals. Cs orbitals do not significantly contribute to the DOS in the first few eVs around the band gap.
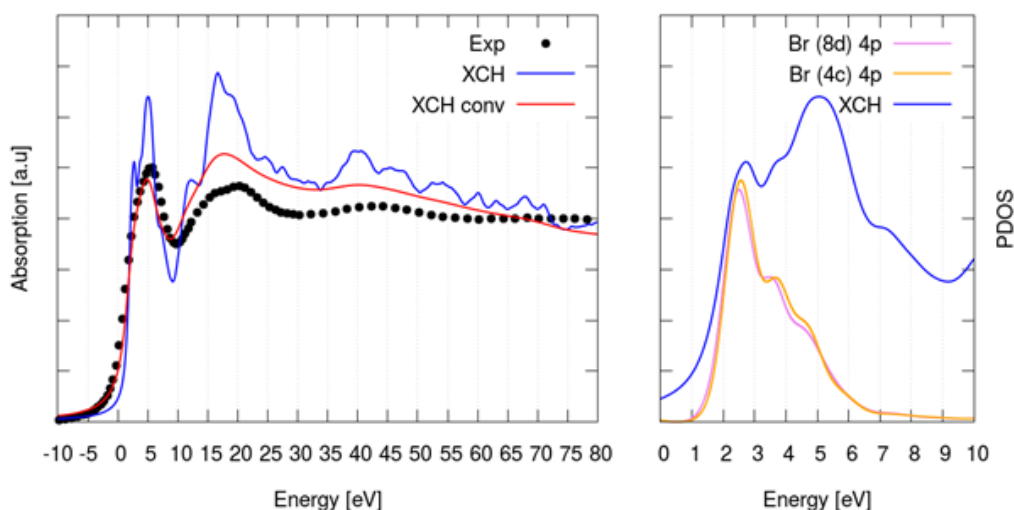
Figure 1.11: Left panel: the calculated Br K-edge XANES spectra (XCH) for the orthorhombic structure before (blue) and after (red) the Lorentzian convolution compared to the experimental data, which was rigidly shifted and aligned to theoretical spectra. Right panel: contribution to the p-DOS from the 4p states of the two nonequivalent Br atoms. The zero of the energy in the plots is set to the top of the computed valence band.

1.7.9   Temperature-dependent X-ray diffraction and X-ray absorption spectroscopy

1.7.9.1   Thermal X-ray absorption spectroscopy at Br K-edge and Pb L_3-edge

Figure 1.12 shows the steady-state spectrum at 25 °C and the XAS differences between the temperature-dependent and the room temperature full spectra, recorded at three key temper-
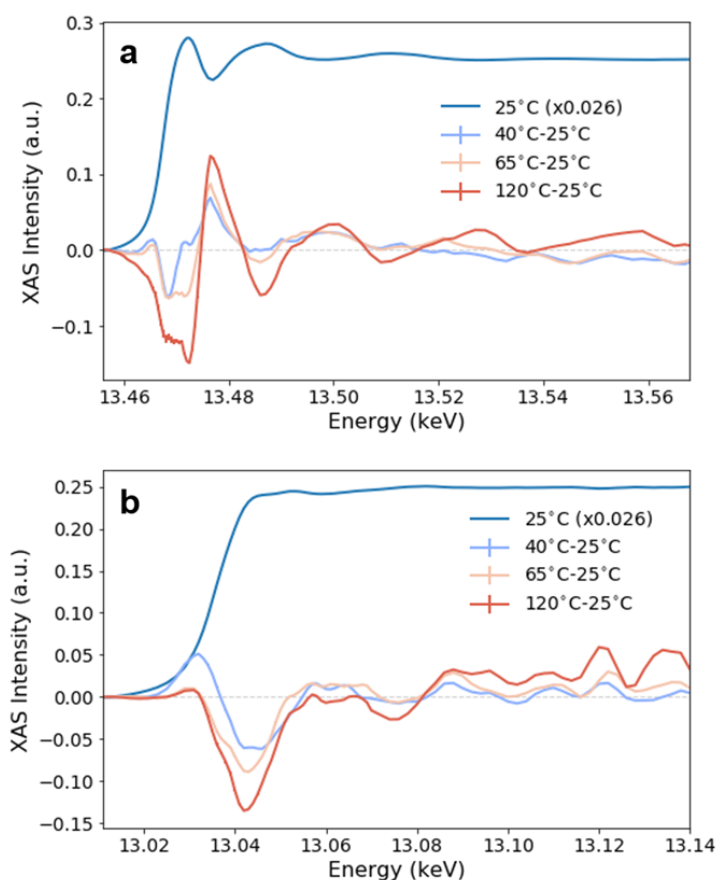
Figure 1.12: Differences between high-temperature XAS minus room-temperature XAS at (a) Br K-edge and (b) Pb L_3-edge, at three selected temperatures.

atures for both Br and Pb edges.

XAS spectra were affected by a minor, systematic energy shift due to the backlash of the monochromator during the extensive energy scan from the Br to Pb edges and to the 12.9 keV energy of the XRD measurements. The source of this backlash was reliably identified because consecutive scans at the same edge did not display significant energy shift, even when varying the temperature. For each scan, the backlash was compensated for an optimal shift, determined through a minimization process as a function of the energy shift. We designed the optimization parameter as the absolute difference between the modulus of the area underlying the normalized first derivative of the considered spectrum and a reference spectrum. The 25 °C spectrum was used as reference.

The same optimization procedure was employed to align the thermal dataset with respect to the steady-state Br K-edge and Pb L_3-edge XAS spectra collected in APS. For all scans, an optimal value for the shift was uniquely identified. In Figure 1.12 we report the typical profile of the optimization value as a function of the energy shift. The backlash correction could remove temperature effects on the XAS edge absolute energy position, as in the case of band gap temperature-dependence.
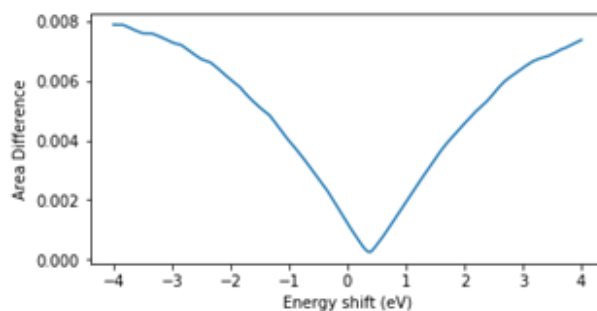
Figure 1.13: Optimization parameter (absolute difference between the modulus of the area underlying the normalized first derivative of a pair of spectra) as a function of the energy shift for the Br K-edge scan at 45 °C. The 25 °C XAS spectrum was taken as reference spectrum.
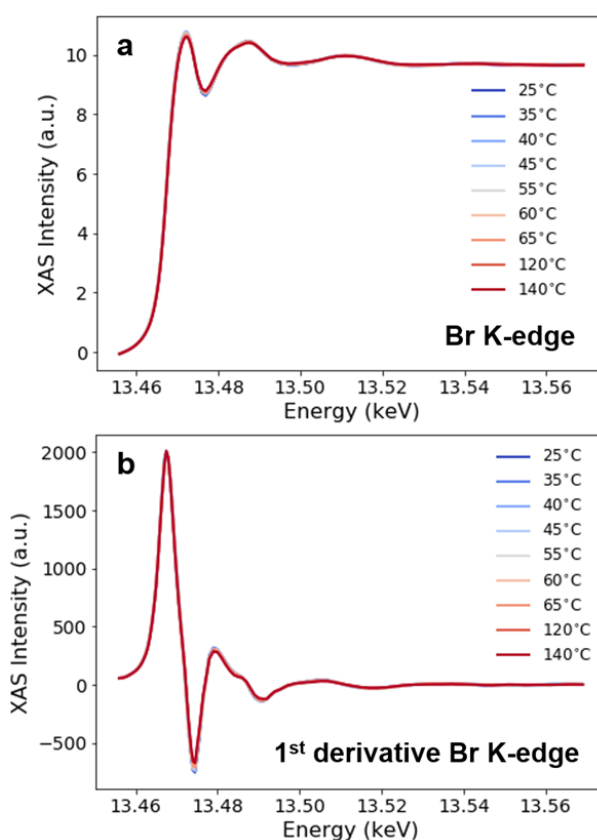
Figure 1.14: Aligned and normalized Br K-edge (a) spectra and (b) first derivative with respect to the energy as a function of the temperature.

Indeed, assuming that the core orbital energies are not affected by changes in the sample temperature, the absolute position of the XAS spectra may change with the band gap, as it influences the energy difference between the valence and conduction bands. A correction was introduced following the Varshni relation [75], estimating the temperature dependence of the system's band gap as:

31

$$E_g(T) = E_g(0) - \frac{\alpha T^2}{T + \beta} \tag{1.4}$$

In the case of CsPbBr$_3$ NCs, the values of α=-7.3·10^{-5} eV·K^{-1} and β=314 K were determined in a temperature-dependent photoluminescence study in the temperature range 80-550 K [76]. Under these assumptions, a blue-shift of the XAS spectra up to 6.5 meV can be expected upon heating the sample from 25 °C to 140 °C, much smaller than the backlash corrections applied to the temperature-dependent Br K-edge spectra (between 0.235 eV and 0.589 eV). For each temperature, the final spectrum was computed as the average of the backlash corrected spectrum and the same spectrum where the Varshni correction was also included. The corresponding error bars were also calculated.

Consistent with the data analysis procedure of pump-probe spectra, a flat pre-edge offset was subtracted from each steady-state scan and the obtained spectrum was normalized by its edge integral. The resulting aligned Br K-edge spectra and their first derivative with respect to the energy are shown in Figure 1.14 as a function of the temperature. Temperature-dependent XAS differences were obtained by subtracting the 25 °C XAS spectrum from each XAS spectrum in the temperature range 35-140 °C.

1.7.9.2   Quantification of the photothermal effect

We estimated the upper limit of the optically-induced temperature changes considering the energy deposited by the pump beam in the CsPbBr$_3$ lattice, in the absence of cooling channels for the NC lattice on sub-100 ps time scales. Accounting for the exceptionally high photoluminescence quantum yield of our sample (~90%), the lattice temperature increase is mainly related to the deposition of the excess energy between the pump wavelength (355 nm) and the emission wavelength (516 nm). We estimate a value of ΔT~120 °C, following the equation:

$$\Delta T = \frac{F_abs \cdot \alpha}{c \cdot d_{jet} \cdot c_p} \tag{1.5}$$

where we considered an effectively absorbed fluence F$_{abs}$ of 7.15 mJ/cm^2 (given the solution optical density of 1.7 O.D.), an energy-to-heat conversion α of 0.41 (which accounts for both the pump excess energy and the 10% of non-radiative recombination), a CsPbBr$_3$ concentration c of 5.8 mg/ml, a jet thickness d$_{jet}$ of 200 μm and the heat capacity c$_p$ value of 215 mJ/g·K, approximated to its lower limit with respect to the temperature [77; 78]. Scattering of light from the liquid jet was neglected. Similar calculations were reported in ref. [41] to estimate the temperature increase in an ultrafast electron diffraction experiment on MAPbI$_3$ thin film. Despite the instantaneous ΔT obtained in the calculation is non-negligible, we can exclude the presence of dominant photothermal effects in our measurements, based on the expected time

scales for the cooling process and the spectral changes associated to it (see main manuscript).

1.7.9.3 Temperature-dependent X-ray diffraction data analysis

T-dependent XRD data were collected using a Pilatus 100k detector, with an incoming X-ray energy of 12.9 keV, in order to monitor the sample integrity in the thermal study. The 2D images were integrated using the python function pyFAI.AzimuthalIntegrator. The sample position with respect to the detector was determined calibrating the measured graphite 2D pattern with the graphite literature data reported in the "pyfai calibration" open source program. The rotation parameters were optimized in the program in order to correct the circles of the 2D maps into straight lines.

The 1D XRD patterns were thus obtained performing a vertical binning of the rectified 2D images. A common linear background was subtracted by all curves. It was determined by minimizing the residuals between the 35 °C XRD background pattern and a linear function used in the fitting. The pixel-to-scattering vector conversion was performed using the following relations:

$$
\begin{aligned}
l &= p \cdot \Delta \\
\delta &= tan^{-1} \frac{l + \alpha}{L} \\
d &= \frac{\lambda}{sin\theta} \\
S &= \frac{2\pi}{d}
\end{aligned}
\tag{1.6}
$$

Where p is the pixel number corresponding to the peak position, Δ is the pixel size, L is the sample-detector distance, α is the distance between the transmitted X-ray beam and the detector in the plane orthogonal to the X-ray beam, λ is the 12.9 keV X-ray energy in wavelength. A least-squares fitting was used to refine the measured L and α quantities in order to match the peak position of the XRD pattern generated with VESTA for a $CsPbBr_3$ orthorhombic unit cell. A Gaussian broadening was applied to VESTA predictions to better resemble the experimental conditions. In Figure 1.15, XRD profiles at selected temperatures are shown over the Q range between 1.3 and 2.8 $Å^{-1}$. The prominent peak at 1.83 $Å^{-1}$ comes from the background signal of the thin layers of graphite encasing the $CsPbBr_3$ sample.
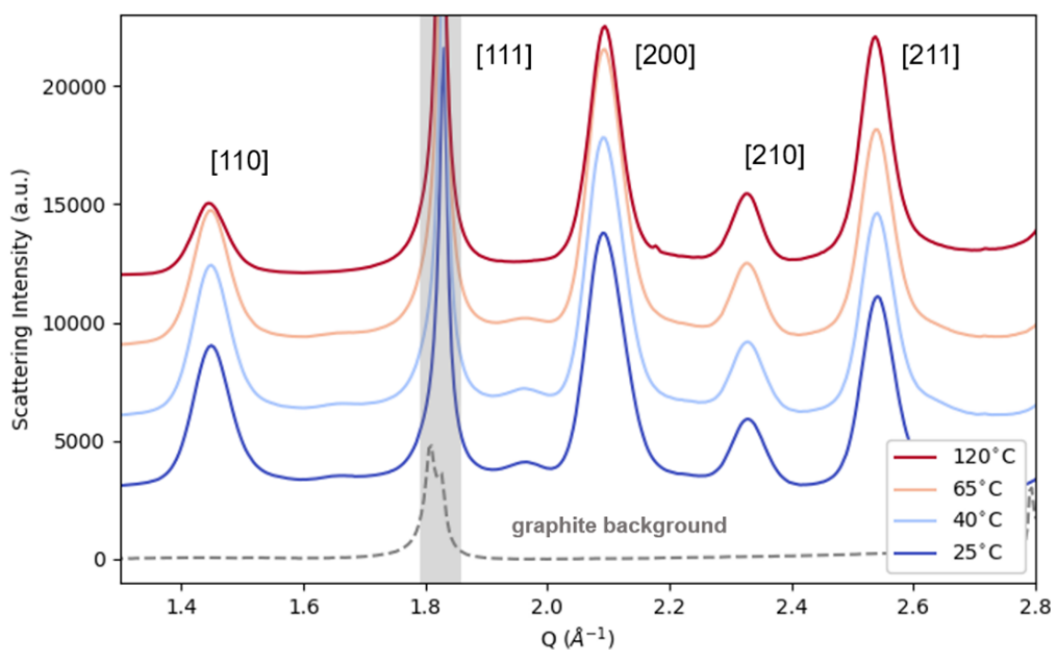
Figure 1.15: XRD in the 1.3-2.8 Å^{-1} Q range at four selected temperatures. For the 120 °C pattern, the peaks are labelled according to the high-temperature $Pm\bar{3}m$ cubic phase reported in the literature [2]. An arbitrary offset was introduced for each spectrum to better resolve the spectral evolution with the temperature. The dashed grey curve corresponds to the background originated by the graphite sheets of the thermostated cell, which signal is superimposed to the [111] CsPbBr$_3$ diffraction peak.

2 Local disorder in the CsPbBr$_3$ high temperature phase: the role of thermal fluctuations and phonon anharmonicity

The following chapter is adapted from a manuscript currently under writing, involving the following authors:
O. Cannelli, J. Wiktor, N. Colonna, M. Puppin, L. Leroy, C. Bacellar, I. Sadykov, F. Krieg, G. Smolentsev, M. V. Kovalenko, A. Pasquarello, M. Chergui, G. F. Mancini.
My contribution: experimental measurements, data analysis, data interpretation, manuscript writing.

2.1 Abstract

The widespread application of perovskite active materials for technological devices is currently limited by their poor long-term stability. A better understanding of the system's degradation under external perturbations such as thermal heat requires the development of consistent atomic level descriptions. In this work, we report that the temperature-dependent response of CsPbBr$_3$ nanocrystals across the phase diagram is primarily caused by local thermal fluctuations. Combining X-ray powder diffraction and X-ray absorption measurements at the Br K-edge, we monitored long- and short-range structural changes as a function of the temperature and directly compared these results with the predictions of accurate *ab-initio* simulations. Specifically, we clarify the origin of the X-ray diffraction and X-ray absorption pattern changes, ascribed to thermally-induced dynamical disorder rather than to a local symmetry increase of the lattice with the temperature. The observed changes in the PbBr$_6$ octahedral tilting distribution point to thermally-induced phonon anharmonicity effects. The comprehensive description proposed in our work paves the way for a rational control of the lattice response under external stimuli.

2.2 Introduction

The implementation of lead-halide perovskites as active layer in photovoltaic and optoelectronic devices is currently hindered by their relatively poor stability [79; 80]. Despite their promising performances [8; 81], these materials suffer from different forms of degradation under operative conditions, caused by external factors such as oxygen, moisture or UV light exposure [82–84]. Composition and structural instabilities were also observed, due to phase segregation [85] and thermal heat effects [86]. Understanding the mechanisms underlying these issues requires the characterization of the system's response under these external perturbations as a first step towards next generation devices development and their marketability. In both inorganic and hybrid perovskites, the common lead-halide inorganic framework constitutes the structural backbone hosting either inorganic or organic cations and determining the structural response of the system [17]. Given this lattice structure, all-inorganic pervoskites are benchmark systems to study thermal effects on the crystal lattice because of the absence of the additional dipolar interactions caused by the organic cations of the hybrid systems. In CsPbBr$_3$, the ABX$_3$ perovskite crystal consists of a Pb-Br inorganic sublattice in which the Pb^{2+} ions are surrounded by 6 Br$^-$ anions, making a framework of corner-sharing octahedra. The cuboctahedral voids left in the crystal are filled by the Cs$^+$, creating a complementary sublattice where the cations undergo a free rattling motion [17]. In single crystals, the phase diagram of this system was determined by X-ray diffraction (XRD) and it was assigned to phases of decreasing symmetry upon temperature lowering: cubic $Pm\bar{3}m$ (T>130 °C), tetragonal $P\dfrac{4}{m}bm$ (88 °C<T<130 °C) and orthorhombic $Pnma$ (T<88 °C) [24]. A neutron diffraction study ascribed the phase transition sequence to the condensation of the PbBr$_6$ tilting modes into distorted geometries [87]. Indeed, starting from the perfect cubic symmetry of the perovskite lattice (schematically shown in Figure 1a, top), the tetragonal phase is obtained by distorting the PbBr$_6$ octahedra unit cell along the equatorial plane, causing a deviation of the Pb-Br-Pb angle from the ideal 180° value. The additional distortion of the Pb-Br-Pb angles along the axial plane modifies the lattice symmetry from tetragonal to orthorhombic, as represented in Figure 2.1a (bottom). In these works, the highest temperature phase was assigned to a cubic lattice based on the disappearance of XRD faint reflections called superlattice peaks. These features arise in low symmetry phases from the periodic recurrence of the cooperative octahedral tilting, which doubles the unit cell constant along the axis perpendicular to the tilting direction [88], as represented in Figure 2.1a (bottom) for the c-axis of the orthorhombic phase. The XRD patterns for orthorhombic and cubic unit cell symmetries are shown in Figure 2.1b, as predicted in VESTA software [1] at 12.9 keV X-ray incident energy.

This simple description of the system's lattice changes across the phase diagram became more debated only in recent years, despite the fact that the presence of structural disorder at high temperatures was already suggested in the seminal work of Møller on inorganic lead-halide perovskites single crystals [89]. Thermal fluctuations of the inorganic Pb-Br framework among instantaneous non-cubic structures were proposed in a joint temperature-dependent Molecular Dynamics (MD) and low-frequency Raman study on methylammonium (MA$^+$) lead-bromide and caesium lead-bromide single crystals [27]. Thermally-induced rotational
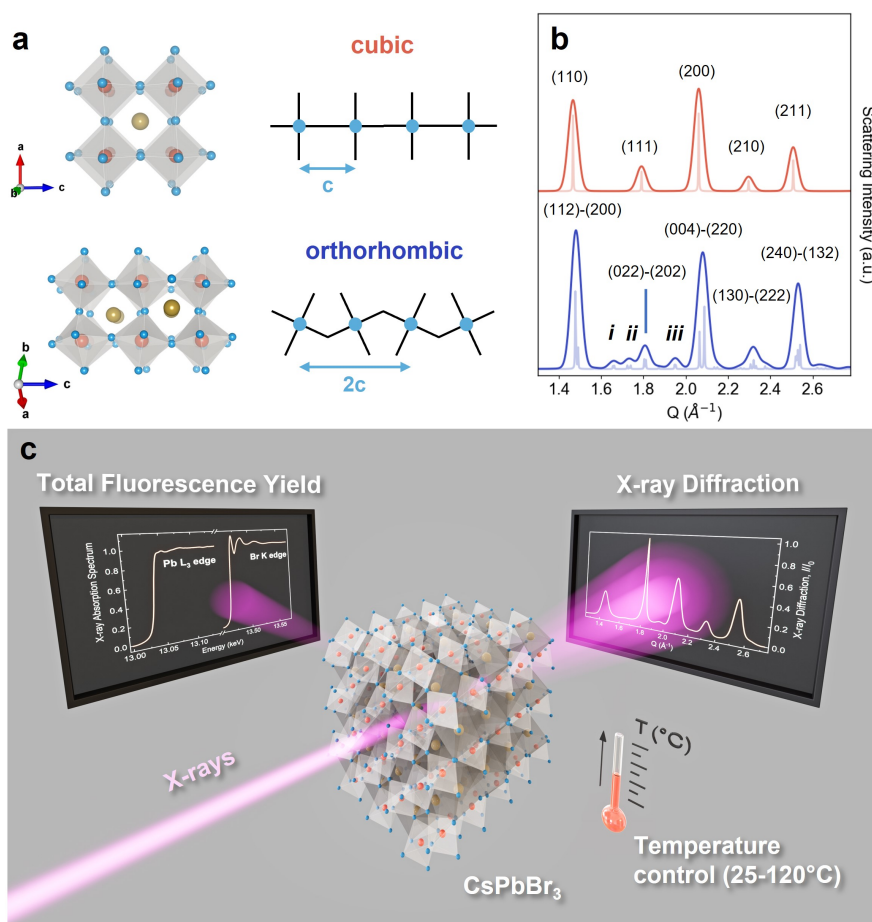
Figure 2.1: (a) CsPbBr$_3$ crystal structures. Pm$\bar{3}$m cubic (top) and *Pnma* orthorhombic (bottom) graphical representations of the CsPbBr$_3$ structures, and pictorial views of the octahedral tilting. In the orthorhombic phase, the ordered tilting of the PbBr$_6$ octahedra causes the doubling of the unit cell constant along the crystallographic c-axis; (b) CsPbBr$_3$ XRD patterns. Cubic (top) and orthorhombic (bottom) XRD patterns simulated in VESTA [1] for a 12.9 keV incident X-ray energy. The peaks *(i),(ii),(iii)* correspond to the superlattice peaks and rise from the unit cell doubling of the low symmetry phase with respect to the cubic structure. (c) Long- and short-range structural probing of thermally-induced changes in CsPbBr$_3$ perovskite nanocrystals: schematic layout of the experiment. Temperature-dependent XRD and XAS measurements were conducted in parallel on CsPbBr$_3$ dry nanocrystals respectively at 12.9 keV and at the Br K-edge (13.450-13.570 keV).

disorder of lead-halide octahedra was also observed in a high energy resolution inelastic X-ray scattering (HERIX) and PDF study on MAPbI$_3$ single crystals at 350 K, ascribing the effect to the phonon anharmonicity of the Pb-I cage [18].

For ligand-stabilized nanostructures the scenario is even more complex, due to intrinsic heterogeneity of the polycrystalline structures and the strong background XRD signals, related to the high surface-to-bulk ratio of the nanocrystals (NCs) and to the diffuse scattering of the organic ligands [19; 90]. In these systems the phase transition temperatures vary with the size of the samples, which for CsPbBr$_3$ nanocrystals were observed at T=108-117 °C, for the cubic-tetragonal phase transition, and T=50-59 °C, for the orthorhombic-tetragonal phase

transition [21].

Also in this case, the picture of lattice symmetry changes with the temperature became questioned by more refined structural characterizations. An X-ray total scattering and Pair Distribution Function (PDF) study on all-inorganic lead-halide perovskites NCs identified the presence of orthorhombic twin domains, which preserve the Pb-X distortions above the highest phase transition temperature [19]. The authors proposed that this static disorder is entropy driven, due to a temperature-induced increase of the orthorhombic nanodomain density. In the proposed scenario, the apparent higher-symmetry of the system would come from the configurational average of differently oriented domains. Structural disorder of the metal-halide framework was also observed in organic lead- and tin-halide perovskites. Investigations based on PDFs obtained from the Fourier transform of X-ray powder diffraction showed that, in their high temperature phases, the structural refinements for short and long internuclear distances of these systems pointed to different lattice structures [25]. Specifically, significant internal distortions of the BX$_6$ octahedra were observed for short internuclear distances, whereas cubic symmetries were proposed to describe the structure at longer distances.

All these works highlight the presence of significant static and dynamic disorder, raising questions about the assignment of highly ordered phases in CsPbBr$_3$ and in other perovskite systems, especially at high temperatures. However, despite the large variety of employed techniques, a unified picture simultaneously describing thermally-induced changes in the short- and long-range is still missing. Key to solving this challenge is the combination of consistent observables from experiments and simulations, offering a comprehensive atomic level description.

In a recent time-resolved X-ray absorption spectroscopy (TR-XAS) study on CsPbBr$_3$ nanocrystals (NCs), we combined experiment and theory to quantify local structural changes due to the polaron formation occurring upon laser light excitation [91]. We demonstrated that lattice distortions are due to the activation of a specific longitudinal optical phonon via electron-phonon coupling, and we ruled out thermal contributions to the photoinduced dynamics of the system, based on the comparison of the TR-XAS spectra with temperature-dependent ones.

Here, we focus on the steady-state characterization of the purely thermal response of the CsPbBr$_3$ NCs across their phase diagram. We demonstrate that the high temperature phase of this perovskite shows a wide range of locally disordered configurations, on average centred on the high symmetry positions of the cubic phase. We performed a correlative temperature-dependent measurement combining X-ray powder diffraction and Br K-edge X-ray absorption spectroscopy (XAS) on CsPbBr$_3$ NCs in the 25 °C-120 °C range, *i.e.* across the phase diagram of the nanostructured system. Our approach allows us to simultaneously monitor the long-range structural modifications occurring in the crystal with the local lattice changes.

Our XRD results are directly compared with the predictions of accurate *ab-initio* MD simulations as a function of the temperature. The agreement between theory and experiment clarifies the origin of the system's XRD pattern changes upon temperature rise, showing for the first time in CsPbBr$_3$ that the disappearing superlattice peaks are related to short-range dynamical disorder and not to a symmetry increase. We observe thermally-induced changes in

the distribution of the $PbBr_6$ octahedral tilting, which are rationalized in terms of temperature-dependent effects due to the phonon anharmonicity.

These results are further reconciled with the local characterization of the Pb-Br framework through the comparison of the temperature-dependent XAS measurements with refined *ab-initio* simulations, which include the core-hole effect on the computed spectra. Our finding confirms that in the high temperature phase, the local structure deviates both from purely orthorhombic and cubic symmetries, differently from the co-existence of orthorhombic and cubic domains observed at room temperature [92], supporting the idea that multiple local configurations are dynamically adopted by the system. The stocastic nature of the thermal fluctuations prevents determining specific lattice changes caused by the temperature increase, differently from the light-induced polaronic distortions, which are selectively driven by electron-phonon coupling and therefore could be precisely quantified with TR-XAS [91]. The deeper understanding of the perovskite responses upon different perturbations opens the opportunity for the control of the system, externally influencing the lattice structure and its stability.

2.3   Methods

Parallel temperature-dependent XRD and XAS measurements were performed at the Su-perXAS beamline at the Swiss Light Source (SLS) of the Paul Scherrer Institute (Switzerland), respectively in transmission and fluorescence geometry. The samples were synthesized by our collaborators Dr. Franziska Krieg and Prof. Maksym V. Kovalenko (Institute of Inorganic Chemistry, Department of Chemistry and Applied Biosciences, ETH Zürich, Switzerland) and consisted of a powder of long-chain zwitterion-capped $CsPbBr_3$ dry perovskite NCs with cuboidal shape (side length 8.1±1.6 nm) and high photoluminescence quantum yield [50], allocated into a thermostated cell holder between two graphite layers of 0.254 mm thickness. The internal temperature of the cell was calibrated and monitored with a thermocouple. For each temperature, the thermal response of the sample was measured with XRD and XAS in the temperature range between 25 °C and 120 °C, across the reported $CsPbBr_3$ NCs phase transitions [21; 24]. A schematic representation of the experiment is shown in Figure 2.1c.

Temperature-dependent XRD measurements were performed with the sample at 0° with respect to the incidence monochromatic X-ray beam at 12.9 keV. The transmitted signal was collected using a Pilatus 100k detector (94965 pixels, 172x172 μm^2 pixel area). The sample-detector distance was 24.10 cm, with the detector laterally displaced of 4.53 cm, avoiding its exposure to the direct X-ray beam. XRD patterns were recorded at the temperatures 25, 35, 40, 45, 55, 60, 65, 120 °C. The 2D images were integrated using the python function py-FAI.AzimuthalIntegrator and a common linear background was subtracted from all curves. The XRD signal generated by the graphite sheets was identified in a dedicated measurement without the perovskite sample. The sample integrity was preserved at all temperatures up to 120 °C, as confirmed by the collected XRD patterns. Parallel temperature-dependent XAS measurements were conducted using a 5-element silicon drift detector (SDD) for fluorescence

detection at 90° geometry. The spectra were collected at the Br K-edge (13.450-13.569 keV) for the temperatures 25, 35, 40, 45, 55, 60, 65, 120 °C using a crystal silicon (111) monochromator. As described in [91], systematic energy shifts due to the monochromator backlash across subsequent energy scans were corrected by designing an optimization parameter, corresponding to the absolute difference between the modulus of the area underlying the normalized first derivative of the considered spectrum and a reference spectrum (25 °C spectrum). Band gap temperature-dependent contributions to the XAS edge absolute energy position were introduced following the Varshni relation [75]. The final spectra were obtained averaging the backlash corrected spectra and the same spectra with the additional Varshni correction, computing the corresponding error bars. A flat pre-edge offset was subtracted for each spectrum and the intensity was normalized by the edge integral.

To provide an accurate atomic level description of the temperature-dependent structural changes, we collaborated with Prof. Julia Wiktor (Chalmers University of Technology, Gothenburg, Sweden) and Prof. Alfredo Pasquarello (École Polytechnique Fédérale de Lausanne, Lausanne, Lausanne, Switzerland). *Ab-initio* Molecular Dynamics (MD) simulations based on density functional theory (DFT) were performed using the CP2K package [93]. The Perdew-Burke-Ernzerhof (PBE) functional [53] was used to describe the exchange-correlation energy. Three different MD simulations, lasting for 10-16 ps, were carried out in the isobaric (NpT) ensemble. In the runs, the initial shape of the cell was kept constant, while the volume of the cell was allowed to fluctuate. One MD calculation was run at 27 °C (300 K) with the initial orthorhombic geometry. At 130 °C (403 K), two simulations were run, one initialized with the cubic and one with the orthorhombic geometry. All simulations were carried out in supercells containing 1080 atoms, which corresponds to the 6x6x6 repetition of the unitary cubic cell. The Brillouin zone was sampled at the sole Γ point. The first 5 ps of the simulations were considered as equilibration period and were excluded from the statistics. The mean XRD patterns were calculated by averaging the diffractograms predicted by VESTA [1] for instantaneous structures separated by 0.75 ps extracted from the MD trajectories.

We collaborated with Dr. Nicola Colonna (Laboratory for Neutron Scattering and Imaging, Paul Scherrer Institute, Villigen, Switzerland) to compute XAS spectra performing detailed first-principles calculations using the Quantum Espresso distribution [51; 52] based on a DFT-PBE approach and plane-wave and pseudopotentials technique. The exchange-correlation effects were described using the PBE functional [53], and the ultrasoft pseudopotentials from the PSlibrary [54] were employed to model the electron-ion interaction. Valence states for Br, Pb and Cs atoms were described using semicore 3d, 5d, and 5s plus 5p electrons, respectively. Plane-wave expansions up to a cut-off kinetic energy of 50 and 300 Ry were performed respectively for the Kohn-Sham wave functions and the charge density. An energy convergence threshold of 10-10 Ry/atom was defined in the calculations. The Br K-edge absorption cross-section was computed in the dipole approximation with the Lanczos recursive method, avoiding the expensive calculation of the empty states, using the XSpectra package [55; 56] of Quantum ESPRESSO. The unit cell atomic coordinates were taken from the PDF refinements of XRD data recorded at 22 °C and 160 °C, respectively for the orthorhombic and cubic structures [21]. The simulations were performed on 2x2x2 supercells using the so-called excited-electron plus

core-hole (XCH) approach [63]. In this method one excited Br atom with a full core-hole in the 1s state is included in the supercell and its excited configuration is generated with the LD1 module of Quantum ESPRESSO package. A charge-neutral excitation is obtained by adding an extra electron in the bottom of the conduction band. Separate XCH supercell calculations were performed for each non-equivalent Br atom in the structure, using a large enough supercell to prevent spurious interactions between the excited atom and its replicas in periodic boundary conditions. The final XAS spectra result from the average of each non-equivalent Br site over three values of the polarization of the incoming light, namely along the [001], [010], [100] crystallographic directions. The supercell Brillouin zone was sampled with a uniform grid of 3x3x2 k-points centred in the Γ point. The spectra were convoluted with an energy-dependent Lorentzian broadening [74], starting with 0.3 eV and reaching the maximum value of 6.0 eV, with an arctan-type behaviour. The inflection point was set 16 eV above the top of the valence band.

2.4 Results

2.4.1 Temperature-dependent X-ray diffraction

In Figure 2.2a we show the evolution of the experimental XRD pattern as a function of temperature, from 25 °C to 120 °C, and in the 1.25-2.7 Å^{-1} Q range. The pronounced peak at 1.827 Å^{-1} scattering vector comes from the background signal generated by the graphite sheets enclosing the sample, and it is superimposed on the main reflections (022)-(202) and the superlattice peak *(ii)* of the orthorhombic phase, preventing the evolution of the system through the tetragonal phase to be followed. Nonetheless, the scientific focus of this work is on the temperature-dependent changes between room temperature (orthorhombic phase) and the temperatures above 120 °C (allegedly cubic phase). Within our experimental energy resolution, we do not observe significant changes in the shape or width of the main reflection peaks up to the highest temperature, confirming that the quality of the NCs is preserved in the entire temperature range 25-120 °C. Upon temperature increase, we monitor the progressive disappearance of the superlattice peaks *(i)* and *(iii)*, highlighted with grey shaded areas, up to the highest phase transition temperature of the NCs (120 °C) [21].

Our experimental study was complemented with *ab-initio* MD simulations. Three different conditions were considered in our calculations: MD at 27 °C and 130 °C, both starting with an orthorhombic structure, and MD at 130 °C starting with a cubic structure. As elaborated in the following, both 130 °C structures are highly dynamic and are characterized by pronounced local distortions. Although they differ for the initial symmetry employed in the simulation, their thermal dynamics let the systems converge to similar structures that locally resemble a mixture of orthorhombic and cubic phases. The results of the MD as a function of time are reported in the Supplemetary information section 2.7.1.

In Figure 2.2b, we report the XRD pattern predicted by the *ab-initio* MD simulations for the three considered cases. At 27 °C we distinctly observe the presence of the three superlattice peaks *(i)*, *(ii)*, *(iii)*, confirming that a repeating pattern of PbBr$_6$ octahedral tilting is preserved
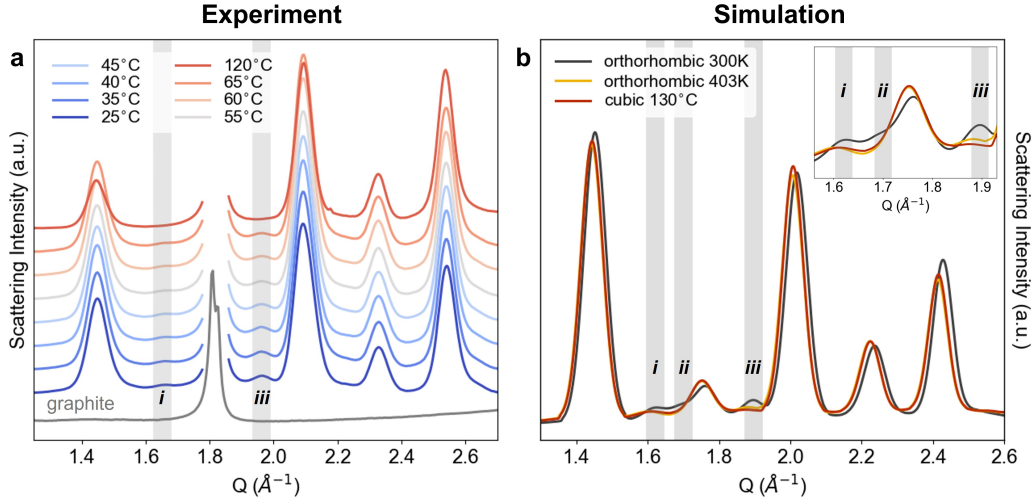
Figure 2.2: Temperature-dependent XRD patterns. (a) Experimental XRD pattern as a function of the temperature from 25 °C to 120 °C. The sharp feature at 1.827 Å⁻¹ originates from the graphite peak enclosing the sample. The shaded grey areas mark the region of the *(i)* and *(iii)* superlattice peaks, which disappear upon temperature increase. (b) Average XRD patterns predicted from the MD simulations at: 27 °C with orthorhombic starting geometry (grey), 130 °C with orthorhombic starting geometry (orange) and 130 °C with cubic starting geometry (red). The shaded grey areas highlight the *(i),(ii),(iii)* superlattice peaks. Inset: zoom into the 1.55-1.94 Å⁻¹ region of the superlattice peaks.

in the long-range despite the thermal motion of the lattice. Instead, a strong reduction or complete disappearance of the superlattice peaks occurs for both MD at 130 °C, together with a slight shift of the main reflections towards lower scattering vectors. The structural differences between the three MD simulations were characterized by computing the statistical distribution of the Pb-Br-Pb angles in the system, projected along the XZ plane of the lattice. We averaged the results of the last 5 ps of each dynamics, making sure that the MD calculations reached convergence. This angle quantifies the degree of local PbBr₆ tilting in the system due to the thermal dynamics. In Figure 2.3a we show the statistical probability of the tilting as a function of the angle, reported as the difference between 180° and the Pb-Br-Pb angle projected along the XZ plane. In this reference system, any angular distortion with respect to the perfect cubic structure implies a deviation from 0°.

The low temperature orthorhombic structure shows a wide bimodal distribution of the Pb-Br-Pb angle peaked at symmetric positions of ±15°. Upon temperature increase, a drastic change in the Pb-Br-Pb statistics occurs. Both 130 °C simulations are characterized by a broad monomodal distribution centred at 0°. The statistical weight of strongly distorted configurations remains relevant, with extreme absolute values up to 40-60°, similar to what is observed for the orthorhombic structure at 27 °C.
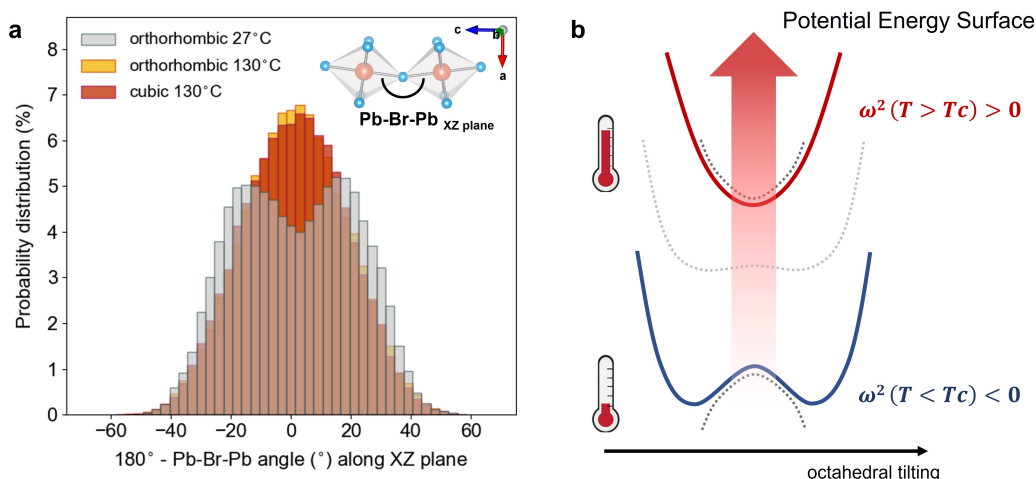
Figure 2.3: Theoretical predictions of the MD simulations. (a) Probability distribution (%) of the Pb-Br-Pb angle as a function of the angle distortion: 27 °C with the orthorhombic starting geometry (grey), 130 °C with the orthorhombic starting geometry (orange) and 130 °C with the cubic starting geometry (red). The angle Pb-Br-Pb is projected along the XZ plane, locally describing the octahedral tilting of the Pb-Br inorganic framework. The x-axis reports the difference between 180° and the Pb-Br-Pb angle projection along the XZ plane in order to centre the distribution at 0°. The average is performed over all Pb-Br-Pb angles of the 6x6x6 supercells and over the time steps of the last 5 ps of the MD simulations, when the system has converged to the global minimum of the MD. Inset: graphical representation of the Pb-Br-Pb angle in the plane defined by the a and c crystallographic axes (XZ plane). (b) Schematic of the Potential Energy Surface evolution with the temperature along the soft phonon coordinate of the octahedral tilting. The frequency of the soft phonon mode is temperature-dependent due its strong anharmonicity [3]. Upon temperature increase, from bottom to top, the potential landscape along this mode changes, causing the displacive phase transition. At temperatures below the phase transition temperature (T_C), the high symmetry position with tilting angle equal to 0° corresponds to a saddle point ($\omega^2_{softmode}$ <0), and the octahedral tilting stabilizes the system (orthorhombic and tetragonal phases). Above T_C, the potential energy surface becomes parabolic ($\omega^2_{softmode}$ >0) and the energy minimum is displaced from the tilted position into the high symmetry position at 0°. The corresponding probability distribution is modified with the temperature, changing from bimodal to monomodal across the phase transition, as shown in panel (a).

2.4.2 Temperature-dependent X-ray absorption spectroscopy

The thermally-induced local structural modifications in CsPbBr$_3$ NCs were monitored with temperature-dependent XAS at the Br K-edge. The experiment is compared with accurate *ab-initio* simulations for two different lattice structures of the system: an orthorhombic configuration describing the room temperature structure and a cubic lattice which approximates the high temperature phase. For both cases, we used the atomic coordinates available in the literature [21]. The computations were performed using 2x2x2 supercell structures and explicitly account for the screened core-hole effect on the XAS spectra, following a strategy that was proven to precisely reproduce Br K-edge spectra for the CsPbBr$_3$ system [91].
Being an element-selective technique, XAS allows to inspect the local environment surrounding the selected sites, in this case the Br centres. The structural changes due to the temperature

increase affect the XAS line shape, both at pre-edge energies [94] and in the spectral region above the ionization limit corresponding to the edge. Starting from the edge, the XAS signal originates from single and multiple scattering events of the photoelectron, and it contains information about the angles and the bond distances between the probed site and its nearest-neighbours [45; 46].

In Figure 2.4a, we report the Br K-edge experimental XAS spectra obtained at 25 °C and 120 °C, and the simulations for the orthorhombic and cubic structures. All curves were scaled by their underlying areas. The experimental spectra show a first peak at the Br edge (the so-called white line, at 13.472 keV), related to the Br 1s-4p electronic transition, followed by post-edge modulations peaked at the energies 13.4875 keV and 13.510 keV. The temperature rise from 25 °C to 120 °C implies an intensity decrease of the main features and an intensity increase of the local minima, with an overall effect corresponding to an apparent broadening of the spectral features. The computed spectrum for the orthorhombic structure reproduces all main features, even though with deviations in their relative intensities. The simulation for the cubic structure shows one additional feature at 13.498 keV and significant intensity variations of the main peaks, which are discussed in the following.

In order to isolate the spectroscopic changes induced by the temperature increase, Figure 2.4b shows the spectral differences obtained by subtracting the experimental spectrum at 25 °C from the 120 °C spectrum, and by subtracting the simulated orthorhombic spectrum from the simulated cubic spectrum. The latter reflects the spectral changes expected under the hypothesis of a local symmetry increase with the temperature. The experimental data show a broad negative feature in the rising-edge region at energies 13.466-13.478 keV, with a global minimum at the edge position at 13.472 keV. A pronounced modulation is observed up to 50 eV above the edge, with damped positive and negative features, respectively, peaked in the local minima and maxima of the steady-state spectrum. Conversely, the simulated difference shows two positive peaks at 13.470 keV and 13.483 keV, and a negative band between 13.4725 and 13.480 keV, followed by smaller post-edge modulations at higher energies. The first three features, completely absent in the experimental differences, can be traced back to the main changes occurring upon the symmetry increase: for the cubic structure both the white line and the second higher maximum of the Br K-edge spectrum become sharper with respect to the orthorhombic simulation. Since the spectral weight is preserved (the area underlying the two curves is the same), an intensity increase of the maxima leads to a depletion of the local minima, in direct contrast with the experimental observations upon temperature increase.

2.5   Discussion

The CsPbBr$_3$ high temperature phase (T=120 °C in Figure 2.2a) has often been ascribed to a high symmetry structure, mainly because its XRD pattern could be reproduced assuming a static cubic lattice configuration, as reported in Figure 2.1b (top panel). However, our MD results at 130 °C show, to our knowledge for the first time in this system, that dynamically disordered structures can effectively describe the high temperature XRD pattern, and specifi-
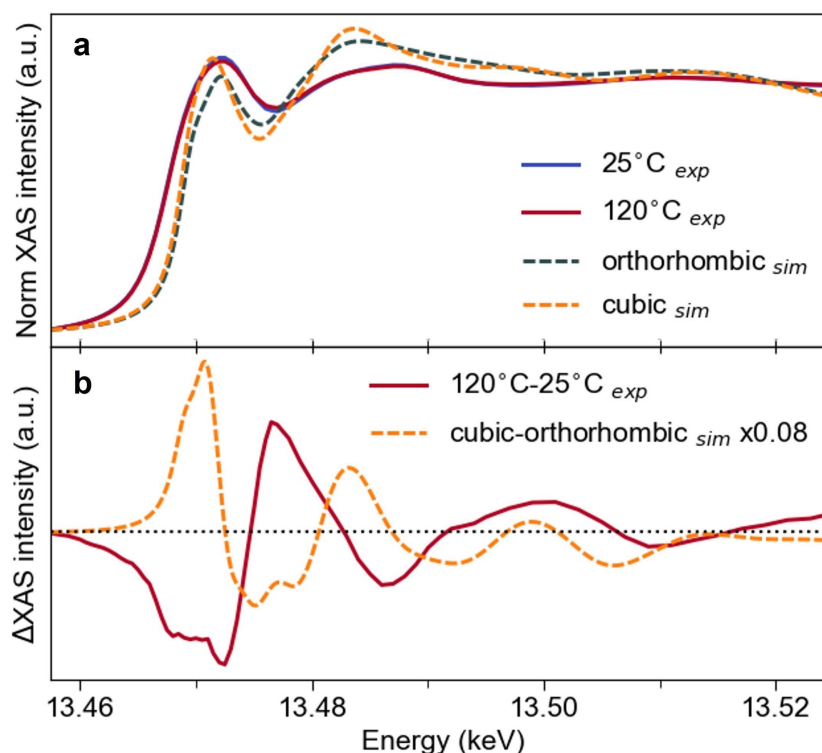
Figure 2.4: Temperature-dependent XAS at Br K-edge and theoretical *ab-initio* calculations. (a) Experimental Br K-edge spectra at 25 °C (blue) and at 120 °C (red), and computed XAS spectra for the orthorhombic (dashed grey) and cubic (dashed orange) structures. All spectra were scaled by their underlying areas. (b) Br K-edge XAS differences for 120 °C minus 25 °C (experiment, red) and cubic minus orthorhombic (dashed orange, simulation). A 3-point adjacent averaging of the energy axis was performed for experimental thermal difference, whereas the simulated spectral difference was multiplied by a factor x0.08 to enable a straightforward comparison of its line shape with the experiment.

cally the disappearance of the *(i)*, *(ii)*, *(iii)* superlattice peaks. The presence of the three XRD superlattice peaks in CsPbBr$_3$ is a characteristic feature of the orthorhombic phase, which is related to the regular periodicity of the cooperative octahedral tilting in the crystal. Our finding demonstrates that the disappearance of these superlattice peaks is caused by the breaking of the long-range tilting, an effect that we ascribe to pronounced thermal fluctuations of the crystal rather than an increasing order in the system.

Indeed, the MD simulations show that the lattice becomes dynamically more active and disordered with the temperature, as observed in the statistical displacement of Cs, Pb and Br sites with respect to their average positions (see Figure 2.6 in the supplementary information section 2.7.2). The analysis of the Pb-Br-Pb distribution as a function of the tilting angle in Figure 2.3a highlights that the temperature increase mainly affects the centre of the distribution, *i.e.* the distortions of the Pb-Br-Pb bond in proximity of the regular cubic geometry. Thus, the data do not reflect a static symmetry increase of the lattice, being large amplitude distortions equally present at low and high temperatures. This result is also confirmed by the agreement between the MD calculations at 130 °C for both orthorhombic and cubic geometries. The

Chapter 2. Local disorder in the CsPbBr$_3$ high temperature phase: the role of thermal fluctuations and phonon anharmonicity

slight differences between the predictions of two simulations can be ascribed to the different boundary conditions imposed in the supercell for the two starting symmetries. Indeed, in both cases the thermal dynamics lifts the original long-range symmetry of the structure and dynamically distorts the lattice.

The absence of a local symmetry increase with the temperature is confirmed by the XAS results in Figure 2.4. Our simulations show that, upon unit cell symmetry changes from orthorhombic to cubic, the Br XAS spectral shape becomes sharper, with features more resolved in energy. Instead, the temperature effect on the experimental spectra causes an overall broadening of the main peaks. If theory predicts opposite changes with respect to the experiment upon an order increase of the lattice, then different structural changes are expected with the temperature rise, suggesting that an order reduction occurs at the local scale rather than a symmetry increase.

Additionally, the comparison between theory and experiment highlights that reducing the local structure of CsPbBr$_3$ to an average cubic cell is inadequate to reproduce the 120 °C XAS spectrum, even though the MD simulations at high temperature show mean structures that are centred in the high symmetry positions. Since the XAS signal originates from the statistical average of all local configurations of the probed sites, at high temperatures this flexible system cannot be precisely described with a unique averaged configuration representative of all local geometries.

This thermal scenario is very different from the light-driven structural changes observed in CsPbBr$_3$ NCs with TR-XAS [91]: upon above band gap excitation, polarons are formed due to the electron-phonon coupling between the photocarriers and the polar inorganic lattice. The crystal distortion involves the activation of one specific longitudinal-optical phonon mode, implying well defined nuclear displacements, which TR-XAS locally determines with atomic scale precision. Combined together, the possibility to computationally reproduce the polaronic distortions and the difficulties in reproducing the thermal effects on CsPbBr$_3$ perovskites demonstrates that: *(i)* high structural precision can be achieved with XAS for this system in the presence of distinct lattice changes, as in the case of the selective activation of one phonon mode via electron-phonon coupling [91]; *(ii)* indirectly proves that the system's configuration at high temperature is very complex and cannot be reduced, at the local scale, to an average ordered structure. To our knowledge, the effect of thermal disorder on the XAS spectra was successfully reproduced only for systems in which the harmonic approximation of the phonon modes is appropriate [94; 95]. At present, a similar procedure becomes computationally unfeasible for largely anharmonic systems such as lead-halide perovskites. This task becomes even more challenging to accurately simulate ligand-stabilized nanostructures, which are characterized by an intrinsic heterogeneity in terms of the size, structure and composition of the system. In this context, employing correlative approaches that join short- and at medium-to-long distance investigations represents a viable strategy to obtain an atomic level description of dynamically disordered systems.

In summary, these results show that an ordered cubic lattice cannot simultaneously reproduce our experimental XRD and XAS data. In light of these observations, we argue with the description of the system's phase diagram in terms of symmetry increasing phases upon

temperature rise. In the literature, subsequent phase transitions in CsPbBr$_3$ single crystals were shown both with structural techniques like XRD [24] and neutron diffraction [87], and with bulk measurements such as differential scanning calorimetry [96] and ultrasonic velocity [97]. These observations of distinct phase transition temperatures partially contrast with the evidence of a temperature-dependent disorder increase in CsPbBr$_3$. Indeed, in inorganic lead-halide NCs, a static disorder increase was reported with increasing temperature, due to a growing density of twinned nanodomains, which would locally preserve the orthorhombic symmetry [19]. Recent Monte Carlo simulations at finite-temperatures, performed using a minimal anharmonic vibrational Hamiltonian parametrized on DFT simulations at zero Kelvin [98], have theoretically described the qualitative features of the phase transitions in CsPbBr$_3$ in terms of pure thermal activation of the lattice [98]. Even in single crystals, thermal local fluctuations in the Pb-Br framework were experimentally shown for CsPbBr$_3$ in its high temperature phase [27]. In the latter study, a zero-frequency Raman peak was observed, which is normally absent in purely harmonic systems. This result points to the presence of strong anharmonicity in the CsPbBr$_3$ lattice, a property related to the lead-halide framework, as it was also observed in MAPbI$_3$ single crystals using the HERIX technique [18]. Similarly, *ab-initio* simulations in the absence of thermal effects showed anharmonic potentials related to the octahedral tilting modes in inorganic lead and tin halide perovskites [99].

A consistent explanation among these contrasting elements on the system's phase diagram is proposed in light of the phonon anharmonicity of the inorganic sublattice. In the past, the study of temperature-dependent phonon anharmonic effects in oxide perovskite systems [100] led to the development of a theory for the explanation of their structural phase transitions [3]. These thermal processes were defined as "displacive" phase transitions, since they imply the presence of a "soft" phonon mode, which vibrates about two different *displaced* mean positions across the phase transition temperature and which is responsible for the overall lattice symmetry change at the critical temperature.

Recently, a temperature-dependent neutron diffraction study reported the presence of a soft mode in an organic lead-halide perovskite single crystal, namely MAPbBr$_3$ [101]. The results were interpreted in terms of displacive thermal phase transitions. Due to the common PbBr$_3$ framework between MAPbBr$_3$ and CsPbBr$_3$, we can rationalize our MD results on the Pb-Br-Pb angle distribution assuming a similar picture to also be valid for all-inorganic lead-bromide perovskites. In this framework, temperature-dependent anharmonic effects modify the Potential Energy Surface (PES) of the system [3] along the PbBr$_6$ tilting mode. Specifically, at low temperature the CsPbBr$_3$ PES corresponds to a double-well potential, explaining the bimodal distribution of the Pb-Br-Pb angle for the MD calculations at 27 °C in Figure 2.3a, peaked at two symmetric tilting values. Upon temperature rise, the PES shape gradually changes into a harmonic potential centred at the high symmetry position corresponding to the cubic geometry, as schematically shown in Figure 2.3b. Such a temperature-induced change accounts for the modification of the Pb-Br-Pb angle distribution observed in our MD simulations at 130 °C: across the phase transition, the nuclei start oscillating around a displaced position, namely the high symmetry position at 0°. However, due to the thermal activation of this low-frequency mode, the octahedral tilting preserves significant distortions from the averaged

cubic geometry, in agreement with the statistically relevant tails of the Pb-Br-Pb distortion in Figure 2.3a.

We remark that our results demonstrated that the temperature-dependent structural changes in the CsPbBr$_3$ system are related to thermally-driven disorder. Therefore, in the proposed framework the presence of the phase transition is rationalized in term of the strong phonon anharmonicity of the Pb-Br sublattice. This proposal accounts for the presence of subsequent phase transitions suggesting a picture that is more complex than a simple symmetry increase of the lattice crystal with the temperature.

2.6 Conclusions

We presented a temperature-dependent investigation of CsPbBr$_3$ NCs using X-ray diffraction and Br K-edge X-ray absorption spectroscopy to characterize the lattice changes taking place across the system's phase diagram. We demonstrate that the highest temperature phase of CsPbBr$_3$ corresponds to a dynamically disordered structure, which on average is centred on the cubic symmetry positions. Through a direct comparison between experiments and refined *ab-initio* simulations, we show that the disappearance of the XRD superlattice peaks upon temperature rise is due to the breaking of the long-range PbBr$_6$ octahedral tilting and not to a symmetry increase of the lattice structure. Thermally-induced changes in the predicted Pb-Br-Pb tilting distribution are explained in terms of temperature-dependent phonon anharmonicity effects. The XAS results confirm that the local structure of the high temperature phase deviates from the orthorhombic and cubic ideal symmetries, due to thermal fluctuations in the lattice, in contrast to the precise distortions induced in the system upon light excitation. These findings show that strongly different lattice responses take place in the system upon thermal and light perturbations, not only clarifying their underlying mechanisms but also offering strategies to control the perovskite nuclear degrees of freedom with different external stimuli. Understanding the thermal processes acting at the atomic level represents the first step towards a rational design of perovskite-based devices with an improved stability.

2.7 Supplementary Information

2.7.1 Time evolution of the Pb-Br-Pb angle distribution in the molecular dynamics simulations

In Figure 2.5 we show the evolution of the Pb-Br-Pb angle distribution as a function of the time for the three MD simulations: 27 °C starting with an orthorhombic symmetry (top), 130 °C starting with an orthorhombic symmetry, 130 °C starting with a cubic symmetry. Data are reported as the difference between 180° and the Pb-Br-Pb angle projection along the XZ plane in order to centre the distribution at 0°. The simulation at 27 °C shows an initial widening of the angular distribution, which completes within the first 200 fs. This effect is due to the thermal dynamics process, which distorts the lattice with respect to the ideal
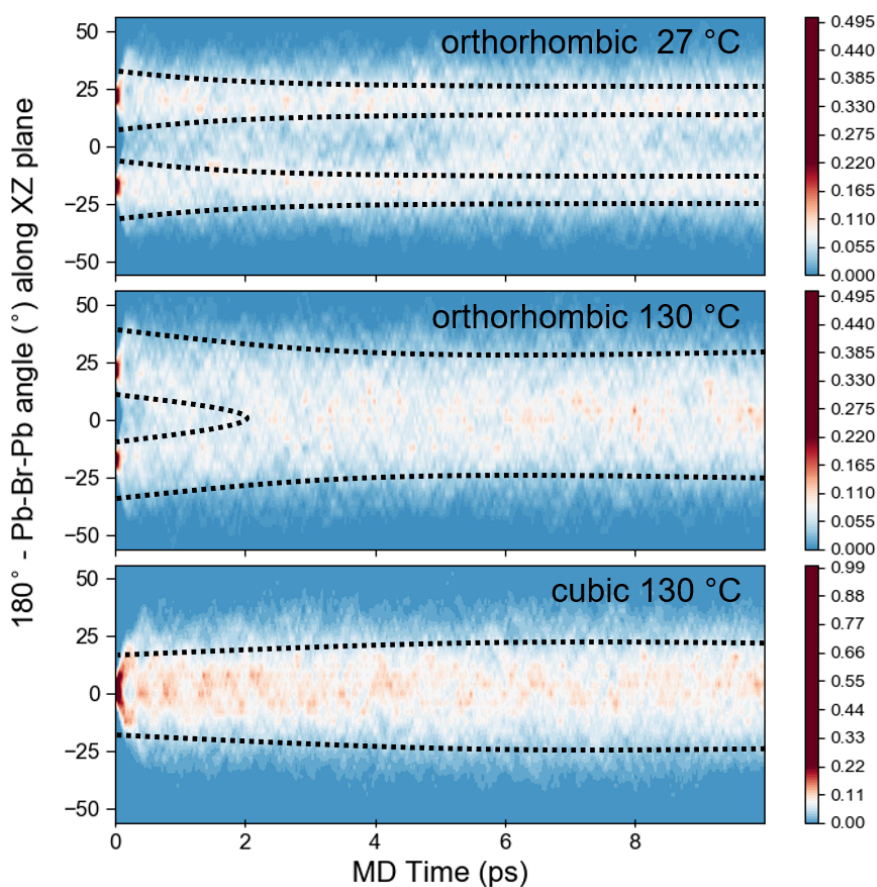
Figure 2.5: Time evolution of the Pb-Br-Pb distribution along the XZ plane during the MD simulations. (top) MD at 27 °C starting from an orthorhombic crystal structure; (middle) MD at 130 °C starting from an orthorhombic crystal structure; (bottom) MD at 130 °C starting from a cubic crystal structure. The y-axis reports 180° minus the Pb-Br-Pb angle projection along the XZ plane in order to centre the distribution at 0°. The z-axis shows the probability to find a given angle for the Pb-Br-Pb projection on the XZ plane as a function of the time. The dark dashed lines serve as guides for the eyes.

orthorhombic structure imposed in the MD simulation at time zero. In the subsequent MD times, the distribution dynamically fluctuates, retaining the maxima in the symmetric positions around $\pm 15°$, corresponding to the octahedral tilting cooperatively kept by the $PbBr_6$ units in the orthorhombic structure. For the MD simulations at 130 °C, the initial structure relaxes towards an energetically more stable configuration in longer times. During the first 2 ps, the orthorhombic structure at 130 °C evolves from a bimodal distribution towards a broad monomodal distribution centred at 0°. Instead, the structural relaxation of the cubic structure at 130 °C completes in the first 300 fs of the MD, and it consists in simple broadening of the distribution due to thermal lattice dynamics. For MD times above 4 ps, the high temperature configurations are analogous, characterized by a Pb-Br-Pb distribution centred in the high symmetry cubic position (0°), but with significant distortions of the octahedral tilting angle.
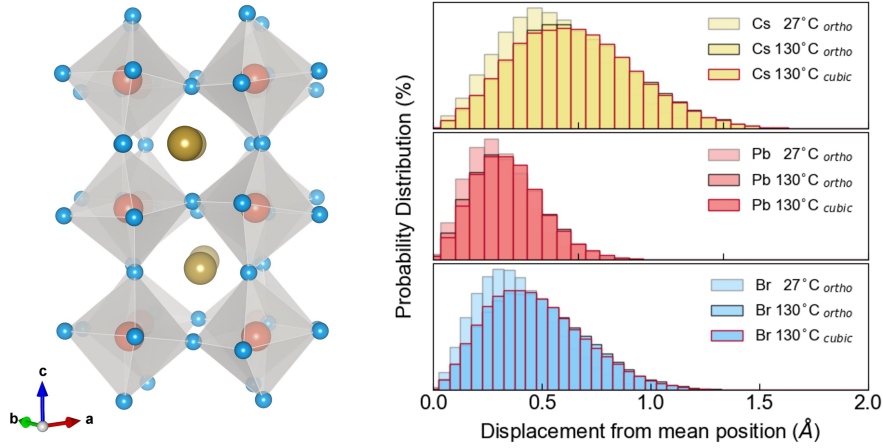
Figure 2.6: Theoretical predictions of the MD simulations. Probability distribution (%) of site displacement (Å) from the average position over the last 5 ps of the MD simulations, in the three cases: 27 °C for the orthorhombic starting geometry (grey boxing), 130 °C for the orthorhombic starting geometry (black boxing) and 130 °C for the cubic starting geometry (red boxing). Top - Cs atom (yellow); middle - Pb atom (light red); bottom - Br atom (light blue). The atoms are color-coded with the graphical representation of the orthorhombic structure reported on the left.

2.7.2   Thermal displacements of the Cs, Pb, Br sites

The thermal dynamics of the Cs, Pb, and Br sites was quantified as a function of the temperature through the probability distribution of the site displacement with respect to their mean position in the MD structure, as reported in Figure 2.6. The results were averaged over the last 5 ps of the MD simulations, when the structures have relaxed into the configurations of minimum energy. We observe that the Cs fluctuations are significantly active already at room temperature ($< \Delta r_{Cs}^{27°C} >$=0.62 Å) and they increase with the temperature ($< \Delta r_{Cs}^{130°C} >$=0.73 Å, +18% upon temperature increase). This result confirms the wide mobility of the inorganic A$^+$ cations in their cuboctahedral voids [17]. The Pb thermal dynamics is only slightly perturbed by the temperature increase ($< \Delta r_{Pb}^{27°C} >$=0.33 Å, $< \Delta r_{Pb}^{130°C} >$=0.38 Å). Instead, Br centres exhibit significant changes in their mobility with the temperature, showing that thermal lattice dynamics of the Pb-Br framework is dominated by the Br displacements ($< \Delta r_{Br}^{27°C} >$=0.59 Å, $< \Delta r_{Br}^{130°C} >$=0.73 Å, i.e. +24% upon temperature increase). These observations highlight the increased thermal dynamics associated with the phase transition from room temperature to 130 °C.

3 | Femtosecond dynamics in spinel Co$_3$O$_4$

3.1 Introduction

Transition metal oxides (TMOs) have been increasingly studied as promising systems for photovoltaic and photocatalytic processes [102–105], especially for their stability, tunable band gaps and earth-abundance. Although most optoelectronic applications rely on exploiting the charge carriers that are photogenerated upon above band gap excitation, the understanding of the fundamental processes underlying the relaxation dynamics of the photocarriers in these materials prior to charge separations is still poorly understood.

Compared to conventional semiconductors such as Si and Ge, which have fully occupied orbitals and purely covalent bonds, TMOs are characterized by chemical bonds with a stronger ionic character and partially filled d-orbitals that are localized on the metal centres. The complex lattice and electronic structure of these systems makes their photodynamics particularly rich, with correlated responses among the electronic, spin and nuclear degrees of freedom.

Co$_3$O$_4$, which represents a prototypical case of the intrinsic complexity of TMOs, has been studied for its thermodynamic stability, making it a good candidate for catalytic activity of CO oxidation [106], water splitting reaction and solar energy conversion [107; 108]. The Co$_3$O$_4$ lattice has a normal spinel structure (space group $Fd\bar{3}m$) where the O^{2-} anions form a close-packed face centred cubic lattice. The stoichiometry of the crystal implies the presence of two different oxidation states, Co^{2+} and Co^{3+}, which are respectively located in the tetrahedral and octahedral voids of the oxygen network with a 1:2 ratio (Figure 3.1(left)). As a consequence of their local symmetry, the crystal field splitting for these sites determines the presence of 6 paired electrons on the Co^{3+} T$_{2g}$ orbitals, and 4 paired and 3 unpaired electrons respectively in the e$_g$ and t$_{2g}$ orbitals of the Co^{2+} centres (Figure 3.1(right)). As such, the Co^{2+} sites have a
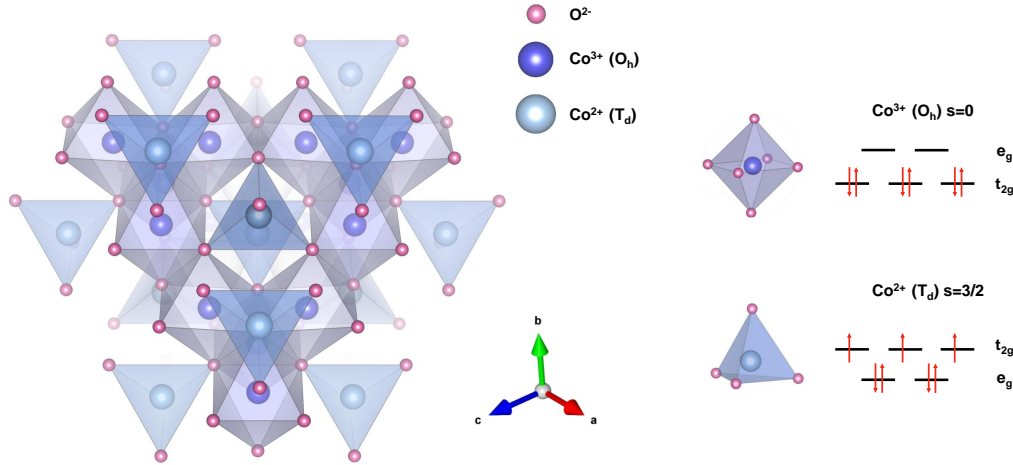
Figure 3.1: (left) Co$_3$O$_4$ cubic spinel lattice structure. The Co^{2+} tetrahedra and the Co^{3+} octahedra are reported in blue and grey respectively. (right) Co^{2+} (d^7) and Co^{3+} (d^6) electronic configuration.

spin s=3/2 which determines the presence of an antiferromagnetic ordered phase below 40 K, where each spin-active Co^{2+} centre is surrounded by four nearest-neighbours Co^{2+} sites with oppositely directed spins [109]. The band structure predicted by density functional theory (DFT) computations consists in a valence band (VB) with similar weights from the O (2p), Co^{2+} d and Co^{3+} d orbitals, whereas the bottom of the conduction band (CB) is mainly composed of Cobalt d orbitals [110]. The complexity of the band structure composition determines the presence of Mott-Hubbard and charge transfer gaps close in energy, resulting in the rich optical spectrum reported in Figure 3.2. The entire spectrum comprises four main peaks at wavelengths 440 nm, 745 nm, 1320 nm, 1500 nm, respectively from blue to the red. The exact assignment of the absorption peaks to specific electronic transitions is still unclear [111–113], but there is general consensus on ascribing the peak at 440 nm to ligand-to-metal charge transfer (LMCT) excitations of the electrons from the O^{2-} (2p) orbitals of the VB to the empty orbitals of the Cobalt sites, specifically O^{2-} (2p)→ Co^{2+} (t$_{2g}$) at lower energies and O^{2-}(2p) → Co^{3+}(e$_g$) at higher energies. The peak at 745 nm was assigned to a metal-to-metal charge transfer (MMCT) transition from the Co^{3+} to the Co^{2+}, creating a pair of Cobalt ions with oxidation states Co^{4+} and Co^{1+}. The weak absorption band at 1320 nm was ascribed to the reversed MMCT process, generating a new pair of Cobalt centres in which a Co^{3+} ends up in tetrahedral sites and a Co^{2+} occupies an octahedral site. The feature at 1500 nm was related to a ligand field d-d transition of the Co^{2+} centre. Few time-resolved studies were conducted on spinel Co$_3$O$_4$. A pump-probe investigation exciting the system at 400 nm and probing the Co M$_{2,3}$ edges in the extreme ultraviolet (XUV) was performed to explore its early dynamics, up to 2 ps, with element and oxidation-state specificity [114]. The authors provided evidence of a prompt electronic transition involving an O^{2-} (2p) to Co^{3+} (e$_g$) charge transfer, followed by two sub-ps relaxation processes, which were respectively ascribed to Auger recombination (190±10 fs) and charge carrier cooling (535±33 fs). Another study confirmed the presence of transient signals upon 400 nm excitation of Co$_3$O$_4$ at the O L$_1$-edge but details on the photo-
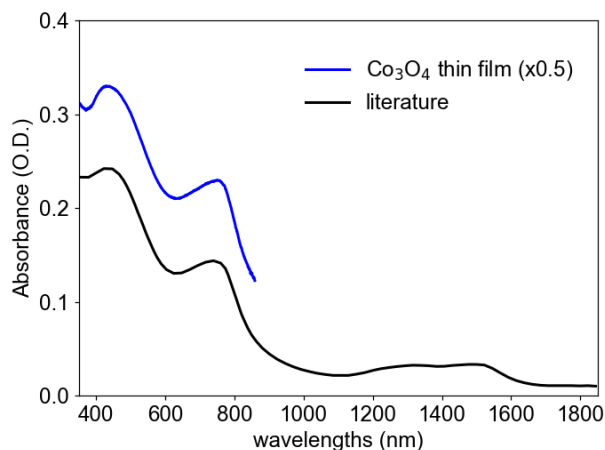
Figure 3.2: UV-Visible spectrum of a 27 nm Co_3O_4 thin film grown on top of sapphire substrate (blue), compared with the extended optical spectrum up to the near infrared (NIR) region reported in the literature (black) [4].

dynamics were not provided [115]. High harmonic generation (HHG) transient absorption at the Co $M_{2,3}$ edges was also exploited to investigate charge carrier recombination processes of the system at longer time scales [116]. Relaxation to the ground state was observed with time constants of 1.9 ns and 600 ps, respectively for thin films in vacuum and in methanol environment. Finally, the ps dynamics of Co_3O_4 was studied in the visible domain upon selective photoexcitation of all the major optical transitions, pointing to the filling of common d-d final states independently of the excitation wavelength [4]. These states represent recombination centres that live up to hundreds of ns. Although these accurate investigations clarified several aspects of the Co_3O_4 photodynamics, details about the ultrafast relaxation processes upon different light excitations are still missing. In fact, the mechanisms bringing the optically generated charge carriers from the ligand-to-metal or metal-to-metal charge-transfer gap into the d-d states of the Mott-Hubbard gap have not been elucidated yet.

A deeper understanding of the complex photodynamics of Co_3O_4 requires using complementary approaches to selectively probe its electronic response and to correlate it with the changes in the spin and nuclear degrees of freedom. In this framework, we started a measurement campaign combining tabletop ultrafast measurements in the visible domain with large scale facility X-ray experiments. Specifically, we explore the study of Co_3O_4 thin films upon selective excitation of the LMCT and MMCT transitions with both time-resolved X-ray diffraction (TR-XRD), to track the nuclear dynamics of the system, and time-resolved X-ray emission (TR-XES), which is an element-selective technique sensitive to the spin, oxidation state and local geometry of the probed sites.

In the following, we report the careful characterization of the sample with dedicated XRD and XES measurements at the synchrotron, which are essential to pursue ultrafast X-ray experiments at free electron lasers (FELs). We start the chapter presenting steady-state measurements of our Co_3O_4 thin films. We employed UV-Visible and X-ray absorption spectroscopy to ensure the quality of the sample in terms of composition and stoichiometry. We also present

the results of resonance Raman spectroscopy, exploited to study the ground state vibrational response of the system under different excitation wavelengths, and a XRD investigation at the synchrotron to detect the diffraction peaks, which are most sensitive to the coherent phonon modes activated upon ultrafast excitation. The results of a synchrotron XES study are discussed, in which we determined the experimental conditions to detect strong emission signal, still preventing sample damaging under X-ray light exposure. We then focus on ultrafast time-resolved reflectivity measurements. The latter represents the first femtosecond transient experiment on spinel Co_3O_4 in the visible domain, pumping the material at 400 nm and 800 nm and probing it in the 450-750 nm range. The high temporal resolution (65 fs) and broadband detection of the set-up allow us to study the initial steps of the system's photodynamics, observing significant differences in the relaxation processes of LMCT and MMCT transitions. We report strong changes in the incoherent electronic and coherent nuclear responses prior to the population of the same final d-d states, ruling out the hypothesis of a relaxation cascade bringing the photocarriers from the highest LMCT to the lowest d-d gap through an intermediate MMCT state. We finally present preliminary results of 400 nm pump/femtosecond XES probe at the Co $K_{\alpha1,2}$ emission lines of Co_3O_4 thin films at the European X-ray free electron laser (EXFEL). Combined together, our findings suggest the presence of two distinct relaxation channels upon excitation of the system at 800 nm and 400 nm, the latter possibly related to an ultrafast intersystem crossing process, a rare phenomenon in solid state materials.

3.2 Methods

3.2.1 Sample preparation and characterization

Performing TR-XRD and TR-XES experiments at a FEL require an *ad-hoc* design of the sample. Differently from gas and liquid phase, pump-probe X-ray experiments on solid state systems impose highly demanding boundaries on the sample preparation side, as discussed in the following.

3.2.1.1 Sample thickness

Visible and X-ray light have very different absorption coefficients in materials. In an optical-pump/X-ray-probe experiment, the strong mismatch in penetration depth between the pump and probe pulses requires a careful choice of both sample thickness and experimental geometry to be employed, generally a grazing incidence configuration.
Indeed, in normal incidence geometry the penetration depth of the optical pump at 400 nm and 800 nm in Co_3O_4, respectively, corresponds to 29 nm and 144 nm, as computed based on the extinction coefficient reported in the literature from ellipsometry measurements [113]. The X-rays are bulk sensitive and have penetration depths that vary with the photon energy. Based on the predictions of the Center for X-Ray Optics (CXRO) of the Lawrence Berkeley National Laboratory's Materials Sciences Division [117], for our sample (27 nm Co_3O_4 film on
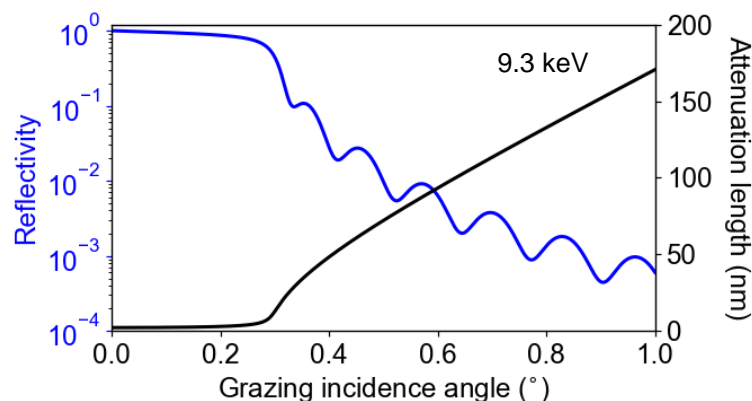
Figure 3.3: CXRO predictions of reflectivity (blue, left y-axis) and attenuation length in nm (black, right y-axis) as a function of the grazing incidence angle for an X-rays energy of 9.3 keV. A 27 nm Co_3O_4 film (density=6 g/cm^3) on top of a 5 mm Al_2O_3 substrate (density=3.98 g/cm^3) was considered in the calculations.

top of 5 mm Al_2O_3 substrate) X-ray photons at 9.3 keV have an attenuation length of about 10 μm in normal incidence geometry. Under these conditions, the X-ray signal collected from a single crystal would essentially come from the unpumped bulk of the sample, strongly reducing the contrast of a pump-probe measurement. We overcome this issue by designing a thin film with a thickness matching the penetration depth of the optical light, namely 27 nm. On a thin film, a normal incidence geometry implies that most of the X-ray photons are transmitted through the film and they are absorbed by the substrate, causing unnecessary thermal load on the sample. Keeping the X-ray flux constant, the probe photon fluence can be reduced setting the experimental conditions in grazing incidence geometry. In this configuration, the penetration depth of the optical pump changes following Snell's law. For small incidence angles (<5-10°), the refracted angle is almost constant, and the penetration depths are very close to the normal incidence ones, respectively 27 nm and 137 nm for 400 nm and 800 nm. For the probe, the attenuation length as a function of the grazing incidence angle is obtained following CXRO predictions (Figure 3.3). We observe a strong dependence of the attenuation length with the angle of incidence, with values of tens of nm obtained only for very shallow angles below 0.5°. Thus, the two conditions of (i) minimization of the thermal load coming from the X-rays and (ii) matching of the pump and probe penetration lengths are achieved for angles between 0.3° and 1°, which are experimentally challenging to realize. With respect to normal incidence, the sample reflectivity at shallow angles also significantly changes. For angles above 0.3°, the X-ray reflectivity is kept below 10% and does not affect much the experimental conditions of the measurements (Figure 3.3). In the visible, the optical reflectivity is computed following Fresnel's law for 400 nm and 800 nm pump light, as shown in Figure 3.4. The optical reflectivity and the increased footprint of the pump spot-size on the sample in grazing incidence implies a significant reduction of the effective excitation fluence when the pump energy is kept constant.
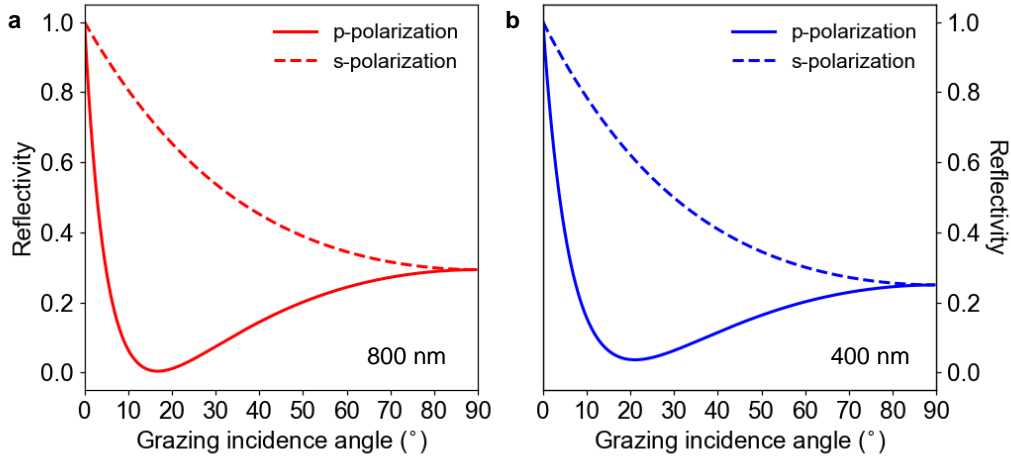
Figure 3.4: (a,b) Reflectivity as a function of the grazing incidence angle respectively for 800 and 400 nm light with s- (dashed) and p-polarization (full).

3.2.1.2 Sample growth

A consequence of the thin film choice is the limited flexibility in the sample orientation, with the out-of-plane crystallographic direction constrained by the employed synthetic method. As will be explained in section 3.2.3, we have verified the compatibility between the sample growth direction and the experimental conditions of a planned time-resolved X-ray diffraction (TR-XRD) experiment. The Co$_3$O$_4$ film was synthetized by our collaborators Dr. Natacha Ohannessian and Dr. Daniele Pergolesi in the Thin Films and Interfaces Group of the Paul Scherrer Insitute (PSI). The sample consists of a 27 nm Co$_3$O$_4$ thin film epitaxially oriented along the (111) direction on top of a (0001) sapphire substrate prepared with pulsed laser deposition [118]. Particular attention was made in ensuring the monocrystallinity of the pure spinel phase and the absence of other phases of stoichiometric Cobalt oxide.

3.2.1.3 Resonance Raman measurements

In order to provide a deeper interpretation of the time-resolved reflectivity data that will be discussed in section 3.3.1, we characterized the steady-state Raman response of Co$_3$O$_4$ under resonance conditions. Even though the Raman scattering response of spinel Co$_3$O$_4$ was already subject of some works [119–121], these studies were limited to resonance conditions with the LMCT excitation only, and explored Raman shift energies up to the lowest wavenumbers of 100 cm^{-1}. However, due to the selective enhancement of the Raman features under resonance excitation, a proper characterization of the Raman active modes possibly activated in the pump-probe measurements *via* impulsive stimulated Raman scattering (ISRS, refer to section 3.2.2.1 for more details) requires comparing spectra obtained upon excitation of both LMCT and MMCT optical transitions. Specifically, we measured resonance Raman spectra in the 40-840 cm^{-1} energy loss region, exciting the sample at 532 nm and 785 and using a LabRAM
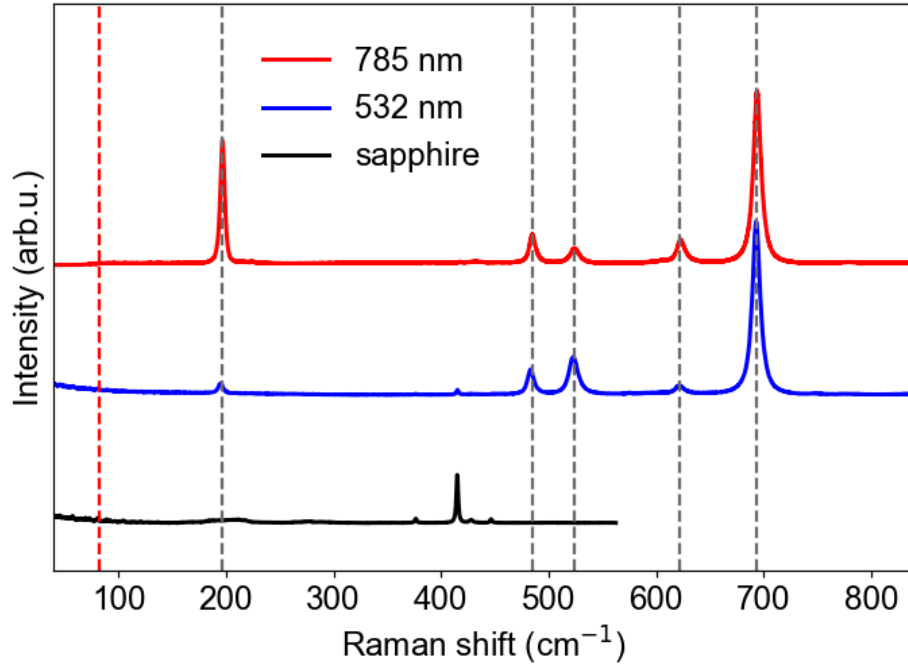
Figure 3.5: Co_3O_4 Raman spectrum obtained upon 785 nm and 532 nm excitation wavelengths. An arbitrary offset was introduced along the vertical axis, and the spectra Co_3O_4 were normalized by the intensity of the 694 cm^{-1} feature. The pure sapphire substrate (λ_{exc}=532 nm) is shown in black, scaled by an arbitrary factor to highlight the presence of a peak at 415 cm^{-1}. The dashed gray lines mark the Raman shift position of the modes with energy (symmetry): 196 cm^{-1} (T$_{2g}$), 482 cm^{-1} (E$_g$), 524 cm^{-1} (T$_{2g}$), 622 cm^{-1} (T$_{2g}$), 694 cm^{-1} (A$_{1g}$). The dashed red line highlights the absence of any Raman feature at 82 cm^{-1}.

HR Raman spectrometer available in the Earth and Planetary Science Laboratory of the École Polytechnique Fédérale de Lausanne. The results are reported in Figure 3.5. Consistent with the factor group analysis on the normal spinel structure, which predicts the presence of 5 Raman active modes [122], namely one A$_{1g}$, one E$_g$ and three T$_{2g}$ modes, our spectra consist of five Raman peaks, highlighted with dashed grey lines. Following the assignment reported in polarization dependent measurements [119], they correspond to the symmetries: T$_{2g}$ (196 cm^{-1}), E$_g$ (482 cm^{-1}), T$_{2g}$ (524 cm^{-1}), T$_{2g}$ (622 cm^{-1}), A$_{1g}$ (694 cm^{-1}). We note the presence of a faint feature at 415 cm^{-1} originating from the sapphire, as confirmed by a separate measurement of the pure substrate. The Co_3O_4 spectra were scaled by the intensity of the A$_{1g}$ peak at 694 cm^{-1} and show a strong dependence of the electron-phonon matrix elements from the excitation wavelength. In particular, we notice a significant increase in the relative intensity of the Raman mode at 196 cm^{-1} changing the excitation from 532 nm to 785 nm. DFT calculations of the Raman active phonons in Co_3O_4 showed that the T$_{2g}$ mode is associated with a substantial shortening of the Co-O bond in the tetrahedral units, with minor off-axis distortions of the apical Oxygens surrounding the octahedral Co^{3+} sites [120]. As we will show in section 3.3.1, upon 800 nm excitation the phonon mode at 196 cm^{-1} strongly couples with the photogenerated charge density *via* the ISRS mechanism. Conversely, exciting
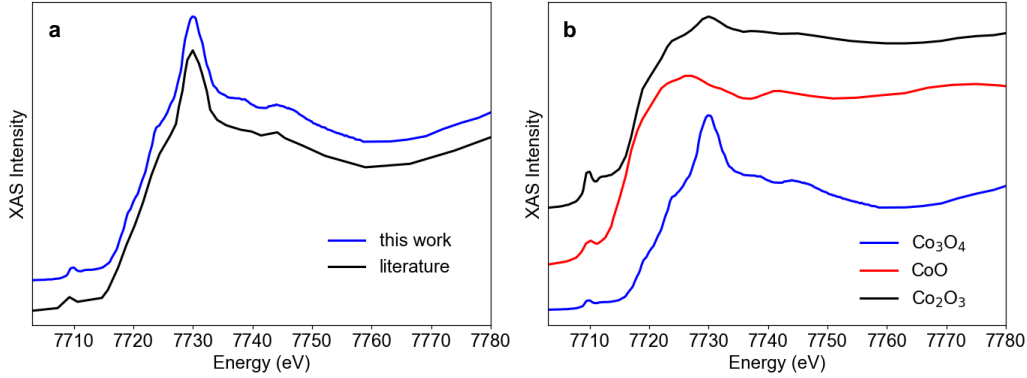
Figure 3.6: (a) XAS spectrum of the 27 nm thick Co$_3$O$_4$ film compared with the data reported in the literature [5]. (b) XAS spectra comparison of the Co$_3$O$_4$ thin film and of two reference standards containing Co^{2+} (CoO) and Co^{3+} (Co$_2$O$_3$) sites only. The spectra were normalized by the maximum intensity and an offset was introduced along the vertical axis.

the system with a 400 nm pump pulse, coherent phonons oscillating at 82 cm^{-1} are generated, a frequency that does not correspond to any Raman active mode of the ground state system, as highlighted by the red dashed line in Figure 3.5.

3.2.1.4   X-ray absorption spectroscopy measurements

The quality of the pure spinel phase of our Co$_3$O$_4$ thin films was confirmed with a steady-state XAS characterization performed at the MicroXAS beamline at the Swiss Light Source (SLS). These measurements will also be useful to guide future optical pump/X-ray probe experiments under resonance conditions with the Cobalt K-edge transition. The XAS signal was measured in fluorescence geometry, with the sample and the detector respectively at 45° and 90° with respect to the incoming X-ray beam. A Ketek detector was used for the XAS measurements across the Cobalt K absorption edge (7.700-7.780 keV), exploiting its energy resolution of about 150 eV to exclude the elastic scattering signal and isolate the Cobalt fluorescence lines. The spectra were collected using a Si(311) crystal monochromator. The X-ray energy was calibrated using a Cobalt foil. The intensity was corrected by the incoming X-ray flux, retrieving a signal that is proportional to the X-ray absorption coefficient in the thin-sample limit [123], a valid approximation, considering the 27 nm sample thickness of our thin film.

The Co K-edge spectrum is reported in Figure 3.6 along with the digitized curve of the Co$_3$O$_4$ sample from the literature [5]. Both spectra were normalized by the maximum intensity and a vertical offset was introduced for better clarity. The faithful correspondence between the two curves in the pre-, main- and post-edge regions confirms the quality of our thin films. The presence of other crystalline phases was further excluded measuring the XAS spectra of two reference Cobalt oxide compounds: CoO (Co^{2+}) and Co$_2$O$_3$ (Co^{3+}).

3.2.2   Time-resolved reflectivity

3.2.2.1   General principles

Time-resolved reflectivity (TRR) is a pump-probe technique sensitive to the photoinduced variation of the sample optical properties as a result of the changes in its dielectric function $\epsilon(\omega)$. Light-driven modifications of the charge carrier density n_e, the electronic temperature T_e, the lattice coordinates Q, or any other relevant parameter, affect the dielectric function and thus induce a modification of the material's reflectivity. The reflectivity changes can be expressed as [124; 125]:

$$\frac{\Delta R}{R} = \frac{\partial \ln R}{\partial \epsilon} \cdot \frac{\partial \epsilon}{\partial n_e} \cdot \Delta n_e(t) + \frac{\partial \ln R}{\partial \epsilon} \cdot \frac{\partial \epsilon}{\partial T_e} \cdot \Delta T_e(t) + \frac{\partial \ln R}{\partial \epsilon} \cdot \frac{\partial \epsilon}{\partial Q} \cdot \Delta Q(t) \tag{3.1}$$

This formulation explicitly shows that TRR can provide information about the electron dynamics, lattice motion and the electron-phonon coupling in the system through time dependent variations of n_e, T_e, and Q [124; 126–130].

The photoinduced response of the material can be separated into an incoherent and a coherent term, respectively obtained accounting for the first and second order terms in the perturbation treatment of the Hamiltonian describing the light-matter interaction.

The incoherent response of the material occurs upon above band gap excitation and subsequent relaxation of the charge carriers, affecting the dielectric function of the system and thus its reflectivity. On a sub-100 fs time scale, the electron-electron scattering leads to thermalization of the nonequilibrium charge density, which can be described with a Fermi-Dirac distribution characterized by an electronic temperature T_e. Later, on sub-ps times, the excess energy of the photocarriers with respect to the optical band gap is dissipated *via* optical phonon emission, a process mediated by electron-phonon scattering, which leads to charge carrier cooling and equilibration between carrier and lattice temperatures [131]. Eventually, the photocarriers recombine *via* radiative and non-radiative Auger recombination processes, the latter being dominant at high carrier densities [132].

The coherent response of the system is observed only when the ultrafast pump pulse is shorter than the period of the collective excitation, which is possibly launched in the system. In this case, the coherent oscillation of the collective excitation, *e.g.* coherent phonons, introduces a periodic modulation of the dielectric function and the reflectivity [133]. Two different mechanisms underlie the generation of coherent excitations in materials: impulsive stimulated Raman scattering (ISRS) [134; 135] and displacive excitation of coherent phonons (DECP) [125]. A schematic representation of the two processes is shown in Figure 3.7. In ISRS, a coherent vibrational motion is triggered in the electronic ground state potential by the pump laser. This process requires the dependence of the dielectric function on the lattice displacements of the phonon: $\frac{\partial \epsilon}{\partial Q} \neq 0$, *i.e.* the coherently excited phonon must be Raman active. Instead, in a DECP process, the ultrashort pump induces an impulsive shift of the excited state potential energy surface, due to the electron-phonon interaction between the photocarriers and the lattice crystal. In her seminal work on DECP, Dresselhaus *et al.* assumed a linear dependency of the lattice shift from the charge carrier density $n_e(t)$ to describe the generation of totally-
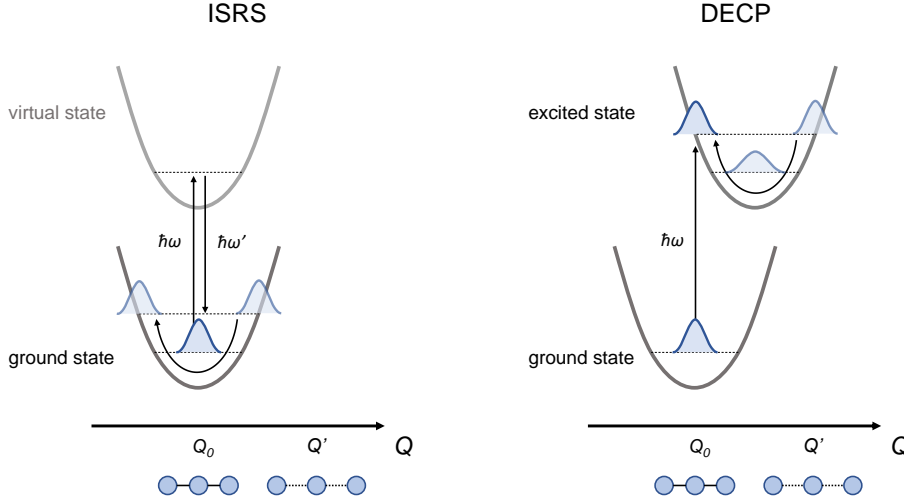
Figure 3.7: Schematic layout for the generation mechanisms of ISRS (left) and DECP (right). In ISRS the coherent dynamics occurs in the ground state electronic potential, whereas in the DECP the coherent response is in the excited state potential energy surface.

symmetric phonon modes upon excitation of conventional semiconductors [125]. The same theory can be extended to phonons with lower symmetry, accounting for the appropriate symmetry components of the carrier density.

Both ISRS and DECP processes manifest as a coherent modulation of the optical properties of the system. The different generation mechanisms can be unravelled from the Raman spectrum (ISRS phonons must be Raman active) and from the relative phase of the oscillations: since the ISRS vibrations start from the equilibrium position of the ground state, they are expected to follow a sine wave as a function of time, DECP phonons, instead, should follow a cosine wave as a function of time, being generated upon impulsive shift of the excited electronic potential energy surface.

3.2.2.2 Laser system and electronics

A femtosecond broadband visible set-up operating at 20 kHz either in absorption or reflection geometry was built to perform the time-resolved optical experiments presented in this chapter.

The layout of the set-up is schematically shown in Figure 3.8. A Ti:sapphire oscillator (Halcyon, KMLabs), pumped by a continuous wave Nd:YVO4 laser (VERDI, Coherent), delivers sub-50 fs pulses centred at 800 nm with a repetition rate of 80 MHz, and is used as a seed for a cryogenically cooled regenerative amplifier (Wyvern500, KMLabs). The amplifier is tandem-pumped by three Q-switched Nd:YVO4 pump lasers (Photonics Industries) and operates at 20 kHz. The resulting output delivers highly stable 50 fs pulses of 6 mJ centred at 800 nm, and typically has shot-to-shot energy fluctuations below 0.1% rms [136]. About 10 μJ of the resulting energy is exploited for time-resolved broadband visible experiments. The p-polarization of the
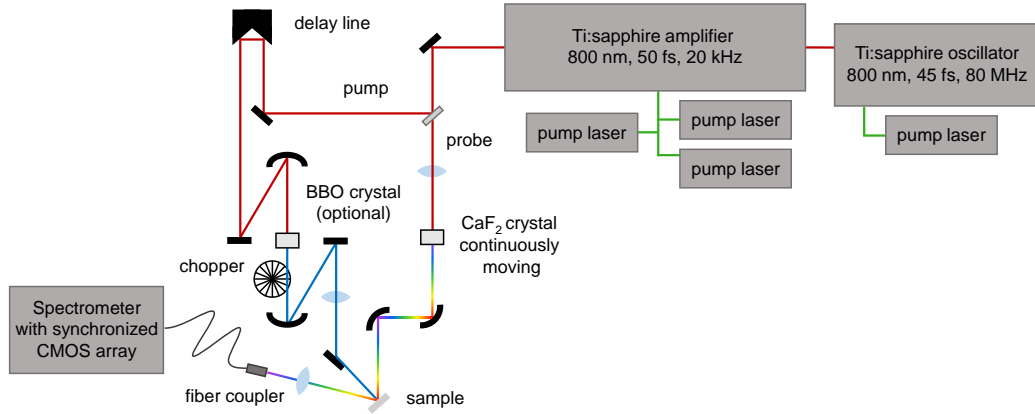
Figure 3.8: Diagram of the 20 kHz laser system and transient reflectivity visible set-up.

incoming laser pulse is selected with a thin polarizer and the beam is split into pump (80%) and probe (20%) branches. The pump beam passes through a motorized delay line, enabling to scan the relative delay between the pump and the probe pulses, and is focused with a 20 cm spherical mirror into a 0.5 mm-thick type I β-barium borate (BBO) crystal to generate 400 nm pulses (optional). Close to the focus position, the pump passes through a 100 blades chopper, operating at 10 kHz and phase-locked to the laser repetition rate (20 kHz), and is then collimated with a second 20 cm spherical mirror. If the pump is frequency doubled, the residual 800 nm intensity is removed with 4 harmonic separators.

The beam is then focused with a lens into the sample in normal incidence geometry, or at 22° incidence angle, respectively when operating in reflection or transmission mode. The probe beam is focused into a 2 mm-thick CaF_2 crystal to generate the visible supercontinuum. The white light quality is optimized by tuning the probe energy to 0.5 μJ with a ND filter, by adjusting the beam numerical aperture with an iris positioned just before the 15 cm focusing lens, and by translating the CaF_2 position along the beam focus with a micrometric manual stage. Crystal damaging and the consequent white light degradation is prevented by continuously moving the CaF_2 at 10 Hz along the vertical direction. Long term damaging is avoided by additionally scanning the crystal along the horizontal direction with a motorized stage. The diverging beam is collimated and focused on the sample with a pair of 90° off-axis parabolic mirrors. The residual 800 nm component is filtered before the sample by a shortpass glass filter. Pump and probe beams are spatially and temporally overlapped on the sample, with typical sizes of 150x150 μm and 60x60 μm, respectively. When operated in reflection geometry, the sample is tilted about 22° with respect to the probe beam and the reflected white light is focused into a 2 m long multi-mode optical fiber placed at 45° with respect to the probe direction, which delivers the probe into a spectrograph.

The broadband pulse is dispersed by a 150 gr/mm holographic grating and the resulting spectrally-resolved signal intensity is measured with a complementary metal-oxide semiconductor (CMOS) array detector (Hamamatsu S11105, 512 pixels, 12.5x250 μm^2 pixel size) synchronized to the data acquisition system. Since the maximum readout rate per spectrum

is almost 100 kHz (each pixel has a readout up to 50 MHz), pumped and unpumped spectra are collected in shot-to-shot detection mode [136]. The readout operation of the CMOS is triggered at 20 kHz repetition rate with a gated signal delivered by a triggering card, which synchronizes the laser amplifier signal (20 kHz) with the 11 MHz master clock of the 16-bit analog-to-digital converter (ACD). A replica of the gated trigger is halved and used to operate the chopper at 10 kHz, phase-locked to the laser amplifier outputs [137].

In the pump-probe experiments, several time scans are repeated in order to improve the signal-to-noise ratio (SNR) of the measurement. For each delay of the time scans, 20000 consecutive shots are recorded, sorted on a shot-to-shot basis into pumped and unpumped spectra, and averaged. In reflectivity mode, the pump-probe signal is computed as:

$$\frac{\Delta R(\omega, t)}{R} = \frac{R_{pumped}(\omega, t) - R_{unpumped}(\omega, t)}{R_{unpumped}(\omega, t)} \tag{3.2}$$

where ω corresponds to the spectrally-resolved frequency of the probe and t is the time delay between the pump and the probe at which the pumped and unpumped signals were collected. The frequency calibration of the spectra was performed measuring the absorption spectrum of both a Holmium reference in solution (Hellma) and the corresponding pure solvent. The reflectivity matrixes from consecutive scans are then averaged together. Since the supercontinuum probe is not dispersion-compensated before reaching the sample, the reflectivity maps have to be chirp corrected. To define the parameters for the group velocity dispersion (GVD) correction, pump-probe measurements on pure sapphire were performed. Indeed, since this substrate does not absorb light at the employed pump (400 nm and 800 nm) and probe wavelengths (450-750 nm), the white light chirp can be precisely defined through the fitting of the coherent artefact signals with a second order polynomial function. The coherent artefact signal is present only at time delays when the pump and probe pulses overlap in time, and its analysis allows to determine the wavelength-dependent time zero position and the instrument response function (IRF) of the set-up, defined as cross-correlation width of the pump and probe pulses.

Both the chirp correction and the global lifetime analysis (GLA) of the pump-probe maps were performed with the Optimus software [138]. Within the GLA approach, the pump-probe time traces at each wavelength ($S_\lambda(t)$) of the 2D map are simultaneously fitted with a sum of exponential functions convoluted with a Gaussian IRF function [138; 139]:

$$S_\lambda(t) = \sum_{i=1}^{n} A_i(\tau_i, \lambda) \cdot \exp(-\frac{t}{\tau_i}) * IRF(t) \tag{3.3}$$

where $A_i(\tau_i, \lambda)$ is the wavelength-dependent amplitude of the exponential decay characterized by the τ_i time constant.

3.2.3 X-ray diffraction

In this section we present the steady-state XRD investigation performed at the Swiss Light Source (SLS) as preparation for the time-resolved measurements envisaged at the EXFEL. Performing a TR-XRD measurement requires a careful evaluation of the experimental geometry in terms of relative position between the sample, the incoming X-rays, and the detector position. As we discussed in section 3.2.1.1, a grazing incidence configuration is envisaged in order to match the penetration lengths of the optical pump and X-ray probe and to minimize the thermal load on the sample. Once the experimental geometry and the X-ray energy are chosen, the in-plane and out-of-plane components of both the thin film and the substrate must be determined in order to define the orientation matrix of the sample and predict the position of the Bragg reflections in the space. Finally, a choice of the XRD peaks to be measured is needed, since the dimensions of most 2D detectors enable probing a single Bragg reflection at the time. In our pump-probe experiment in the visible domain (see section 3.3.1), we show that, upon 800 nm excitation, a coherent phonon at 196 cm^{-1} is activated *via* ISRS mechanism. Thus, we want to identify and characterize the XRD peaks that are sensitive to this specific phonon mode, since for these peaks we expect to see a coherent TR-XRD response when photoexciting the sample.

3.2.3.1 Synchrotron set-up

The XRD measurements were performed on Co_3O_4 thin films at the Surface Diffraction end station of the Material Science beamline of the Swiss Light Source (SLS). The experiment was carried out in grazing incidence geometry, with a 9.3 keV monochromatic X-ray beam, an energy that is above the Cobalt absorption edge to avoid collecting fluorescence background signal of the Co^{2+} and Co^{3+} centres. The sample was mounted on a hexapod stage and oriented vertically with respect to the floor at an incidence angle of 0.33° (Figure 3.9). The signal was detected using a Pilatus 100k detector. Before starting the experiment, the sample orientation matrix must be defined. The procedure consists in identifying diffraction peaks for both the film and the substrate under the $\theta - 2\theta$ geometry, assigning tentative h, k, l indexes based on a preliminary assumption of the sample orientation and on the knowledge of the sample lattice parameters. The measured Bragg peaks are used to fit the orientation matrix, the goodness of which is evaluated afterwards based on the error of the fitting results. Once the orientation matrix is defined, the Bragg peaks to be detected in grazing incidence geometry are chosen specifying their h, k, l indexes. For each peak, azimuthal scans (in-plane rotations of the sample) were performed to optimize the signal intensity. In the experiment, we precisely determined the detector position for several diffraction peaks expected to be sensitive to the activation of the T_{2g} Raman active mode at 196 cm^{-1}. Based on DFT calculations [120], this phonon mode was ascribed to a specific lattice distortion mainly involving the displacement of the Co^{2+} tetragonal sites along the [111] direction. This motion is schematically shown in Figure 3.10 for the rhombohedral Co_3O_4 primitive cell, where the arrow represents the atomic displacement of the Co^{2+} site, and where we sketch in red the [111] plane corresponding
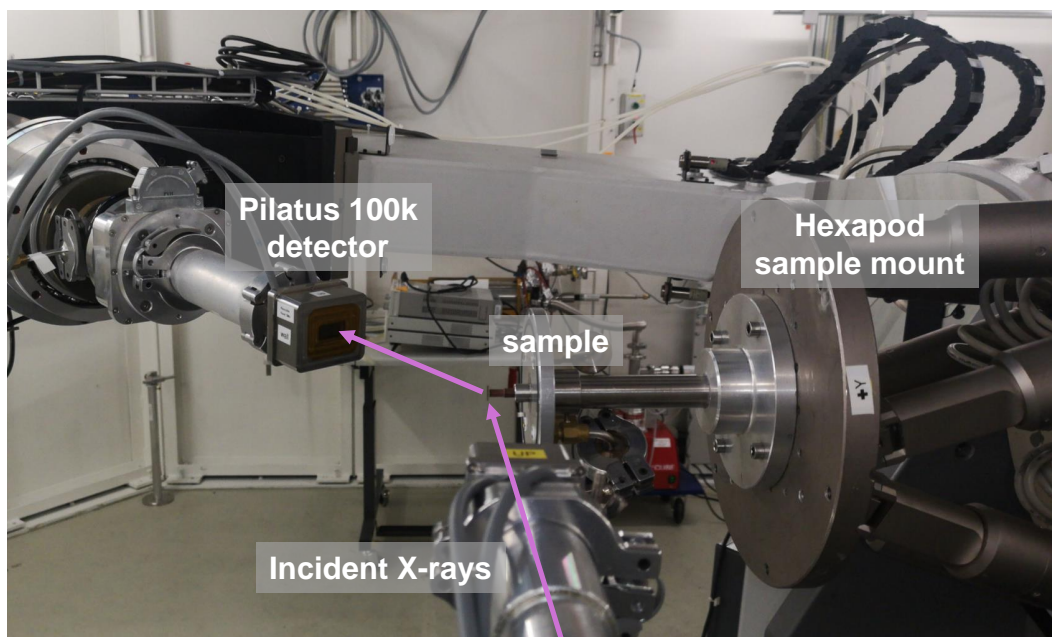
Figure 3.9: Experimental layout of the Material Science beamline. The sample is vertically oriented in grazing incidence geometry with respect to the incoming X-rays. The Pilatus 100k detector is in the geometry corresponding to the (311) Bragg peak detection.
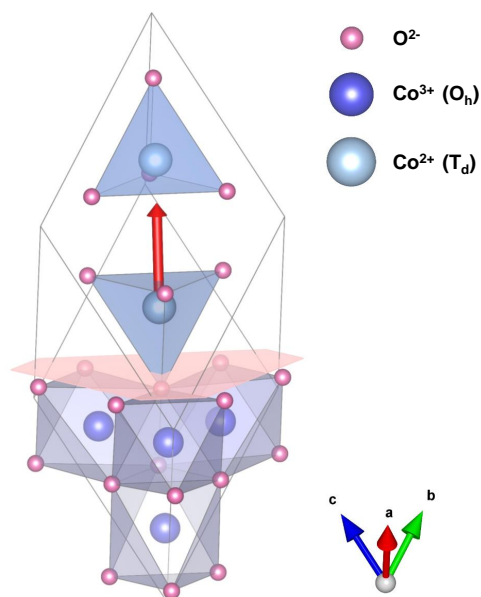
Figure 3.10: Schematic layout of the Co^{2+} tetrahedral atomic displacement activated by the T$_{2g}$ phonon mode. The red arrow points along the direction orthogonal to the [111] plane, reported in light-red, and corresponding to the out-of-plane orientation of our Co$_3$O$_4$ films. The smaller nuclear displacements of the other centres were omitted for clarity.

to the sample surface of our film. The preliminary estimation of the Bragg peaks which are mostly affected by the 196 cm^{-1} lattice distortion was performed computing the XRD signal intensities in VESTA [1] for two cases: the Co_3O_4 lattice crystal in its equilibrium position and the same lattice where a model distortion of the Co^{2+} site along the [111] direction was introduced. We selected the brightest peaks for which the intensity is strongly modified by this specific nuclear motion. In particular, we focused on the three-fold degenerate (311) peak, which was later experimentally measured at the EXFEL (see section 3.3.2), confirming the correctness of our experimental procedure.

3.2.4 X-ray emission spectroscopy

3.2.4.1 General principles

X-ray emission spectroscopy (XES) is an element-selective technique that is sensitive to the electronic, spin and local structural configuration of the probed site. There are multiple implementations of this method, but in the following we will focus on the non-resonant XES at the so-called K emission lines. This technique relies on a 1s electronic excitation into the continuum upon absorption of an X-ray photon, creating a short-living core hole which is filled with an outer shell electron. The resulting excess energy is released *via* competing Auger or fluorescence decay processes. In the former, a second electron is photoemitted from an outer shell, in the latter an X-ray photon is emitted at lower energies with respect to the initial X-ray excitation. A schematic illustration of the process is shown in Figure 3.11 (left). The energy of the fluorescence lines depends on the electronic transitions from the outer orbitals to the 1s core hole. As such, XES probes the occupied density of states of the material. The strongest emission process is related to the 2p to 1s transitions and give rise to the K_α lines, respectively $K_{\alpha 1}$ or $K_{\alpha 2}$ if the electron comes from $2p_{3/2}$ or $2p_{1/2}$ orbitals. About 6 to 8 times weaker are the 3p to 1s transitions of the so-called $K_{\beta 1,3}$ lines, as shown in Figure 3.11 (right) for the Cobalt K_α and K_β emission spectra of spinel Co_3O_4. Even though these processes involve electronic transitions between inner orbitals, both K_α and K_β spectra are indirectly sensitive to the valence electrons of the probed site, which in the case of transition metal atoms correspond to 3d orbitals. The information about the valence electronic configuration of the centre is obtained analysing the interaction between the 3d occupied orbitals and the 2p or 3p hole left in the system upon fluorescence decay. Since this interaction scales with the overlap between the inner orbitals and the 3d wave functions, it is stronger for the 3p orbitals [140]. As a consequence, the weaker K_β lines are more sensitive markers of the electronic configuration of the system compared to the K_α lines. Specifically, a linear relationship between the effective number of unpaired 3d electrons and the position of the K_β maximum was reported [141], provided that the oxidation state and the local environment of the metal site remain constant. The low energy side of the $K_{\beta 1,3}$ lines is characterized by an additional peak, called $K_{\beta'}$, which is related to the 3p-3d exchange interaction. Upon spin decrease, $K_{\beta 1,3}$ and $K_{\beta'}$ energies move towards each other, completely merging for spin configurations equal to zero. A different linear relationship is found between the spin states and K_α lines. In this case, the FWHM of the
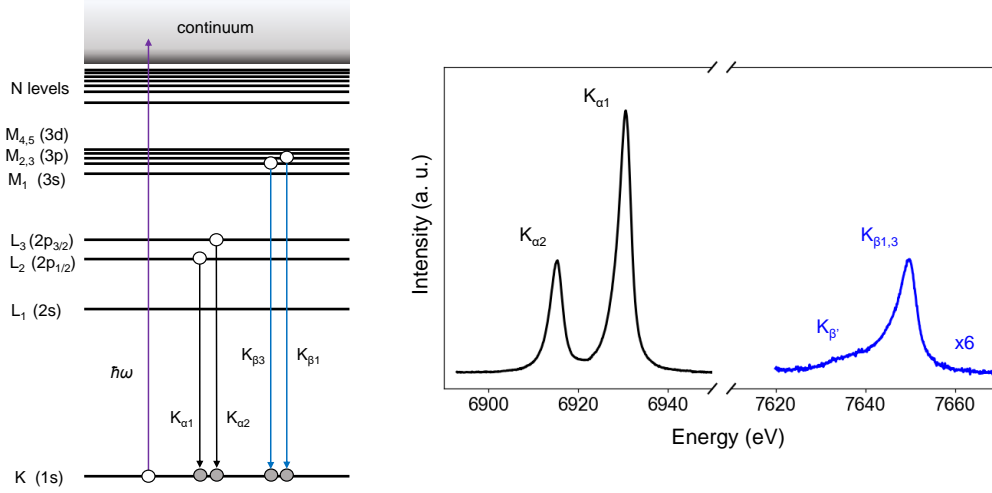
Figure 3.11: (left) Energy level diagram showing the electronic transitions involved in the generation of the $K_{\alpha 1}$, $K_{\alpha 2}$, $K_{\beta 1,3}$ and $K_{\beta'}$ emission lines upon non-resonant absorption of a X-ray photon from the 1s orbital. (right) Co_3O_4 emission lines at the Cobalt K_α and K_β energies.

emission lines scales linearly with the effective spin configuration, due to the 2p-3d exchange interaction [141].

In its time-resolved implementation, TR-XES can accurately probe photoinduced spin and electronic changes around the selected elements as a function of time [142–145]. In the following sections, we briefly present the implementation of TR-XES set-ups at both synchrotron and FEL facilities and we show preliminary results obtained in our experimental campaigns, in which TR-XES was used to follow spin changes in Co_3O_4 thin films.

3.2.4.2 Synchrotron set-up

XES and TR-XES measurements on Co_3O_4 thin films were conducted at the SuperXAS beamline of the SLS in order to determine the signal intensity of Cobalt K_α and K_β lines under the experimental conditions required for pump-probe measurements, namely grazing incidence geometry. A picture of the experimental layout is reported in Figure 3.12. At the SLS synchrotron, the X-rays are delivered at a repetition rate of 1.04 MHz with a hybrid electron filling pattern. In this operation mode, out of the 480 possible electron buckets of the storage ring, 390 are consecutively filled with electron bunches separated by 2 ns and compose the so-called multibunch. One of the remaining 90 empty buckets is filled with a single electron bunch, called camshaft, which has 4 times higher current than the individual bunches of the multibunch. The multibunch is used for steady-state measurement, whereas the camshaft is exploited in picosecond time-resolved experiments, thanks to its pulse duration of about 85 ps in Full Width Half Maximum (FWHM) [146]. XES data was collected with a Pilatus 100k detector, upon installation of a Von Hamos spectrometer in vertical geometry. Si(440) and Si(640) crystals were employed to disperse Co K_α (6.930 keV) and $K_{\beta 1,3}$ (7.650 keV) signals,
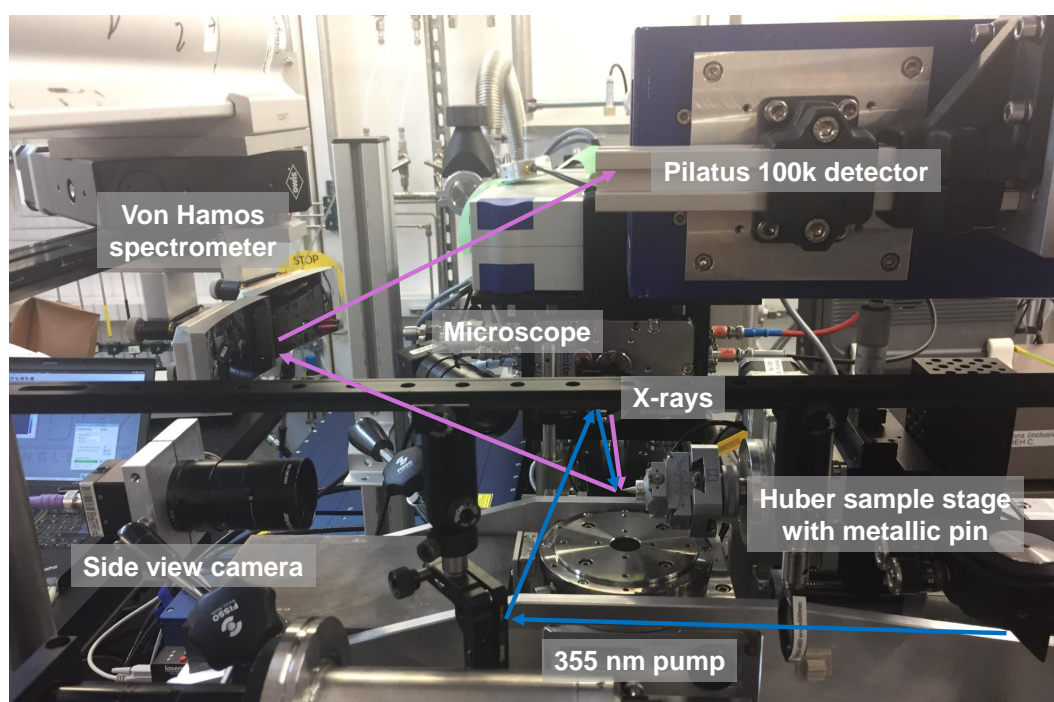
Figure 3.12: Experimental layout of the TR-XES setup of the SuperXAS beamline. The metallic tip (or the sample) is placed in grazing incidence geometry in the centre of rotation of the sample manipulator stage, imaged with a side view camera and a microscope, respectively at angles of 90 and ~30° with respect to the X-rays. The sample is pumped using a 355 nm excitation wavelength at an incidence angle of 3.3°-4°. The X-ray signal is dispersed by a Von Hamos spectrometer equipped with a pair of Si(440) and Si(640) crystals and is collected using a Pilatus 100k detector in vertical geometry.

respectively. Steady-state measurements were performed using a Si(111) crystal monochromator and selecting an off-resonance energy corresponding to 9.0 keV. The signal was collected exploiting the entire filling pattern of the synchrotron at 1.04 MHz.

For pump-probe measurements, only the emission signal generated by the camshaft was recorded with an electronic triggering of the Pilatus acquisition window. A pink beam centred at 9.0 keV was used in order to compensate the 100 times lower intensity of the camshaft signal with respect to the multibunch. The probe repetition rate was set to 260 kHz, twice the repetition rate of the Duetto pump laser. For the latter, a low repetition rate mode of 130 kHz was chosen in order to enhance the energy per pulse of the pump. We excited the sample at 355 nm, frequency tripling the fundamental photon energy of the laser (1064 nm). In the employed grazing incidence geometry, the X-rays and laser incidence angles were respectively varied between 0.3° and 1°, and between 3.3° and 4°. Under these conditions, the maximum pump fluence that we could achieved was 0.6 mJ/cm^2. In order to precisely determine the grazing incidence angle of the sample, a Huber mount was installed on top of the sample manipulator stage of the beamline, and a pair of microscope and side view camera was employed to determine the centre of rotation of the stage using a metallic pin.

In the measurements, strong XES emission spectra were obtained from the thin films. The energy calibration of the Cobalt emission lines was performed collecting the elastic scattering
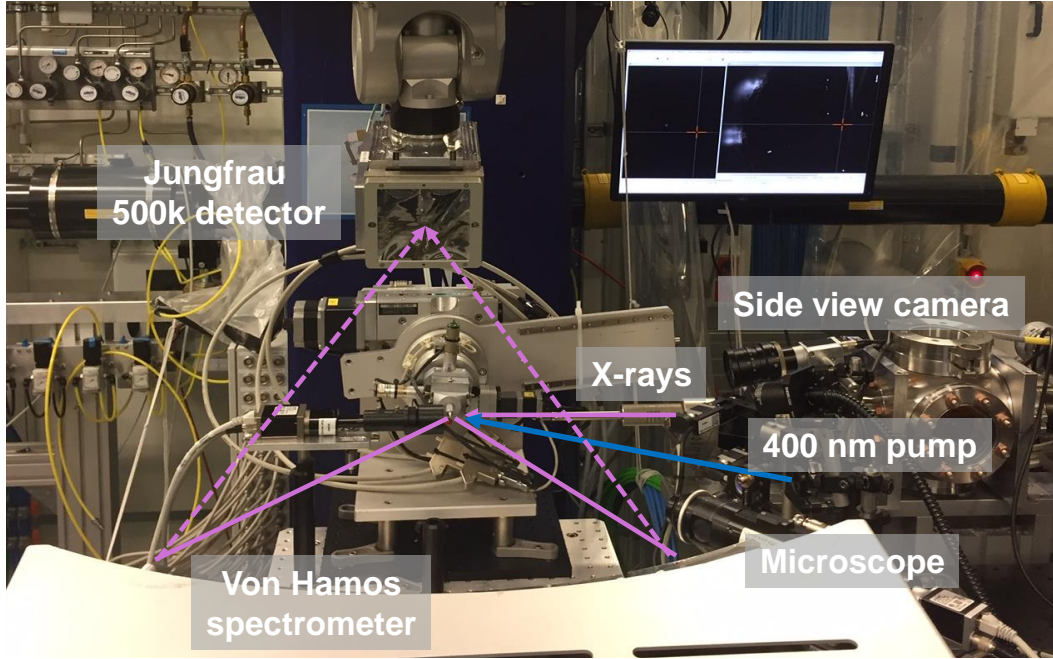
Figure 3.13: Experimental layout of the FEX instrument at EXFEL. The sample (or a metallic tip) is in grazing incidence geometry, with an angle of 0.33° with respect to the incoming X-rays. The 400 nm pump hits the sample with a small angle (8.33°). A microscope and a side view camera were used to determine the centre of rotation of the sample manipulator, in order to accurately control the pump and probe incidence angles. A Von Hamos spectrometer is placed at 90° with respect to the X-rays and is equipped with 8 Si(531) and 4 Ge(111) crystals. A Jungfrau 500k detector was moved with a motorized robot arm to collect either the Cobalt K$_\alpha$ or K$_\beta$ lines in vertical geometry.

signal from the sample in grazing incidence configuration at different monochromatic X-ray energies. We characterized the fingerprint of X-ray sample damaging as a redshift of both K$_\alpha$ and K$_\beta$ lines up to 2 eV. Sample degradation was observed for grazing incidence angles larger than 1°, possibly caused by a combination of increased thermal load, lower X-ray reflectivity of the sample, and higher X-ray photon fluence due to the probe footprint reduction upon incidence angle increase. Thus, for both steady-state and pump-probe measurements, incidence angles below 1° were used.

3.2.4.3 Free electron laser set-up

TR-XES measurements were performed on Co$_3$O$_4$ thin films at the Femtosecond X-ray Experiments (FXE) scientific instrument of the EXFEL [147]. The experimental layout of the experiment is reported in Figure 3.13. The sample was mounted on a Huber stage on top of a motorized sample manipulator in grazing incidence geometry (0.33° with respect to the incoming X-rays). A side view camera and a microscope were employed to determine the centre of rotation of the stage using a metallic pin. A pink beam centred at a 9.3 keV X-ray photon energy was used for off-resonance XES and XRD measurements, with a maximum average energy of 2.5 mJ and an X-ray spot size in normal incidence of 110x110 μm^2 FHWM.

The XES signal was collected using a high-energy resolution Von Hamos spectrometer equipped with 8 Si(531) and 4 Ge(111) crystals to disperse respectively Cobalt K_{α} and K_{β} lines. Each emission line was separately detected using a single module Jungfrau 500k detector with an active area of about 38x76 cm^2 [148], mounted on a vibrationally stabilized inverted robot arm. The same detector was used to identify and collect steady-state XRD signals from the (311) Bragg peak of the Co$_3$O$_4$ film. A Helium bag was installed to reduce the air scattering of the dispersed X-ray signals. During our measurements, the probe energy was attenuated to an average value of 500 μJ in order to avoid nonlinearities in the detected signals. The FEL repetition rate was also decreased down to 10 Hz to prevent sample damaging. Under these operation conditions, the Jungfrau detector was operated in shot-to-shot detection mode. Pump-probe measurements were performed exciting the sample at 5 Hz repetition rate with 400 nm light, frequency doubling the output of a specially designed burst-mode femtosecond laser system available at the beamline [149]. This system operates at variable repetition rate generating broadband 800 nm pulses amplified in a multi-stage non-collinear optical parametric amplifier (NOPA) and routinely compressed to 15 fs pulse durations. The timing jitter between the laser pump and the FEL probe, which is generated *via* a self-amplified spontaneous emission (SASE) process [150], makes the effective time resolution of pump-probe experiments at the FXE beamline of about 115 fs FWHM [151]. In grazing incidence geometry, a 4.4 mJ/cm^2 pump fluence was used to photoexcite the sample. Before starting the pump-probe measurements, we carefully determined the experimental conditions that prevented sample damaging. Based on the results of our previous TR-XES investigation at the synchrotron, very shallow incidence angles were used. The 10 Hz repetition rate was beneficial in reducing the thermal load on the sample, representing the most important source of degradation. Indeed, despite the much higher peak power of the FEL pulses with respect to the synchrotron bunches, under the employed conditions no signatures of sample damaging were observed.

3.3 Results

3.3.1 Femtosecond broadband reflectivity measurements

Femtosecond broadband investigations in the visible regime on Co$_3$O$_4$ films were performed in reflectivity mode, pumping the sample at 800 nm and 400 nm in order to elucidate the excitation wavelength effects on the charge carrier dynamics. The experiments were conducted in the fluence range between 1-10 mJ/cm^2 (800 nm pump) and 2-12.6 mJ/cm^2 (400 nm pump). The photocarriers' density was computed following the formula:

$$n_e = \frac{F}{h\nu \cdot d}(1-R) \tag{3.4}$$

where F is the pump fluence, h is the Planck constant, ν is the photon frequency, d is the penetration depth and R is the reflectivity at normal incidence. Densities in the range between 10^{20} cm^{-3} and 10^{21} cm^{-3} are obtained, in the linear regime for both pump wavelengths,
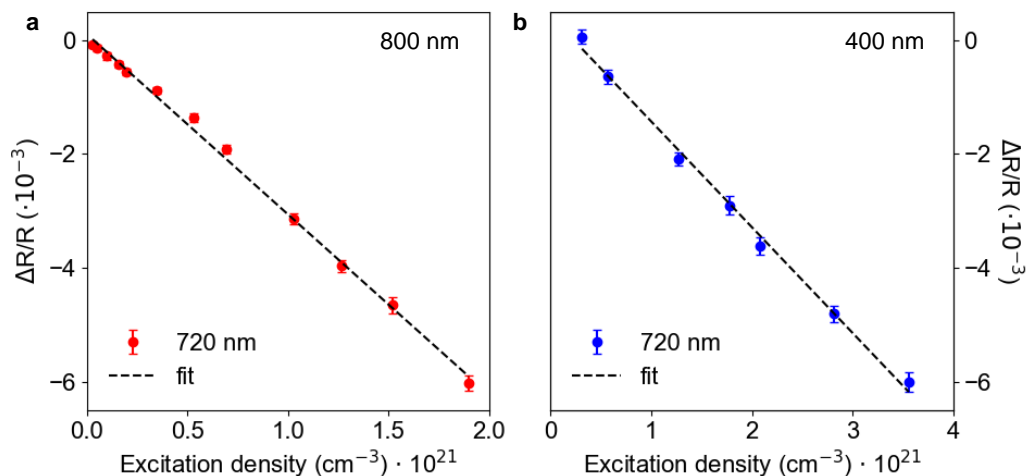
Figure 3.14: (a,b) 720 nm TRR intensity as a function of the excitation density, respectively for 800 nm and 400 nm pump wavelengths. The pump-probe intensities were collected at 1.7 ps time delay.

as reported in Figure 3.14 for the 720 nm probe wavelength. In the following, we compare TRR results obtained under similar excitation densities, namely $1.4 \cdot 10^{21}$ cm^{-3} (800 nm) and $1.3 \cdot 10^{21}$ cm^{-3} (400 nm), unless explicitly mentioned. As shown in Figure 3.15(a,b), the 2D maps obtained in the first 10 ps are qualitatively similar, with modest line shape changes, which are limited to the first 2 ps, and the retention of the transient intensity up to the longest time delay (9.4 ps). Figure 3.15(c,d) reports the energy cuts of the TRR maps at selected time delays for the 800 nm and 400 nm excitation wavelengths. In both cases, the spectra are characterized by two negative bands centred around 520 nm and 750 nm, close to the maxima of the optical absorption spectrum, and a positive feature at 630 nm, corresponding to the local minimum between the LMCT and MMCT absorption bands (see Figure 3.2). An apparent blue shift of the transient spectral weight occurs within the first ps. Despite the overall similarity between the two TRR maps, a closer inspection of the time traces reported in Figure 3.16(a,b) for the first 4.5 ps at the local extrema of 520 nm, 630 nm, 740 nm, and at 575 nm, highlights significant differences in the temporal response of the system when excited at 800 nm and 400 nm. Upon 800 nm pump, the negative bands peaked at 520 nm and 740 nm are characterized by a prompt rise, followed by a sub-ps decay and a second relaxation process on the ps time scale, reaching a plateau, which is kept up to the longest time delay. Instead, the response at 630 nm shows negative values only around time zero and follows a progressive increase of the transient positive signal during the first 2 ps. The intensity growth of the positive band occurs on the same time scales of the negative bands' relaxation. The presence of a second, slower time component is better observed for wavelengths close to the turning point separating the negative band at 520 nm and the positive feature at 630 nm, as shown for the trace at 575 nm. Exciting the sample at 400 nm, the temporal response of the TRR bands is also characterized by two time constants and an offset at longer times. However, differently from the 800 nm excitation, the time scales of two processes are much faster, being both on sub-ps time scales.
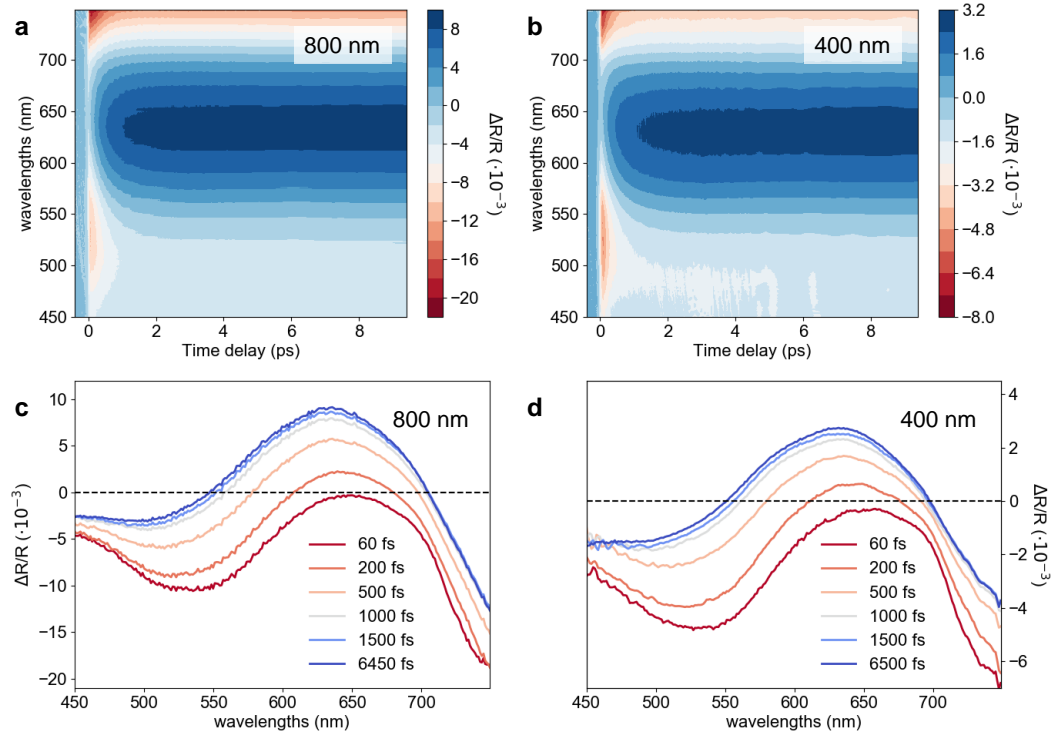
Figure 3.15: (a,b) TRR 2D maps for 800 nm and 400 nm pump wavelengths, respectively with excitation densities of $1.4 \cdot 10^{21}$ cm^{-3} and $1.3 \cdot 10^{21}$ cm^{-3}. (c,d) 800 nm and 400 nm pump TRR energy cuts at the time delays: 60 fs, 200 fs, 500 fs, 1000 fs, 1500 fs, 1500 fs, 6450 (6500) fs.

These differences are captured by the global fit of the TRR maps, which were analysed assuming a bi-exponential time evolution of the signal and an offset, convoluted with a Gaussian IRF function (σ=75 fs). As explained at the end of section 3.2.2.2, in the global fit analysis all probe wavelengths are simultaneously fitted using the same time constants and leaving the wavelength-dependent pre-exponential amplitudes as free parameters of the fit. As a result, for some traces (*e.g.* the negative band maxima) the first exponential decay is dominant, whereas for other wavelengths the second decay process becomes more relevant (*e.g.* at the turning points between the negative and positive bands). The reconstructed maps are reported in Figure 3.17(a,b). The comparison with the experimental maps in Figure 3.15(a,b) confirms the quality of the fit, whose results are summarized in in Table 3.1. We remark that in absence of a second exponential decay, or without an offset at long time delays, the fit significantly worsens. Two time constants of 430±10 fs and 2.5±100 ps are obtained exciting the sample with 800 nm light, whereas a much faster response is observed upon 400 nm excitation, characterized by values of 260±30 fs and 710±40 fs. In our investigation, we collected TRR maps as a function of the excitation fluence and did not observe changes in the obtained time constants. A second crucial difference between the two photoresponses is the presence of time modulations in the TRR signal as a consequence of coherent collective excitations launched in the system upon ultrafast excitation. In order to isolate the coherent modulations from the incoherent electronic relaxation process, we subtracted the global fit signal from the 2D reflectivity maps.

71
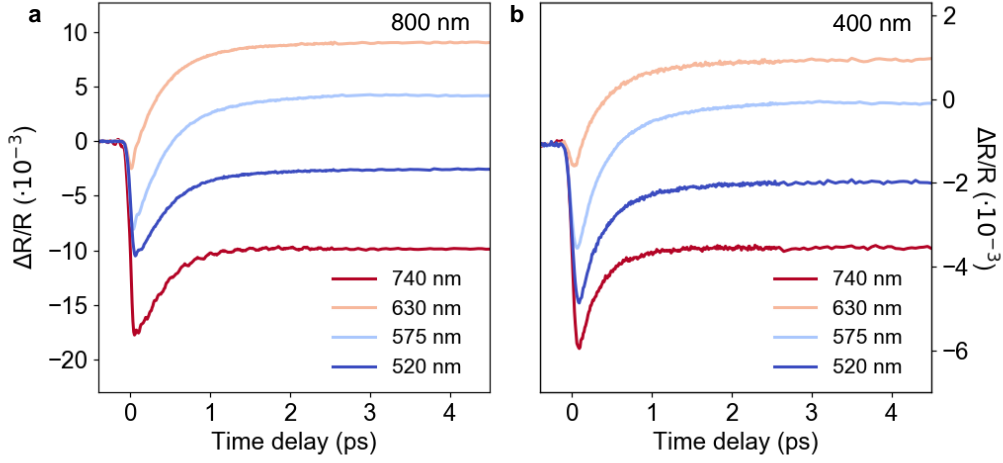
Figure 3.16: (a,b) 800 nm and 400 nm time traces, respectively at excitation densities of $1.4\cdot10^{21}$ cm^{-3} and $1.3\cdot10^{21}$ cm^{-3}. Four selected wavelengths are displayed: 740 nm, 630 nm, 520 nm, and 575 nm, respectively corresponding to the ΔR/R local extrema of the TRR maps and to the turning point between the negative feature at 520 nm and the positive feature at 630 nm.

The map of residuals for 800 nm and 400 nm excitations are reported in Figure 3.17(c,d) for the first 2.225 ps of the dynamics. Panel (c) shows distinct oscillations with a frequency of 170 fs across the entire map, which are more defined in the red region of the spectrum. In panel (d), instead, we notice smaller oscillations with a longer oscillation period. The strong residual signals around time zero are due to coherent artefacts, which were not completely described in the fit.

Pump wavelength	τ_1 (ps)	τ_2 (ps)	τ_3 (ps)
800 nm	0.43±0.01	2.5±0.1	offset
400 nm	0.26±0.03	0.71±0.04	offset

Table 3.1: Exponential decay time constants resulting from a global fit analysis of the TRR maps upon 800 nm and 400 nm excitation.

We improved the SNR of the residuals performing an average over several wavelengths. Specifically, we computed the mean value of the TRR residuals in the wavelengths range 500-570 nm and 660-730 nm, *i.e.* in the regions where the amplitude of the incoherent electronic response is smallest. The results are shown in Figure 3.18(a,b), where we notice strong differences between the different pump wavelengths.

Upon 800 nm excitation, a pronounced coherent response with a frequency of 170 fs is observed at 660-730 nm, with a moderate daof the fluence, evenmping across the investigated time window. At 500-570 nm, instead, the oscillation at 170 fs is less intense and the coherent response is dominated by a damped oscillation of period ~1.7 ps. The response induced by the 400 nm pump is completely different, with modulations comparable to the noise level for the 660-730 nm trace and a distinct oscillation with frequency 405 fs for the 500-570 nm trace.
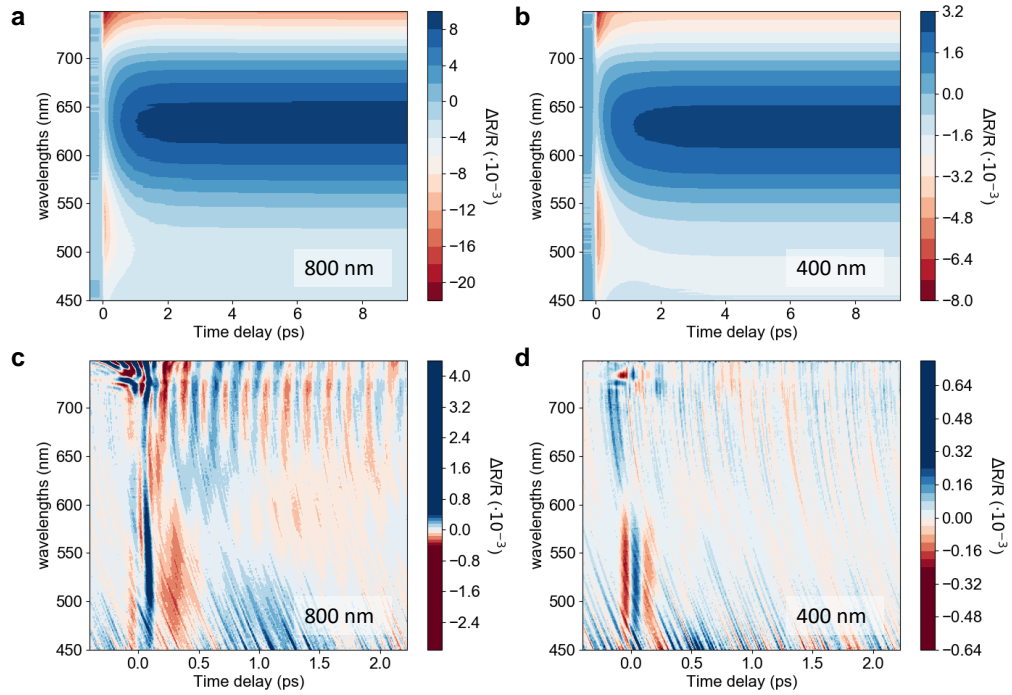
Figure 3.17: (a,b) Reconstructed 2D maps from global fit results of the 800 nm (excitation density of $1.4\cdot10^{21}$ cm^{-3}) and 400 nm (excitation density of $1.3\cdot10^{21}$ cm^{-3}) pump TRR maps, respectively; (c,d) 2D maps of residual obtained subtracting the reconstructed maps of the global fit from the experimental maps upon 800 nm (excitation density of $1.4\cdot10^{21}$ cm^{-3}) and 400 nm (excitation density of $1.3\cdot10^{21}$ cm^{-3}) excitation, respectively.

In Figure 3.18(c,d), we report the Fourier transform (FT) of the traces presented in panels (a,b). Following established procedures for time-domain Raman spectroscopy data treatment [31; 152], the analysis was performed using a zero padding algorithm and applying a Kaiser-Bessel windowing (β=6), in order to reduce the spectral leakage caused by the finite time sampling prior to FT [153]. In panel (c), a feature at 196 cm^{-1} is observed in both spectral ranges, with the 500-570 nm spectrum showing an additional intense peak at about 20 cm^{-1}. The feature at 196 cm^{-1} exactly matches the T$_{2g}$ Raman active phonon observed in Figure 3.5. Thus, we assign the fast coherent modulation of the TRR measurements upon 800 nm excitation to an ISRS process. The slower oscillation at 20 cm^{-1} is possibly related to a coherent acoustic phonon (CAP) that could be generated *via* different possible sources, such as deformation potential or thermoelasticity [154–156]. Panel (d) shows a noisy FT spectrum for the 660-730 nm trace, which would require better statistics to confirm the possible presence of two faint features at 108 cm^{-1} and 435 cm^{-1}. Instead, the FT of the 500-570 nm trace displays a prominent peak centred at 82 cm^{-1}, together with a small feature around 20 cm^{-1}. The 82 cm^{-1} feature does not correspond to any Raman active mode reported in Figure 3.5, independently of the excitation wavelength (532 nm and 785 nm). Therefore, this peak can be ascribed to a DECP coherently generated in the material upon the selective excitation of the system at 400
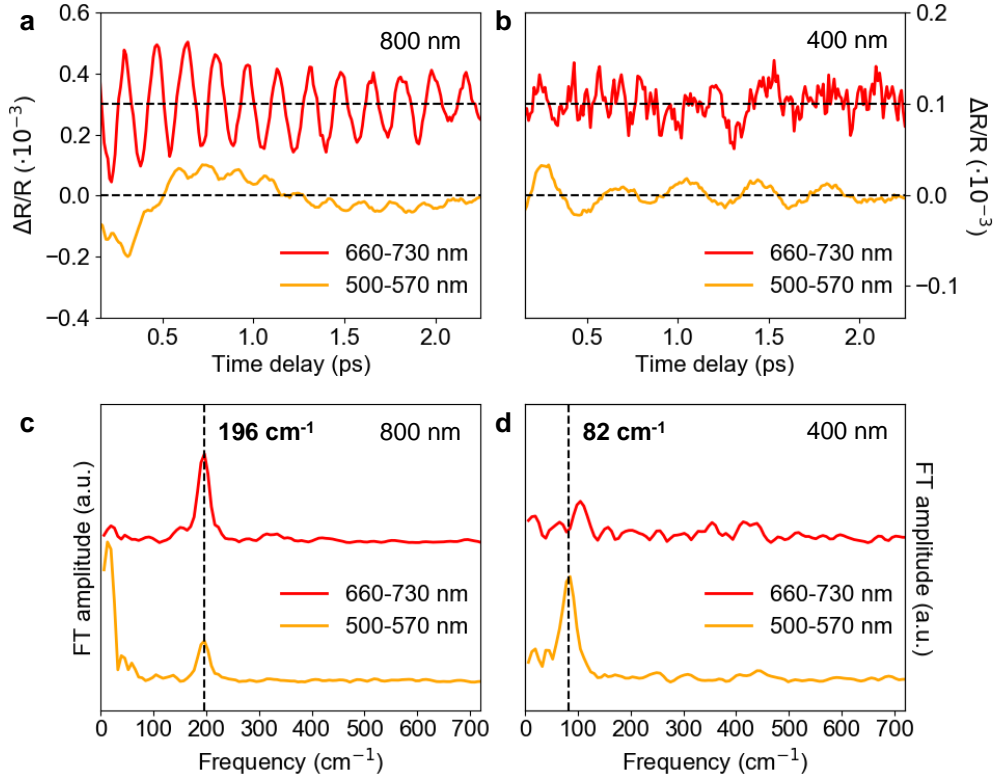
Figure 3.18: (a) Average of residuals in the 500-570 nm and 660-730 nm probe windows upon 800 nm pump excitation (photocarriers density of 1.4·10^{21} cm^{-3}). An offset of +0.3 mO.D. was applied to the 660-730 nm trace for clarity. (b) Average of residuals in the 500-570 nm and 660-730 nm probe windows upon 400 nm pump excitation (photocarriers density of 1.3·10^{21} cm^{-3}). An offset of +0.1 mO.D. was applied to the 660-730 nm trace for clarity. (c,d) Fourier transforms of the traces reported in panels (a,b) respectively. The vertical dashed lines highlight the strongest FT features, respectively at 196 cm^{-1} and 82 cm^{-1} for the excitation wavelengths 800 nm and 400 nm.

nm. In order to better characterize the nature of these collective excitations, we performed fluence dependence studies of the TRR maps for both excitation wavelengths. Figure 3.19(a,b) reports the FT amplitudes of averaged time traces as a function of the excitation density: we selected the 660-730 nm and 500-570 nm traces respectively for the 800 nm and 400 nm pumps, with the aim of characterizing the faster oscillatory components of our spectra. For completeness, in panels (c,d) we also show the amplitude changes of the 20 cm^{-1} feature as a function of the fluence, even though a detailed analysis of CAPs is beyond the scope of this work. In all panels, the experimental data are plotted with the corresponding linear fits, which well describe the fluence dependence of the 196 cm^{-1} and 82 cm^{-1} features. This is consistent with both proposals of ISRS generation of the T$_{2g}$ mode at 196 cm^{-1} and the DECP origin of the phonon mode at 82 cm^{-1} [125], as described in section 3.2.2.1. No frequency shifts of the FT amplitudes of the optical phonon maxima are observed by changing the pump fluence.
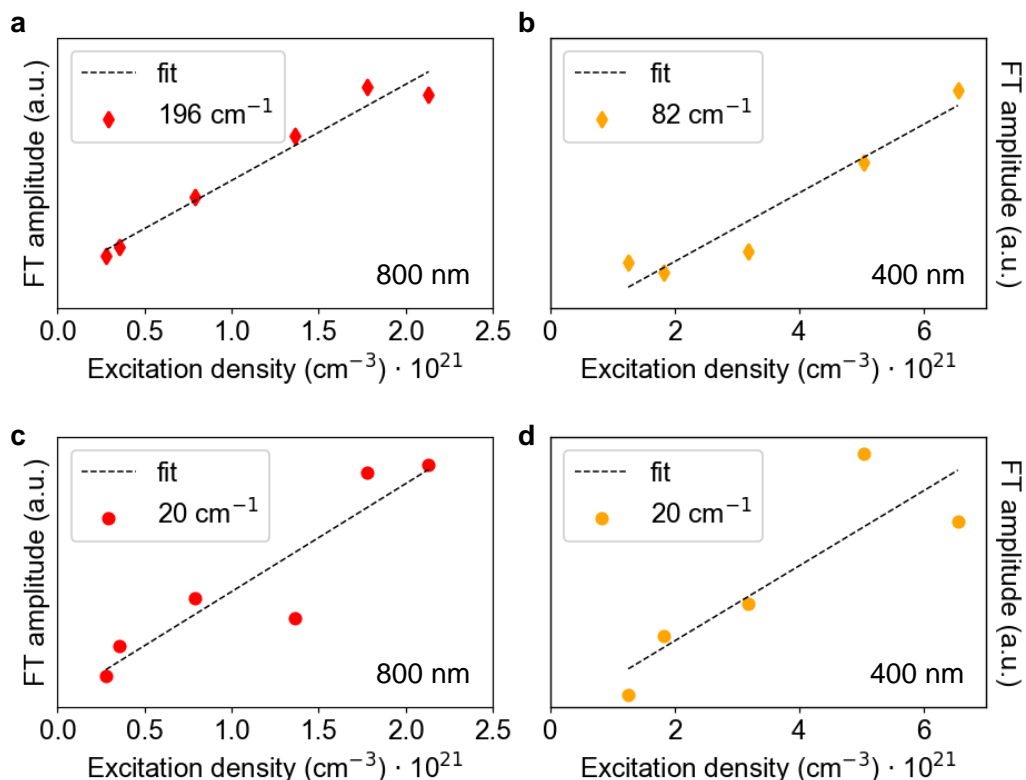
Figure 3.19: (a,b) Fourier transform amplitudes of average residuals as a function of the excitation density, respectively for the 196 cm^{-1} feature (800 nm pump, 660-730 nm probe range) and 82 cm^{-1} feature (400 nm pump, 500-570 nm probe range). (c,d) Fourier transform amplitudes of average residuals as a function of the excitation density for the 20 cm^{-1} feature, respectively for 800 nm pump (660-730 nm probe range) and 400 nm pump (500-570 nm probe range).

3.3.1.1 Discussion

The 400 nm excitation was unambiguously assigned to an O^{2-} (2p) to Co^{3+} (e$_g$) charge-transfer transition, based on a XUV transient absorption investigation at the Co M$_{2,3}$ edge of Co$_3$O$_4$ thin films [114]. In that work, two relaxation time constants were measured, 190±10 fs and 535±33 fs, possibly ascribed to an Auger recombination process and hot carrier relaxation towards the band edges. Accounting for the differences in the pump excitation densities between our measurements and the XUV ones, a general agreement in the time constants is observed: in fact, the authors reported a first time constant of 270±70 fs for photocarrier densities of ~2·10^{21} cm^{-3}. Thus, we assign the first time constant to a convolution of Auger recombination process, marginal at our fluences, and ultrafast charge carrier thermalization, and the second process at 710±40 fs to photocarrier cooling. We claim the same processes are involved upon 800 nm excitation, despite the longer relaxation times, respectively 430±10 fs and 2.5±0.1 ps. Indeed, a time constant of about 2 ps was ascribed to hot carrier cooling in a combined picosecond transient absorption and transient reflectivity investigation in the visible domain on Co$_3$O$_4$ thin films with 800 nm pump light [4]. Based on the similarity

between transient absorption and transient reflectivity spectra, the three spectral features composing the transient energy traces (which agree with those shown in Figure 3.15(c,d)) were interpreted in terms of ground state bleach (GSB) of the LMCT and MMCT bands and photoinduced absorption (PA) [4]. The authors observed the same transient line shapes upon 520 nm, 800 nm, and 1400 nm excitation wavelengths. Additionally, they reported a bleaching of the d-d transition bands in the NIR, which increase in intensity on the ps time scale and decay in hundreds of ns. Based on these results, localized d-d excitations were proposed as the final state of the photodynamics, independent of the optical transition originally excited. The absence of line shape changes in the transients was interpreted in terms of a modulation of the hybridization between O 2p and Co d orbitals, due to electron-phonon coupling effects. This explanation would account for the bleaching of the CT electronic transitions even in absence of state filling effects, since after the first few ps the photocarriers have relaxed in the d-d states.

Despite this consistent picture, our ultrafast measurements with fs resolution unveil a more complex scenario upon different excitation wavelengths. Indeed, there is an apparent contradiction between the absence of specificity in the final states populated in a few ps (notwithstanding the employed pump frequency), and the highly selective phonon and temporal response observed in our high-resolution experiments.

Our results show that the excitation of the LMCT state leads to an ultrafast relaxation that is faster than the dynamics of the MMCT. This is in contrast with the idea that longer relaxation times are expected with increasing the photon energy with respect to the Mott-Hubbard band gap, since more electronic excess energy should be dissipated. Thus, we conclude that the decay process leading the LMCT and MMCT states to the d-d states occurs through different relaxation channels, ruling out the hypothesis of a cascade process that brings the LMCT through the MMCT to the d-d states.

The presence of a DECP upon 400 nm excitation implies that electron-phonon coupling occurs between the photocarriers and the optical phonon at 82 cm^{-1}. Our measurements show that the collective excitation of this phonon mode is preserved during the electronic relaxation process from the originally populated LMCT state to the local d-d states, since the phonon oscillation lives more than 2 ps, whereas charge carrier cooling occurs on sub-ps time scales. Thus, we assume that a strong electron-phonon coupling is present also in the final state.

These contrasting evidences can be rationalized in terms of ultrafast intersystem crossing (ISC). As proposed by Jiang *et al.* [114], the sub-ps dynamics observed upon 400 nm excitation could be related to a selective relaxation process which leads the LMCT population directly to the lower d-d states. This nonadiabatic relaxation, which has been observed in the photodynamics of transition metal complexes in solution [157–160], is quite uncommon in solid-state systems, whose photodynamics is mostly ruled by the intra- and inter-valley scattering processes of itinerant electrons. Given the generally localized nature of the electronic states in transition metal oxide systems [161], an atomic-like perspective similar to the transition metal complexes in solutions could be proposed for Co$_3$O$_4$. Under this assumption, the LMCT excitation impulsively shifts the equilibrium position of the potential energy surface along the nuclear coordinate described by the 82 cm^{-1} phonon mode, launching a coherent phonon oscillation
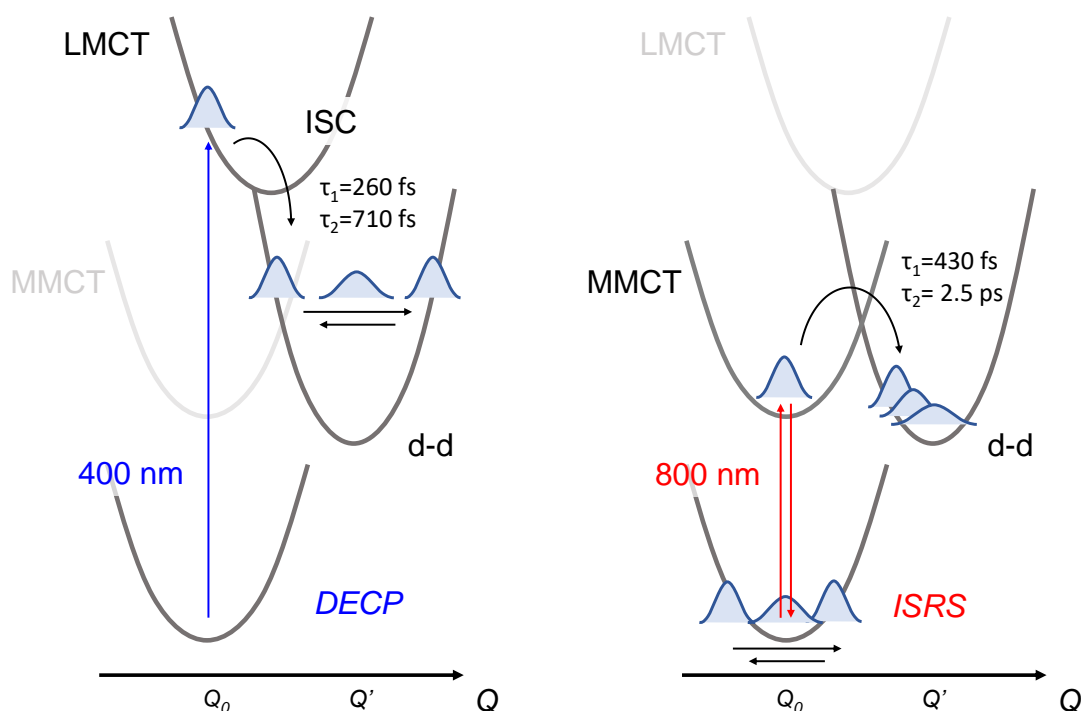
Figure 3.20: Schematic representation of the Co_3O_4 photodynamics upon 400 nm (left) and 800 nm (right) excitation. The blue Gaussian-like curves describe the collective nuclear coordinate *Q(t)* coherently moving on the potential energy surface of the system. The 400 nm pump promotes a LMCT excitation, upon which the system possibly decays into the localised d-d states *via* ultrafast ISC. This direct relaxation process preserves the coherence of the phonon oscillations, leading to a periodic modulation of the reflectivity due to the collective nuclear displacement associated with the DECP at 82 cm^{-1}. Instead, the 800 nm pump excites a MMCT transition, which decays into the d-d state more slowly. This electronic relaxation causes the loss of the vibrational coherence created upon impulsive photoexcitation, even though it brings the system into the same d-d states populated by the LMCT relaxation. The nuclear distortions caused by the electron-phonon coupling in the d-d states is preserved but cannot be observed in reflectivity in absence of coherent vibrational dynamics. Instead, a periodic modulation of the transient signal is found due to the activation of the T_{2g} phonon mode at 196 cm^{-1} *via* the ISRS process.

in the system at the Brillouin zone centre, as sketched in Figure 3.20(left). As a result, a periodic modulation of the dielectric function is generated, enabling the measurement of a coherent nuclear response in transient reflectivity. On ultrafast time scales, the photocarriers relax *via* intra- and inter-band scattering and localise on the Cobalt centres, which change their spins. At the atomic-level, this process corresponds to an ultrafast ISC. Since the fingerprint of the electron-phonon interaction, *i.e.* the coherent modulation of the TRR signal, is preserved even when charge carrier thermalization has completed, the coupling between the electronic and nuclear degrees of freedom must also occur in the d-d states. Therefore, it should be present in the d-d states that are eventually populated upon 800 nm light activation. However, in the latter case, the slower incoherent electronic relaxation may cause the loss of coherence in the phonon oscillations, preventing the observation of the DECP *via* the modulation of the transient reflectivity signal even in presence of electron-phonon coupling (Figure 3.20(right)).

The proposed scenario calls for a more detailed investigation using time-resolved methods that are sensitive to incoherent changes of the nuclear and spin degrees of freedom, motivating the experimental campaign under preparation at the EXFEL. There, we will investigate the system's photodynamics through simultaneous detection of TR-XRD and TR-XES upon 400 nm and 800 nm excitation, confirming or invalidating the presence of an ISC mechanism driving the wavelength selective ultrafast photodynamics of Co$_3$O$_4$.

3.3.2 Ultrafast X-ray emission spectroscopy measurements

In this section we present preliminary TR-XES results obtained both at synchrotron and FEL facilities, offering a first comparison to complement the results of our ultrafast optical investigation. In Figure 3.21(a,b), we report the steady-state XES spectra collected at the EXFEL at the Cobalt K$_\alpha$ and K$_\beta$ lines for Co$_3$O$_4$ thin films and for two references. These compounds contain Co^{2+} and Co^{3+} octahedral centres, respectively Cobalt(II) tris(bipyridine) (Co(bpy)$_3$$^{2+}$) and Cobalt(III) tris(bipyridine) (Co(bpy)$_3$$^{3+}$) chloride pellets. The direct inspection of the spectra shows that Co$_3$O$_4$ has emission lines that are peaked at intermediate positions with respect to the two references. Specifically, in panel 3.21(a) we observe that, upon reduction of the Co centre in Co(bpy)$_3$, the K$_{\alpha 2}$ line blueshifts from 6930.6 eV to 6931 eV. A similar trend is shown in panel 3.21(b), in which, going from Co^{3+} to Co^{2+}, the K$_{\beta 1,3}$ line blueshifts from 7649.7 to 7650.6 eV and the K$_\beta$' sideband distinctly increases in intensity. These spectral changes result from an interplay between the oxidation and spin differences of the two compounds. Indeed, as explained in 3.2.4.1, XES is a sensitive marker of the spin state of the probed sites through K$_{\alpha 1}$ FWHM and K$_\beta$ intensity and position [141], provided that the other parameters are kept constant. A more quantitative analysis would require measuring a third reference compound in which only one of the two parameters is changed, *e.g.* a reference with only one Cobalt(II) centre with tetrahedral symmetry. We remark here that part of the beamtime at the EXFEL was dedicated to the characterization of the XRD (311) peak previously identified in the synchrotron measurements at the Material Science beamline of SLS. The 2D map collected by the Jungfrau 500k detector is reported in Figure 3.22. In Figure 3.23, we report the steady-state K$_\alpha$ spectrum of the Co$_3$O$_4$ sample, along with the TR-XES energy traces collected at two different time delays, 1 ps and 4 ps, and the difference between the Co(bpy)$_3$$^{2+}$ and Co(bpy)$_3$$^{3+}$ steady-state K$_\alpha$ spectra, labelled as Co^{2+}-Co^{3+}. The TR-XES spectra were multiplied by a factor x3 and the Co^{2+}-Co^{3+} trace by a factor x1.3. The transient traces were obtained in about 30 minutes of acquisition time each and were collected just before a major failure of the pump laser of the beamline. As a consequence, no further pump-probe data could be collected during the beamtime.

Significant differences are observed in the spectral line shapes of the two transients. At 1 ps time delay, the K$_{\alpha 1}$ pump-probe is characterized by a derivative-like shape with a node at 6930.6 eV, which is possibly due to a slight shift of the main peak towards higher energies. Instead, the K$_{\alpha 2}$ transient resembles a shrinkage of the steady-state peak, with an increased intensity of the maximum, resulting in a positive pump-probe signal at 6915.6 eV and two negative sidebands. At later times (4 ps), both lines are modified, with a derivative-like
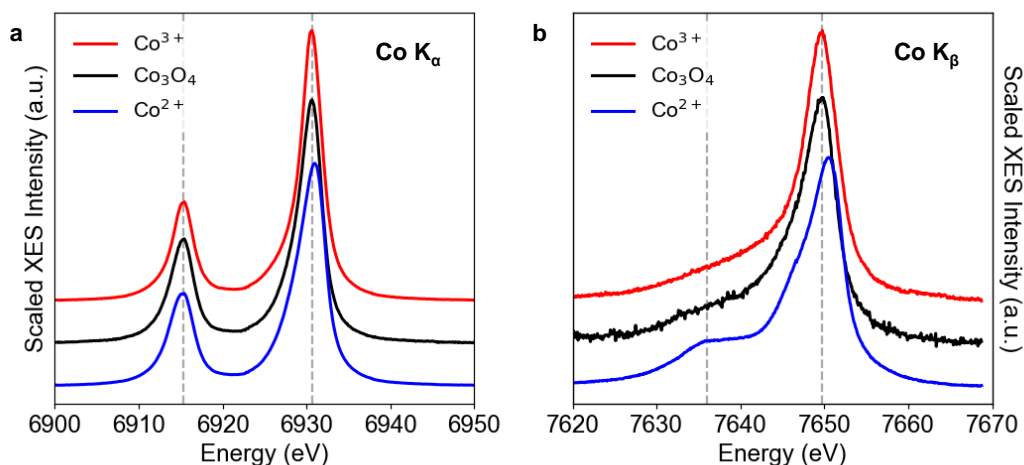
Figure 3.21: (a) Co $K_{\alpha 1}$ and $K_{\alpha 2}$ emission lines of Co_3O_4 and two standards containing Co^{2+} and Co^{3+} centres with octahedral symmetries, respectively $Co(bpy)_3^{2+}$ and $Co(bpy)_3^{3+}$. (b) Co $K_{\beta'}$ and $K_{\beta 1,3}$ emission lines of Co_3O_4 and of the two standards $Co(bpy)_3^{2+}$ and $Co(bpy)_3^{3+}$. The dashed vertical lines at energies 6915.3 eV, 6930.65 eV, 7636 eV and 7649.7 eV respectively highlight the positions of the features $K_{\alpha 1}$, $K_{\alpha 2}$, $K_{\beta'}$, $K_{\beta 1,3}$ of the Co_3O_4 sample.
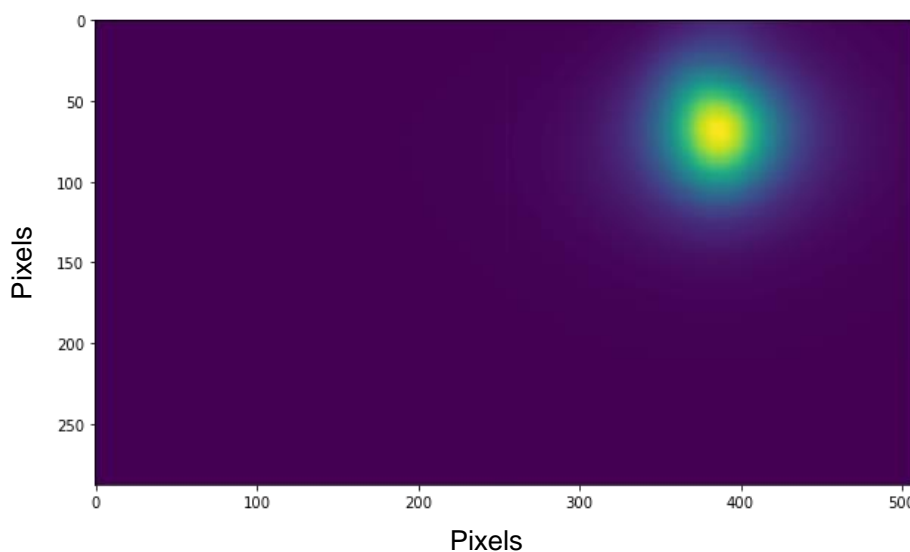
Figure 3.22: Co_3O_4 (311) Bragg peak detected in grazing incidence geometry; x- and y-axis correspond to Jungfrau 500k pixels, z-axis corresponds to the intensity of the X-ray signal.

transient shape with opposite sign with respect to the 1 ps trace at $K_{\alpha 1}$ energies, and slight changes on the low-energy side of the $K_{\alpha 2}$ line. The Co^{2+}-Co^{3+} spectrum shows a negative peak and two positive sidebands around the $K_{\alpha 1}$ maximum, whereas an intensity increase (decrease) of the red (blue) side of the $K_{\alpha 2}$ line is observed around the node at 6914.7 eV. Another trace at 2 ns was measured at the SuperXAS beamline at the SLS, with parallel detection of K_{α} and K_{β} lines. The experimental conditions were slightly different, exciting the sample (a 51 nm
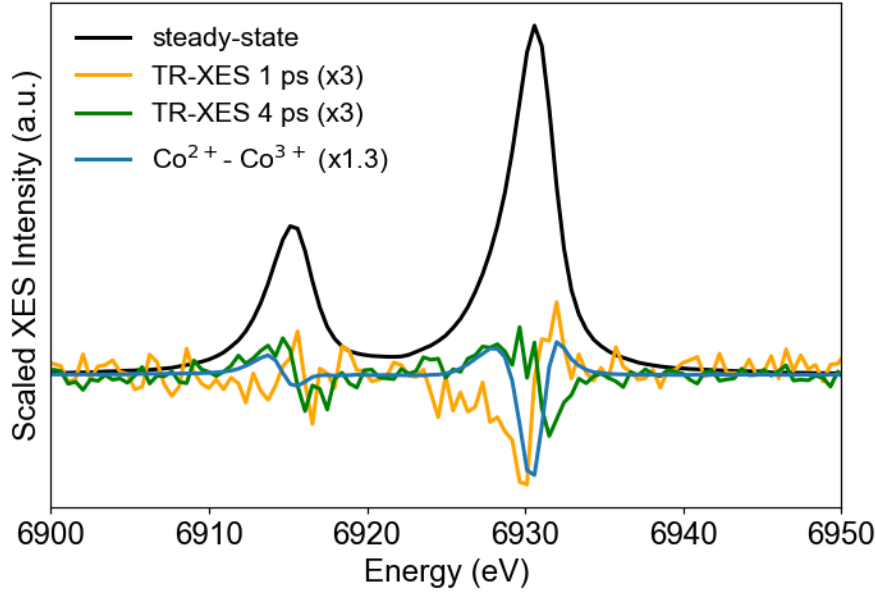
Figure 3.23: Normalized steady-state XES spectrum and TR-XES traces of the Co K$_{\alpha1}$ and K$_{\alpha2}$ emission lines of Co$_3$O$_4$, compared with the spectrum obtained subtracting the steady-state XES of Co(bpy)$_3^{3+}$ to the Co(bpy)$_3^{2+}$ one. Scaling factors of x3 and x1.3 were applied respectively to the transients at 1 ps and 4 ps, and to the Co^{2+}-Co^{3+} spectrum.

thick Co$_3$O$_4$ film) with 355 nm pump pulse and probing it with the 9.0 keV pink beam. The total acquisition time was of about 100 minutes. The results are shown in Figure 3.24(a,b). A distinct pump-probe signal is observed at K$_\alpha$ energies, with a small reduction of the K$_{\alpha1}$ maximum intensity at 6928 eV and an increase of the low-energy side of the K$_{\alpha2}$ line. At this pump fluence and with the employed X-ray flux, no pump-probe change could be observed at the K$_\beta$ line, due to the lower signal intensity with respect to the 6 times stronger K$_\alpha$ lines.

3.3.2.1 Discussion

Given the limited number of energy traces that could be acquired during the EXFEL experiment before the pump laser failure, a precise interpretation of the photoinduced TR-XES changes cannot be performed. However, several relevant aspects can be highlighted by a close analysis of this data set.

The significant differences of the K$_\alpha$ transients at 1 ps and 4 ps demonstrate that spin dynamics occurs on ultrafast time scales, consistent with the hypothesis of an electronic relaxation from the LMCT to d-d states. Indeed, at 1 ps the slow dynamics associated with the 710 fs time constant is still not complete, whereas the system has fully relaxed to a new state at 4 ps. Thus, for time delays shorter than 710 fs, more pronounced changes should be observed. By comparing the 4 ps and 2 ns transients, we notice that additional changes occur at K$_{\alpha1}$ energies, even though a higher SNR is needed to confirm this observation. Instead, the derivative-like shape of these two K$_{\alpha2}$ transients is quite similar. Additionally, the absence of a 2 ns pump-
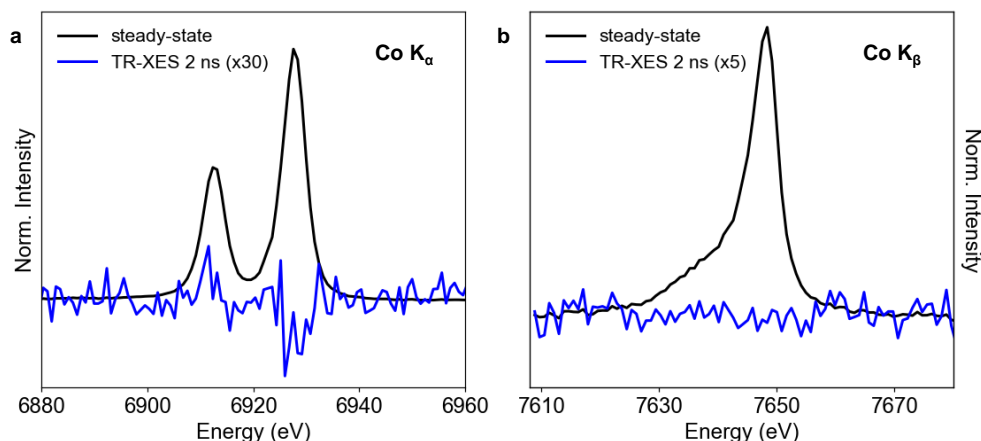
Figure 3.24: (a) Steady-state Co $K_{\alpha1}$ and $K_{\alpha2}$ XES lines of a 51 nm thick Co_3O_4 film and the TR-XES transient at 2 ns time delay (multiplied by a factor x30); (b) steady-state Co K_β XES line of a 51 nm thick Co_3O_4 film. No TR-XES transient is observed at 2 ns time delay with the measured signal to noise level. TR-XES transient was multiplied by a factor x5.

probe signal in Figure 3.24(b) implies that a better SNR is required to detect spin changes at the K_β line at this long time delays. These conditions are fully satisfied at the EXFEL, thanks to the higher photon flux of both pump and probe pulses.

Finally, the differences between the Co^{2+}-Co^{3+} spectrum and the 1 ps trace demonstrate that, at this time delay, the photoinduced spin configuration change of the Co_3O_4 cannot be described with a reduction of the octahedral Co^{3+} site. This finding supports the idea that upon LMCT excitation the system relaxes on sub-ps time scales into a state with different spin, consistently with the proposal of an ultrafast ISC process.

3.4 Conclusions

In this chapter we presented an investigation of the ultrafast photodynamics of spinel Co_3O_4 thin films upon selective excitation of ligand-to-metal charge-transfer and metal-to-metal charge-transfer optical transitions. Through femtosecond broadband reflectivity measurements, we have demonstrated that the sub-ps dynamics of the system strongly differs with the pump wavelength. Specifically, upon 400 nm excitation we observed two electronic relaxation processes with time scales of 260±30 fs and 710±40 fs, which we respectively associate to a convolution of Auger recombination and charge carrier thermalization, and to photocarrier cooling. This ultrafast incoherent response is associated with a coherent modulation of the reflectivity, ascribed to the generation of a displacive excitation of coherent phonons in the excited state. This conclusion is consistent with the absence of any Raman active phonon mode with an energy corresponding to the measured coherent oscillation (82 cm^{-1}). A strongly different response occurs upon 800 nm excitation, with slower incoherent relaxation processes (430±10 fs and 2.5±0.1 ps) and the generation of an impulsively stimulated Raman scattering phonon at 196 cm^{-1} in the electronic ground state of the system. The results rule out the

hypothesis of a cascade relaxation process that brings the system from the ligand-to-metal charge-transfer to the metal-to-metal charge-transfer and eventually to the low-energy d-d states. These findings are rationalized in terms of selective relaxation channels for the two different optical transitions that bring the system into the same d-d states localised on the Cobalt sites. In an atomic-like description, upon ligand-to-metal charge transfer excitation the Cobalt centres undergo an ultrafast intersystem crossing process that preserves the vibrational coherence induced by the impulsive excitation of the system. In order to provide a deeper understanding of the complex photoresponse of the system, which involves the correlated interaction of the electronic, spin and nuclear degrees of freedom, we proposed a combined investigation with femtosecond X-ray diffraction and X-ray emission spectroscopy techniques. The careful steady-state characterization of the experimental conditions required to prepare an ultrafast experimental campaign at Free electron laser facilities was presented. We also showed preliminary results obtained at the European X-ray free electron laser with time-resolved X-ray emission spectroscopy at the K$_\alpha$ lines upon 400 nm excitation, demonstrating the feasibility of the experiment and providing evidences for ultrafast spin changes in the system. Our results suggest that optical control of the Co$_3$O$_4$ charge carrier dynamics can be implemented upon selective excitation of the Co$_3$O$_4$ system with narrowband light pulses.

4 Toward time-resolved laser T-jump/X-ray probe spectroscopy in aqueous solutions

The following chapter is adapted from the article:

4.1   Abstract

Most chemical and biochemical reactions in Nature and in industrial processes are driven by thermal effects that bring the reactants above the energy barrier for reaction. In aqueous solutions, this process can also be triggered by the laser driven Temperature jump (T-jump) method, in which the water vibrational (stretch, bend or combination) modes are excited by a short laser pulse, leading to a temperature increase of the irradiated volume within a few picoseconds. The combination of the laser T-jump with X-ray spectroscopic probes would add element-specificity as well as sensitivity to the structure, the oxidation state and the spin state of the intermediates of reactions. Here, we present preliminary results of a near infrared pump/X-ray absorption spectroscopy (XAS) probe to study the ligand exchange of an octahedral aqueous Cobalt complex, which is known to pass through intermediate steps yielding tetrahedral chlorinated species. The structural changes of the chemical reaction are monitored with great sensitivity, even in the presence of a mild local increase in temperature. This work opens perspectives for the study of non-light-driven reactions using time-resolved X-ray spectroscopic methods.

4.2 Introduction

Most of chemistry and biochemistry that occurs in solution is driven by thermal activation, which brings the systems above the barrier for reaction, as described at the end of the XIXth century by Arrhenius [162]. The detailed study of (bio)chemical reactions has witnessed a huge leap forward with the advent of ultrafast (femtosecond to picosecond) spectroscopy [163], which marked the birth of Femtochemistry, allowing determination of the details of reaction pathways in a very wide variety of systems (gas phase, solutions, proteins, interfaces, etc.). In these studies, a short laser pump pulse triggers a photo-induced process (be it uni- or bi-molecular) in a system, whose evolution is followed by a second, short, "probe" pulse at variable time delay with respect to the pump pulse. The pump-probe method has universally been applied using pulses in the THz, infrared (IR), visible and ultraviolet ranges. Over the past twenty years, it has been extended to probes such as ultrashort pulses of electrons or X-rays [164], either via spectroscopy or scattering and diffraction. These deliver additional insights into the evolution of the excited system by providing information about electronic and, generally not possible by optical domain methods, about nuclear degrees of freedom. Even since the birth of Femtochemistry, exclusively photo-initiated reactions have been studied by probing them in "real-time". However, notwithstanding their importance in Nature and application, photo-induced processes represent only a subset of chemistry and biochemistry. It is therefore crucial to extend pump-probe spectroscopy to non-light driven reactions, and in particular to thermally-driven ones. To this aim, a fast thermal trigger is needed to initiate the process in order to fully exploit the temporal resolution of ultrafast spectroscopy.

In the early 1950s, Manfred Eigen and co-workers inaugurated the so-called relaxation methods in chemical kinetics, which consist of impulsively perturbing a system to trigger a reaction by a temperature (T-), a pressure (P-) or a pH-jump and monitoring the return to equilibrium [165]. The method was initially implemented in the microsecond time domain, but with the advent of pulsed lasers in the 1960s, it was pushed into the nanosecond/picosecond time domain and applied to chemical and biochemical reactions [166–171] using optical spectroscopy, in particular in aqueous solutions.

Water is the most important solvent in Nature and with the advent of ultrafast technology, short laser pulses have been utilized to induce T-jumps of 10-30°C in aqueous media. By directly exciting the water high frequency vibrational and/or bending modes, the non-radiative relaxation of the water dissipates the energy into the bulk solution on ultrafast time scales [172; 173], leading to an ultrafast (2-5 ps) temperature (T) increase of the irradiated volume. This impulsive T-increase can be used to locally trigger chemical reactions, whose evolutions are then monitored by optical probes [174; 175]. This innovative approach opens exciting perspectives in chemistry and functional biology, as it extends the range of applicability of ultrafast laser techniques beyond photochemistry, towards fast non-light-driven reactions.

While optical probes deliver a great degree of insight into the reactions, the identification of reactants, intermediates and products relies on an *a-priori* knowledge of their spectroscopic features. Indeed, visible and UV spectroscopies interrogate the global electronic properties of molecular systems. Optical spectroscopic observables are the energies and intensities of

valence electronic transitions, which are neither element-specific nor spin-sensitive and generally lack structural sensitivity. These limitations are, of course, transposed to time domain experiments. However, X-ray spectroscopies can overcome some of these. In particular, an X-ray absorption spectrum is characterised by edges, which represent the ionization threshold of specific core orbitals (K-edge for the 1s orbital, L_{1-3} for the 2s, $2p_{1/2}$ and $2p_{3/2}$ orbitals respectively, etc.) of the atom. At a given edge, features appear in the pre-edge region, which are due to transitions to empty or partially filled valence orbitals, providing information about the unoccupied density of states and the coordination symmetry (*via* the selection rules) of the investigated element. The edge itself is a sensitive probe of the element's oxidation state and its geometry, while the modulations of the absorption coefficient in the post edge region at low energies (the so-called X-ray near edge absorption structure or XANES) and at higher energies (the so-called extended X-ray absorption fine structure or EXAFS) contain information about bond lengths and angles of the coordinated surrounding atoms, *i.e.* they provide the local structure around the atom of interest [174; 175].

The past 20 years or so have witnessed the implementation of time-resolved X-ray techniques in the picosecond/femtosecond time domain at synchrotrons [176; 177] and more recently, at X-Ray Free Electron lasers (XFELs) [178; 179] for the study of chemical and biological systems in solution. These tools, which include X-ray absorption spectroscopy (XAS), X-ray emission spectroscopy (XES), X-ray solution scattering (XRS) and photoelectron spectroscopy of solutions [180], are now very well established. It therefore appears timely and even necessary to expand their use to the study of non-light driven reactions, and specifically, to thermally-driven ones. Wernet and co-workers implemented an experiment aimed at monitoring the structural changes in the hydrogen bond network of liquid water upon an impulsive T-jump heating. Specifically, they resonantly excited the intramolecular O–H stretch band of liquid water, inducing a T-jump of 20°C, and monitored the transient response by Oxygen K-edge absorption spectroscopy with 80 ps soft X-ray pulses from a synchrotron [181]. This very promising study was, to our knowledge, not further expanded to the investigation of actual thermally-driven chemical reactions with X-ray probes, let alone in the hard X-ray range. Notable exceptions are recent T-jump/X-ray Scattering studies of protein conformational changes from the ns to the ms time scales [182–185].

Here, we explore the possibility of laser T-jump/X-ray probe of a chemical reaction by monitoring a near-IR pump-induced ligand substitution reaction of a hexacoordinated Cobalt complex in a chlorinated aqueous solution by XAS at the Co K-edge. At room temperature (RT), the system consists of a mixture of aquo Cobalt complexes and, upon increasing temperature and/or chloride ion concentration, can be turned into a Co-tetrachloride complex according to (see Figure 4.1a):

$$Co(H_2O)_6^{2+} + 4Cl^- \rightleftharpoons CoCl_4^{2-} + 6H_2O \tag{4.1}$$
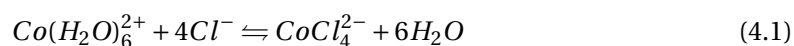
The choice of this model reaction is motivated by previous steady-state and time-resolved studies. The temperature dependence of the reaction had been investigated in detail using

Chapter 4. Toward time-resolved laser T-jump/X-ray probe spectroscopy in aqueous solutions
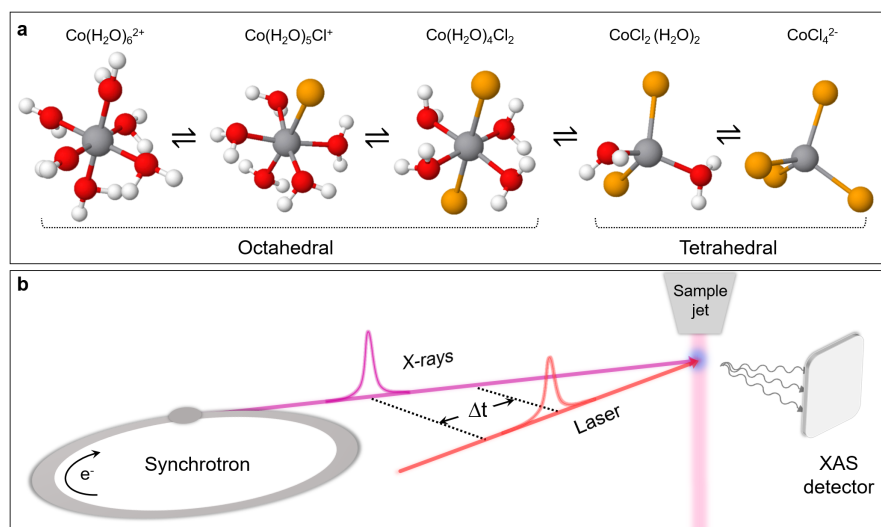
Figure 4.1: (a) Schematic layout of the investigated chemical reaction. The equilibrium can be tuned with changes in temperature or chloride concentration, causing free chloride ions to gradually replace water molecules. In parallel, structural interconversion occurs from the hexa-octahedral to chloro-tetrahedral configuration. (b) Experimental layout of the laser T-jump/X-ray absorption spectroscopy probe. The sample jet schematically represents the closed loop wire guided liquid jet employed in the experiment.

steady-state ultraviolet-visible (UV-visible) spectroscopy [186] and steady-state XAS [7]. The latter reported Co K-edge absorption spectra, as a function of T and/or chloride concentration (Cl$^-$). The authors identified the spectral signatures of the octahedral and tetrahedral species, along with those of the intermediates, establishing the reaction sequence (Figure 4.1a). Ma et al. [187] performed an ultrafast T-jump/optical probe study of the reaction exciting the overtone stretch mode of water at 1.55 μm. Three rate constants were reported and the analysis of their T-dependence was interpreted as supportive of the associative interchange reaction mechanism. The insights into the reaction kinetics and energetics provided by this study, along with the above mentioned steady-state investigations, serve as a basis for a proof-of-principle of the corresponding X-ray spectroscopic experiment.

Here, we explore the possibility of laser T-jump experiments in combination with an XAS probe. Our experiment uses a pump wavelength of 1.064 μm. At this wavelength not only the overtone vibrations of water are excited, but also of the dipole-forbidden d-d transition of the [Co(H$_2$O)$_6^{2+}$] complex (see below). Although this may not represent a pure T-jump, we argue how our results provide a basis for future T-jump/X-ray probe experiments of chemical reactions. We also speculate about novel perspectives for the investigation of T-activated chemical and biochemical processes using a broad range of X-ray spectroscopic (absorption, emission, photoelectron spectroscopies) and scattering (elastic and inelastic) techniques.

4.3   Methods

The measurements were carried out at the MicroXAS beamline of the Swiss Light Source (Paul Scherrer Institute, Villigen). The sample consists of a water solution of $[Co^{2+}]$=500 mM ($CoCl_2$ hexahydrate salt, abcr, purity 99.9%) and $[Cl^-]$=8 M (LiCl salt, Roth, purity 99% min.), which also accounts for the Chlorine contribution coming from the $CoCl_2$ salt. A closed loop wire-guided liquid jet (250 μm thickness) [174; 175] was employed as sample delivery system. The solution temperature was kept constant by means of a thermostat.

The experimental layout is schematized in Figure 4.1b. Transient XAS measurements were performed using the isolated hybrid X-ray pulse provided by the Swiss Light Source (SLS) synchrotron, with a time duration of 70 ps, to probe both the Co K-edge XANES and EXAFS regions. A high repetition-rate Duetto laser (10 ps pulses at 1064 nm fundamental wavelength, 32 μJ pulse energy) was utilized to excite the solution by pumping a combination mode of high-frequency overtones of the symmetric and antisymmetric stretching vibrations of water [172] and the d-d transition of the octahedral Cobalt complexes, in a near-collinear geometry to the X-ray beam. The data acquisition system is described in ref. [146]. We used the total fluorescence yield detection, with avalanche photodiodes in orthogonal geometry with respect to the X-ray beam. The X-ray signal was acquired on a pump-on/pump-off basis at 130 kHz, with the laser deliberately chosen to run at 65 kHz in order to increase the energy per pulse deposited into the irradiated volume. The jet speed (6 m/s) and the laser and X-rays spot sizes, respectively of 70x60 μm^2 and 50x50 μm^2 Full Width at Half Maximum (FWHM), were chosen to avoid multiple pumping of the same spot at the sample position. Reference steady-state X-ray absorption spectra were also recorded at the Co K-edge (7.700-7.800 keV, 2 eV step-size), using a Ketek fluorescence detector. Reagent and product spectra were, respectively, collected for a $[Co(H_2O)_6^{2+}]$=250 mM water solution at room temperature ($CoSO_4$, Roth, purity 99% min.) and a $[CoCl_4][N(CH_3)_4]_{2(s)}$ pellet (Sigma-Aldrich, purity 99.5% min.), a solid standard containing $CoCl_4^{2-}$ groups. In our experiment, the starting temperature, solute and salt concentrations, respectively T=60 °C, $[Co^{2+}]$=500 mM and $[Cl^-]$=8 M, were selected to demonstrate the sensitivity of the near-IR pumping scheme even in the extreme case of weak absorption regime from the solvent, yet maximizing the signal-to-noise ratio.

4.4   Results

In the chemical reaction under investigation (Figure 4.1a), the geometry of each intermediate is dictated by the crystal field stabilization energy [7; 188; 189], implying an octahedral configuration for the first three structures and a tetrahedral configuration for the last two. The equilibrium constant for the overall process is:

$$K_{eq}(T) = \frac{[CoCl_4^{2-}]}{[Co(H_2O)_6^{2+}][Cl^-]^4} \tag{4.2}$$

which indicates that the reaction is sensitive to the ligand concentration. Either an increase of the chloride ion concentration [Cl^-] or an increase in temperature, the reaction being endoergonic, promotes the gradual replacement of the coordinated water molecules by chloride ions, thereby moving the equilibrium in favour of the tetrahedral products. The determination of the [Co^{2+}], [Cl^-], and T parameters, which maximize both the XAS signal and the thermally-induced product formation, is key to the success of a T-jump experiment. The X-ray signal is proportional to the number of Cobalt centres dissolved in the solution. However, a high [Cl^-]/[Co^{2+}] is needed in order to move the equilibrium towards the product. Under this constraint, the upper limit to [Co^{2+}] is actually set by the solubility of LiCl in water. Therefore, a [Co^{2+}]=500 mM was chosen as a compromise, yielding a strong XAS signal while keeping the possibility of a high [Cl^-]/[Co^{2+}] ratio. Since the conversion process is accompanied by a colour change of the solution due to the characteristic absorption spectra of reagent and product, the optimal [Cl^-] and T values were determined using static UV-Visible spectroscopy, as seen in Figures 4.2a and 4.2b. In the literature, the absorption spectra have already been discussed in terms of ligand field theory [186; 190] and a detailed assignment of the bands was recently performed [191]. The broad band centred around 500 nm is associated with two weak Laporte-forbidden d-d electronic transitions of the octahedral species, whereas the feature in the 600-750 nm region is due to strong electronic transitions of the tetrahedral complexes. This region exhibits a partially-resolved fine structure, probably due to spin-orbit coupling and/or vibronic coupling [186].

Figure 4.2a shows the UV-Visible spectra for a [Co^{2+}]=1 M solution at two different temperatures, T=20°C and T=55°C, and for two different chloride concentrations, [Cl^-]=4 M and [Cl^-]=8 M. The presence of the 500 nm and 600-750 nm bands confirms the co-presence of reagents, intermediates and products under equilibrium conditions. Upon a temperature increase, a partial conversion from the hexa-aquo complex to the octahedral chlorinated intermediates and the tetrachloride complex occurs. The band centered at 510 nm increases and shifts towards the red, a behaviour associated with the partial conversion of the reagent into octahedral chlorinated species [191], while the intense 600-750 nm band increases in intensity due to the product formation. A similar effect occurs upon the increase of the chloride concentration from 4 to 8 M, which moves the equilibrium towards the products. The temperature effect is about 2.5 stronger for the [Cl^-]=8 M solution, meaning the product formation and the expected transient signal are higher the larger the chloride concentration. The T-effect on the UV-Visible spectra in the 30-60°C range and at constant [Cl^-] concentration is shown in Figure 4.2b for a [Co^{2+}]=1 M and [Cl^-]=7 M water solution. For the same temperature change of 5°C, the increase of the 600-750 nm product bands is more pronounced at higher temperature. Consequently, the experimental conditions that give a strong XAS signal and a strong temperature-induced complex conversion are at high [Co^{2+}] and [Cl^-] concentrations and at an elevated T. This set of parameters is consistent with those reported by Ma et al. in their T-jump/UV-Visible probe study [187]. The octahedral complexes also have a weak and broad band, which is centred at 1250 nm and has a width that covers a range from 1000 to 1600 nm, as seen in Figure 4.3. This band is assigned to a d-d transition from a non-bonding t_{2g} to an anti-bonding e_g^* orbital. We remark that, although this band contributes significantly
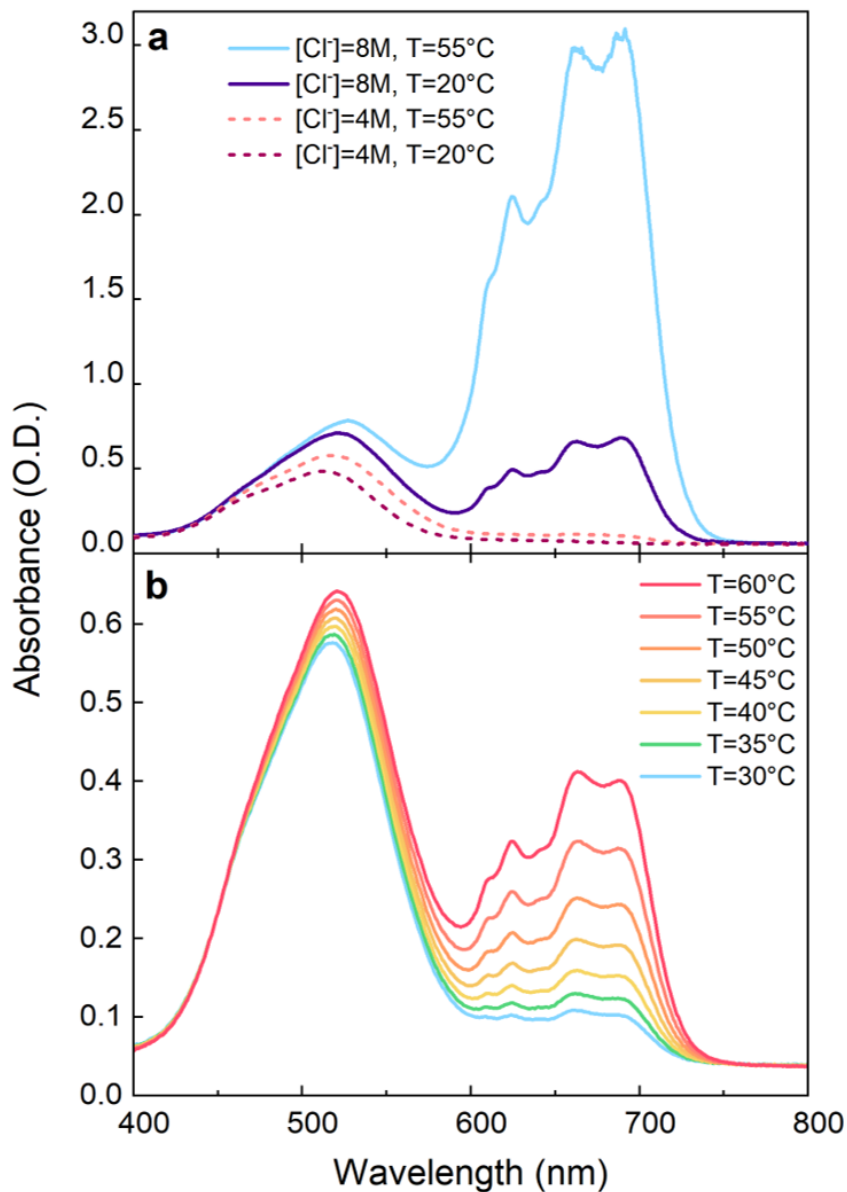
Figure 4.2: UV-visible spectra for a $[Co^{2+}]$=1 M solution. (a) Spectra at two different temperatures, T=20 °C and T=55 °C , $[Cl^-]$=4 M (dashed curves) and $[Cl^-]$ =8 M (solid curves). (b) The effects of the temperature in the range of 30–60 °C for a $[Cl^-]$=7 M solution. The strong increase in the 600–750 nm bands is associated with the tetrahedral product formation, while the redshift of the 500 nm band is related to the formation of octahedral chlorinated intermediates.

to the absorption in the region of our pump wavelength, under the assumptions we explain below, we believe the conclusions constitute evidence for a T-jump experiment probed with XAS. We recorded the steady-state XAS spectra at 60 and 80 °C in order to determine the X-ray spectroscopic changes expected under a significant temperature increase (Figure 4.4a).
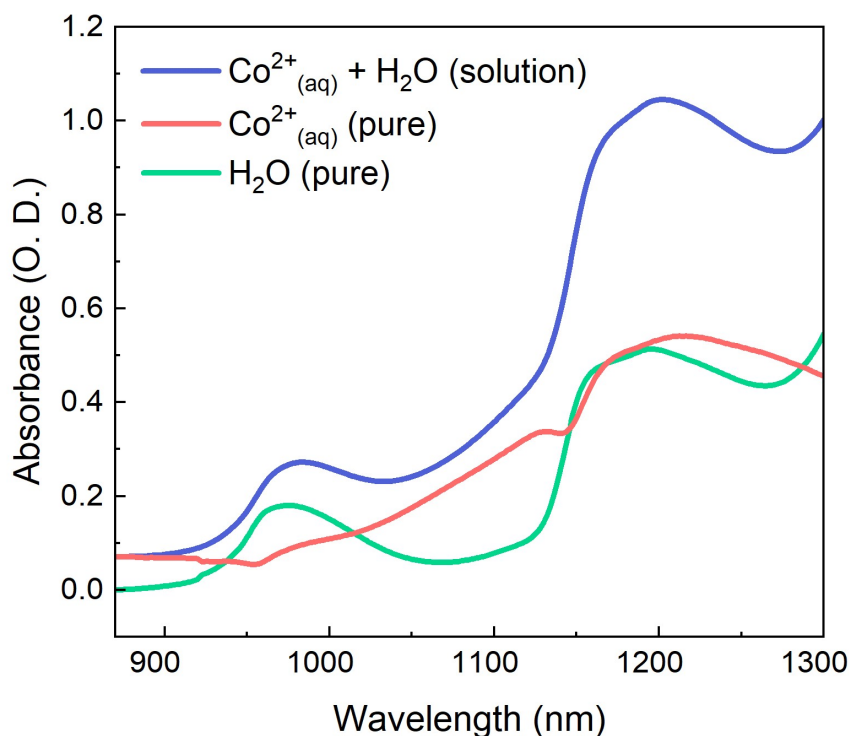
Figure 4.3: Static UV-visible reference spectra of the $[Co^{2+}]$=500 mM, $[Cl^-]$=8 M water solution (blue trace), compared to pure water (green trace) and the pure Cobalt contribution (red trace, taken from the difference between the blue and the green traces). A common offset was subtracted from both the spectra, corresponding to the intensity of the pure water solution at 860 nm, where, according to Ref. [6], the absorbance of the water is almost negligible.

The XAS spectra exhibit a prominent white line at the edge at 7.725 keV, associated with the 1s→4p Cobalt core transition, whose intensity decreases with temperature. Post-edge intensity changes are observed around two isosbestic points at 7.737 and 7.757 keV, in agreement with the results of Liu et al. [7]. We therefore set the sample aqueous solution ($[Co^{2+}]$=500 mM, $[Cl^-]$=8 M) to T=60 °C and utilized the 1064 nm laser light to pump the system, which was probed by XAS at 7 ns time delay. The choice of the time-delay is based on the results of ref. [187], which showed that after 4 ns the concentrations of reagents and products have plateaued and the equilibrium associated with the new temperature is established. Thus, both the 7 ns pump-probe transient and the difference of steady-state XAS correspond to the subtraction of two spectra that reflect the distribution of Cobalt complexes equilibrated at two different temperatures. The same results are compared, bearing in mind that the transient spectrum shows a laser induced effect and not a difference of steady-state spectra. Figure 4.4a shows the transient XAS signal at 7 ns (red dots) and the difference of the steady-state XAS spectra at 80 and 60 °C (black solid line), which are in excellent agreement.

The interpretation of the transient signal requires the knowledge of the XAS features as structural fingerprint of the Cobalt complexes. To this aim, we measured the spectra of the reference compounds corresponding to the start $Co(H_2O)_6^{2+}$ $_{(aq)}$ and end $CoCl_4^{2-}$ $_{(s)}$ species of the reac-
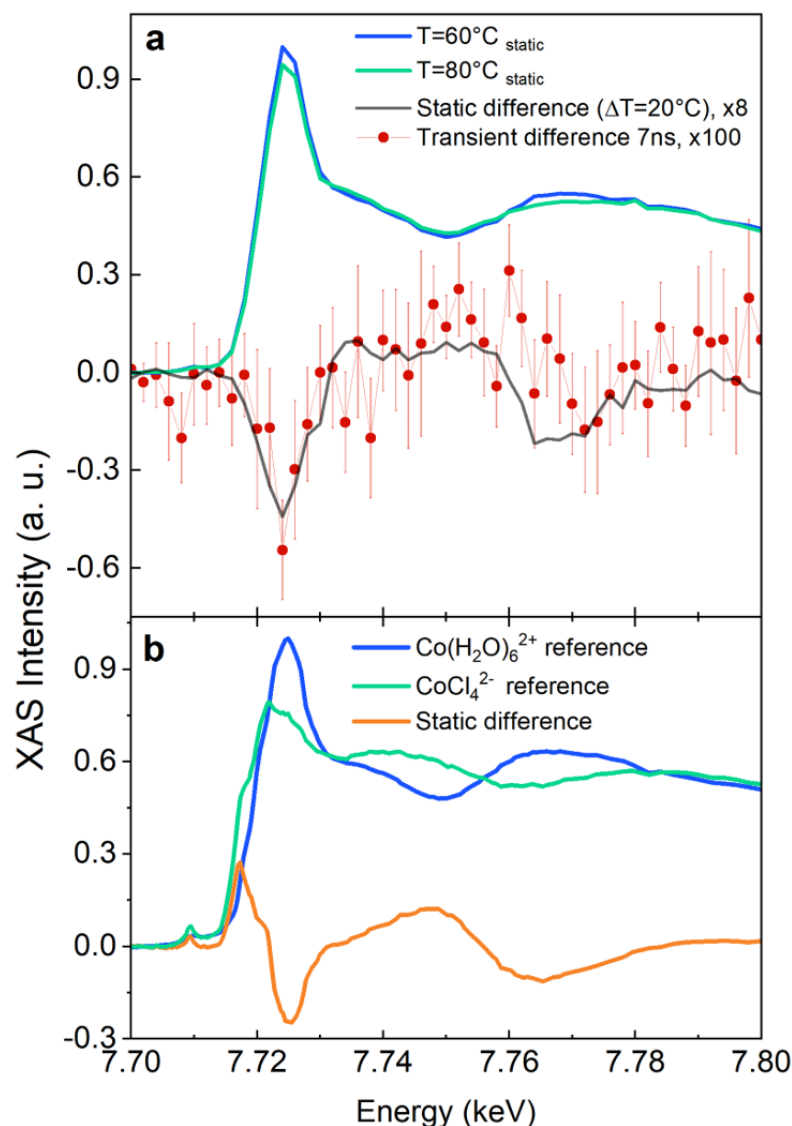
Figure 4.4: Laser T-jump/XAS probe study on a $[Co^{2+}]$=500 mM, $[Cl^-]$=8 M water solution. (a) Static XAS spectra were taken without the laser at 80 °C (green) and 60 °C (blue). The difference between the two static XAS spectra at T=80 °C and T=60 °C is displayed by the black trace (scaled by x8) and overlaid with the pump-probe data (scaled by x100) obtained at 7 ns by the laser-induced T-jump (red dots). The static spectra were scaled with a common factor (maximum of the T=60 °C curve), keeping the presence of the isosbestic points. (b) Reference static X-ray absorption spectra at the Co K-edge. Blue: $[Co(H_2O)_6^{2+}]$= 250 mM water solution at room temperature. Green: $[CoCl_4][N(CH_3)_4]_{2(s)}$ pellet. Their static difference is displayed by the orange solid curve. The spectra were scaled in order to have the same integrated area below the curves. In this way, the presence of the isosbestic points is retrieved.

tion. These spectra are shown in Figure 4.4b, along with their static difference. The latter shows an intensity drop around the main peak at 7.725 keV (the so-called white line) and the appear-

ance of post-edge modulations. Both the intensity drop of the white line and the post-edge modulations are reminiscent of those observed in the 7 ns transient (Figure 4.4a). However, two additional features appear in the static difference of Figure 4.4b: a small pre-edge peak related with 1s→3d Cobalt electronic transitions, and an intense shoulder in the 7.716-7.720 keV range. To rationalize these differences, we compare our spectra with those of Liu et al. in [7], which we have digitized and show in Figure 4.5. These authors reported a systematic investigation of chloride concentration and temperature effects on the steady-state Co K-edge absorption spectra for an aqueous Cobalt(II) chloride solution. Specifically, they identified the XAS spectra of the reagents and the mixture of the two tetrahedral products through a principal component analysis, *i.e.* a data set reduction of the recorded XAS spectra. Their XAS analysis shows that the decrease of the white line intensity is spectrally related with the conversion of the reagent into the octahedral chlorinated intermediates (red trace), whereas the presence of the shoulder and of the main edge depletion is ascribed to the formation of Cobalt chloride tetrahedral species (green trace), also consistent with the conclusions of a recent *in-situ* XAS investigation [192]. The agreement between our transient data at 7 ns (Figure 4.4a) and the static difference for the reagent-octahedral intermediate mixture (Figure 4.5) suggests that, in the present experiment, the excitation drove the equilibrium towards a mixture of the octahedral intermediate species, $Co(H_2O)_5Cl^+$ or $Co(H_2O)_4Cl_2$, without structural conversion to tetrahedral complexes.

4.5 Discussion

Assuming all absorbed photons end up heating the irradiated volume, the peak temperature jump can be estimated following Wang et al. [173]:

$$\Delta T = \frac{2E\alpha}{A\rho C_v} \tag{4.3}$$

where E is the laser pulse energy (32 μJ), α is the absorption coefficient of the solution at 1064 nm, A is the laser spot area at the focus, ρ is the water density and C_v is the water heat capacity at room temperature. In our experimental conditions, ΔT corresponds to a mild increase of 0.13 °C. As a comparison, previously reported T-jump experiments pumped the water absorption peaks located either at 3400 cm^{-1} or 6600 cm^{-1}, where the absorption coefficient is ~10^2-10^4 stronger [6]. Under those conditions, ΔTs of 20-40 °C [181] or 5-10 °C [187] were produced using very high fluences. As previously mentioned, the absorption at 1064 nm is both due to water and to the hexacoordinated complexes (Figure 4.3). Our estimate of the absorption coefficient α at 1064 nm accounts for both the contribution from the water, α = 0.06 cm^{-1}, and that of $Co(H_2O)_6^{2+}$, for which α = 0.21 cm^{-1} with $[Co^{2+}]$=500 mM. Since most of the absorption at 1064 nm is due to the d-d transition [186] of the complexes, one may question whether the observed effects are really due to thermal effects or are caused by photodissociation of an H_2O ligand followed by association Cl$^-$ one.
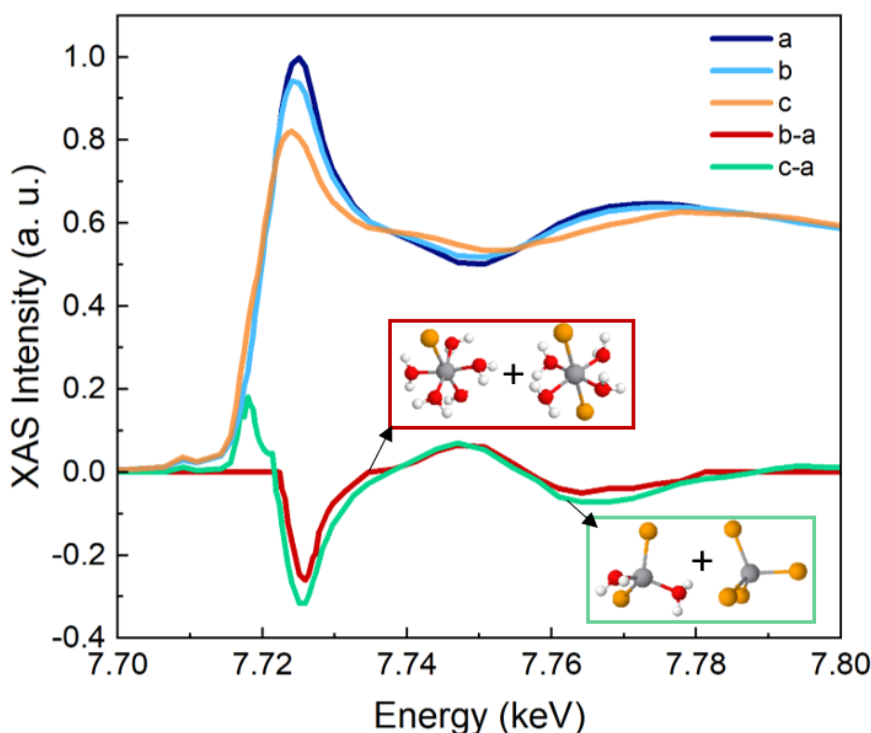
Figure 4.5: Assignment of spectral features to reaction intermediates. All traces were digitized as is from Ref. [7]. In this panel, (a) NaCl=0 M, 250 °C; (b) NaCl=0.5 M, 250 °C; (c) NaCl=1.5 M, 250 °C. The red solid line corresponds to (b-a) (scaled x4), and it is ascribed to the octahedral compound mixture formation. The green solid line corresponds to (c-a), and it is ascribed to the tetrahedral compound mixture formation at the expenses of the reagent.

In the event where there is no photo-dissociation of octahedral Cobalt complexes, it is most likely that the intramolecular relaxation of the excited complex will lead to a heat release to the environment. A good example is provided by the case of aqueous $[Fe(CN)_6]^{3+}$ where the heating of water was found to be on the same time scale (few picoseconds) as the vibrational cooling of the CN stretch frequencies [193]. In addition, a long-lived excited state can reasonably be excluded based on the results of pump-probe experiments of octahedral Co(III) or Co(II) complexes, which show that the relaxation of the systems is complete in few picoseconds [194; 195].

In the event of photodissociation of octahedral Cobalt complexes and considering that at the present concentrations there are 16 Cl atoms and 111 water molecules per octahedral complex, the probability of associating a Cl^- ion to the pentacoordinated fragment is not negligible. However, these events generally take place at much shorter time scales than the nanosecond regime. For example, in the case of aqueous $[Fe(CN)_6]^{4+}$ the uptake of a water molecule after dissociation of a CN fragment requires ~20 ps [196]. In the case of hexacarbonyl metals such as Cr, W and Mo, association times were in the few ps time scale [197]. Finally, in the case of aqueous cis-$[Ru(bpy)_2(CH_3CN)_2]Cl_2$ the substitution of one of the CH_3CN ligands by a water molecule requires ~80 ps [198]. Accounting for the hypothetical presence of

chlorinated species generated with photo-dissociation of the reagent, their contribution to a transient signal would be short lived. Indeed, in the absence of a temperature change, the thermal reaction would be responsible of re-establishing the equilibrium distribution of the Co complexes dictated by the starting temperature, fulfilling the conditions imposed by Eq. 4.3 and washing out any out-of-equilibrium photo-products. Provided the chemical reaction is investigated at longer time scales than the time required for the thermal reaction to occur, no photo-products will be probed. The T-jump optical-domain investigation of the same reaction [187] showed that the thermally-induced product formation is complete in about 4 ns. Therefore, based on simple kinetics and thermodynamical arguments we can safely exclude any direct photo-induced product formation, via dissociation-association, to the observed transient signal at the long time delays considered here (7 ns).

Based on these premises, the laser induced effect can be interpreted as a genuine T-jump at 7 ns. The above results allow us to elaborate more on the T-jump approach in general and on its difference with respect to static (*in-situ*) investigation. *in-situ* methods change the steady-state, average distribution of the species involved in the chemical equilibrium [7]. The T-jump instead locally triggers a chemical equilibrium away from the reagents, and it acts as a tool to isolate - at specific time delays - the effect of the ongoing reaction with respect to the initial conditions, eventually reaching the equilibrium associated with the new temperature and converging to the steady state results. In a general picture, the amplitude of the sudden temperature increase impacts on the speed of the reaction rate (Arrhenius law) and on the number of molecules involved in the chemical transformation. The former determines which intermediates/products will be probed, the latter how strong the transient signal will be. In our experiment, the XAS spectrum associated to a mild T-jump of 0.13 °C shows the same profile as the difference of steady state spectra being 20 °C apart (Figure 4.4a). This implies that the same octahedral intermediates are produced at the expense of the reagent. However, the amount of the reagents converted in these two cases is different, leading to transients of significantly different intensities. This concept is schematized in Figure 4.6: upon a 0.13 °C T-jump, the distribution of energy changes among the complexes and within 7 ns, the chemical equilibrium at the higher temperature is established. This includes a larger amount of octahedral intermediates and, probably, a minor population of tetrahedral products whose signal is not sufficient to overcome the noise of our measurement. This scheme allows us to suggest a reaction landscape where the reagents are thermodynamically more stable than the octahedral intermediates which, in turn, are more stable than the tetrahedral products (Figure 4.1). No kinetic information is retrieved without the time evolution of the concentration of the species, representing the final goal of the investigation of the reaction mechanism. In this respect, XAS represents a powerful complementary approach to the UV-Visible spectroscopy of a T-jump induced processes. In the optical domain, the $CoCl_4^{2-}$ absorption band is strong enough to allow the detection of products, even under experimental conditions where their concentration is almost negligible. Instead, X-ray probing is sensitive to the relative weight of all chemical species, pointing to a large majority of octahedral complexes and providing structural information about the elusive reaction intermediates.
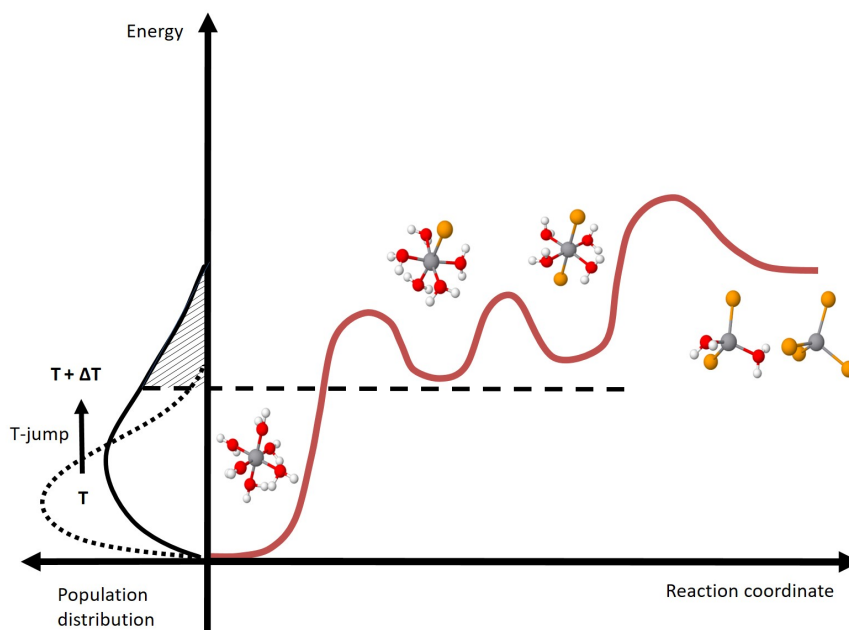
Figure 4.6: Schematic of the energy landscape as a function of the reaction coordinate for the investigated chemical equilibrium: changes of the energy distribution of the complexes as a function of temperature (left) and related conversion of the reagent into intermediates and products (right).

4.6 Conclusion and outlook

The present study is a first step towards implementing X-ray probing of fast thermally-induced chemical reactions in solutions. By pumping an aqueous solution containing hexacoordinated Co^{2+} ions in the presence of a high concentration of Cl^- ions using a 10 ps pulse at 1064 nm, we have driven, up to the octahedral chlorinated intermediates, the reaction that ultimately leads to a tetrachloro-complex. The products were detected by X-ray absorption spectroscopy using 70 ps X-ray pulses from a synchrotron. The exquisite sensitivity to chemical composition and structure makes X-ray spectroscopy ideal to observe chemical and biochemical reactions under their most common and relevant conditions. The present work calls for further studies to fully benefit of the X-ray probing of thermally induced reactions. First, the choice of the laser pump wavelength should be tuned to the red, typically around 1.5 μm, in the overtone of the water stretch mode, in order to more efficiently heat the irradiated volume and thus increase both the transient signal and the reaction rate, avoiding any direct excitation of the educt. Second, because of the ultrafast (2-5 ps) heating of liquid water, extending the method to shorter time scales, *i.e.* faster thermally driven reaction, is now possible, using synchrotron pulses (70 ps) or even X-ray free electron laser pulses (<100 fs). Third, the implementation of the T-jump method with X-ray probing is by no means limited to X-ray absorption spectroscopy but can be extended to X-ray scattering, X-ray emission spectroscopy and liquid phase photoelectron spectroscopy. In particular, the latter two should help distinguish the various intermediates in terms of speciation, while the structural information is derived from XAS. Furthermore, with

the development of new delivery schemes of solutions into vacuum [199; 200], the extension of T-jump induced reactions using soft X-ray probing is now possible, with the advantage that light elements such as N, C, O, F, etc. can be selectively detected, opening perspectives to study organic and biochemical reactions in solution. We believe the present results represent an opportunity to extend the investigation of chemical reactions at synchrotrons and X-ray Free electrons lasers beyond photo-induced ones into temperature-driven (bio)chemical processes.

Conclusions and future perspectives

Ultrafast spectroscopic methods represent powerful probes to investigate the nonequilibrium properties of a system. The combination of multiple techniques ranging from the optical to the hard X-ray domain enables to explore the photoresponse of a material from different perspectives, offering a comprehensive description of the fundamental interactions of its internal degrees of freedom. In this thesis we presented synergistic approaches to unravel the response to external perturbations of two class of complex systems, lead-halide perovskites and transition metal oxides, providing atomic level details of their structures and functions.

We showed the first structural quantification of polaronic distortions in $CsPbBr_3$ nanocrystals upon above band gap excitation, clarifying its origin and monitoring the recovery of its equilibrium state. Time-resolved and temperature-dependent X-ray absorption spectroscopy methods were combined to disentangle the subtle interplay between electronic-induced and photothermal effects caused by the pump pulse, demonstrating that the observed photodynamics is purely electronic driven. This aspect is receiving growing attention in the ultrafast community, as nonequilibrium thermalization is an unavoidable side effect of the electronic relaxation of the system. As a consequence, the correct interpretation of the photoinduced dynamics of a material requires characterizing and understanding thermal responses in thermodynamic equilibrium conditions.

We achieved a better comprehension of the temperature-induced changes in $CsPbBr_3$ nanocrystals complementing steady-state X-ray diffraction and X-ray absorption spectroscopy measurements across the system's phase diagram with accurate *ab-initio* simulations. Our findings clarified the role of thermal fluctuations and phonon anharmonicity in the high temperatures phase of the system, inducing local disorder increase, rather than a structural symmetry increase, which underlies the temperature-dependent changes in the diffraction and X-ray absorption observables.

These results pave the way for a femtosecond investigation of the photoresponse of lead-halide perovskites in the hard X-ray domain. The high photon energies required to probe

the halogen K- and lead L_3- edges are becoming accessible thanks to the recent technical development of the European X-ray free electron laser and the Linac Coherent Light Source II. Performing ultrafast X-ray absorption and emission spectroscopic studies will enable to map the electronic and structural dynamics of perovskites with element- and oxidation-state selectivity. These experiments will shed light on the ultrafast structural dynamics leading to the formation of polarons, possibly highlighting the lattice changes which are mainly involved. Perhaps, the latter represent the most important question to address about the photoresponse of lead-halide perovskites, as polarons are deemed to be at the origin of the exceptional op-toelectronic properties of these materials. However, whether this is related to the chemical composition of the lead-halide framework or to the more general perovskite structure has not been verified yet. Oxide perovskite materials were largely investigated in the past using steady-state techniques, due to the pronounced changes in their physical properties upon external perturbations. Less studied is their photodynamics on ultrafast time scales, in contrast with the extensive investigations accomplished for lead-halide systems. Filling the gap between these two families requires comparing electronic and structural responses of the oxide and lead-halide perovskites using both pump-probe optical and X-ray techniques.

The strong interplay between nuclei, electrons and spins also determines the photodynamics in transition metal oxide materials. We have presented an ongoing research campaign on a prototypical system, spinel Co_3O_4, in which a deeper understanding of its complex light-induced response is provided by combining tabletop and large scale facility experiments. Our femtosecond broadband reflectivity study in the visible domain demonstrated that the selective excitation of the electronic transitions of the system leads to distinct relaxation pro-cesses in the first picoseconds of the dynamics. Different coherent (nuclear) and incoherent (electronic) responses were observed upon 400 nm and 800 nm excitations, respectively in resonance with ligand-to-metal and metal-to-metal charge transfer optical transitions. We proposed the presence of an ultrafast intersystem crossing process which is specifically active for the ligand-to-metal charge transfer transition. This hypothesis, which implies spin config-uration changes on sub-ps time scales, is supported by our preliminary time-resolved X-ray emission spectroscopy results at the Cobalt K_α lines. However, a more extensive investigation is needed to confirm or invalidate this proposal. To this aim, we will perform a study of the correlated structural, spin and electronic responses of the system upon 400 nm and 800 nm excitations *via* parallel detection of femtosecond X-ray diffraction and femtosecond X-ray emission spectroscopy. The beamtime, which is scheduled for next summer at the European X-ray free electron laser, will unravel the fundamental steps determining the ultrafast elec-tronic relaxation from the charge transfer to the Mott-Hubbard band gaps in spinel Co_3O_4. This achievement is not only relevant for applications in solar energy conversion and pho-tocatalysis, but it also represents an important step forward in the understanding of excited state dynamics in transition metal oxide systems.

In the near future, we envisage additional X-ray experiments on Co_3O_4 under resonant con-ditions, providing a wealth of information that non-resonant techniques cannot access. In fact, thanks to the oxidation state selectivity of X-ray absorption and emission spectroscopies, the photon energy of the probe can be tuned in resonance with the Co^{2+} or Co^{3+} centres,

selectively mapping the photodynamics of the tetrahedral and octahedral centres in the spinel structure. This system also represents an ideal benchmark for investigating the influence of electronic excitations on the spin collective dynamics at low temperature. With respect to the more studied magnetite (spinel Fe_3O_4), Co_3O_4 does not present a Verwey transition, and below 40 K it has an antiferromagnetic arrangement where each Co^{2+} (s=3/2) is tetrahedrally surrounded by four nearest neighbours, oppositely spin oriented Co^{2+} ions. The Co^{3+} (s=0) sites, instead, form a magnetically silent pyrochlore lattice in which a photoexcitation of ligand-to-metal or metal-to-metal charge transfer transitions can transiently change their electronic configuration. This process should impulsively activate new exchange interactions in the spin lattice, causing geometrical frustration. In this framework, resonant inelastic X-ray scattering can be exploited to study low-lying local and collective excitations of the Cobalt sites with elemental- and site-selectivity. In its time-resolved implementation, it will directly track the photoinduced changes of the antiferromagnetic order in the material through the magnon fingerprint time evolution in the energy loss spectrum, following the breaking and revival of magnetic order. Such a study will explore the possibility to optically control the phase transition from an antiferromagnetic arrangement to spin-liquid phase, helping to understand frustration and the closely related superconductivity phenomenon.

We concluded the thesis by presenting a possible implementation of the temperature-jump technique into the X-ray domain for the study of thermal chemical reactions in water solution. This experiment relies on the same scheme of a standard pump-probe method, but the pump pulse is used to induce a prompt temperature change of the bulk solution *via* ultrafast relaxation of the vibrationally excited water molecules. We discussed preliminary results obtained for a model reaction, namely a chloride ligand substitution of an octahedral aqueous Cobalt complex, in which the structural changes were observed with precision thanks to the local structural sensitivity of the X-ray absorption probe. In this work, a first step toward the development of this method with X-ray spectroscopy techniques is accomplished, opening a new perspective for the study of thermally-driven chemical reactions in solution and biochemical processes in physiological media, which represent the vast majority in Nature.

Bibliography

[1] K. Momma and F. Izumi. VESTA 3 for three-dimensional visualization of crystal, volumetric and morphology data. *Journal of Applied Crystallography*, 44(6):1272–1276, December 2011.

[2] Matthew S. Kirschner, Benjamin T. Diroll, Peijun Guo, Samantha M. Harvey, Waleed Helweh, Nathan C. Flanders, Alexandra Brumberg, Nicolas E. Watkins, Ariel A. Leonard, Austin M. Evans, Michael R. Wasielewski, William R. Dichtel, Xiaoyi Zhang, Lin X. Chen, and Richard D. Schaller. Photoinduced, reversible phase transitions in all-inorganic perovskite nanocrystals. *Nature Communications*, 10(1):504, December 2019.

[3] Martin T. Dove. Theory of displacive phase transitions in minerals. *American Mineralogist*, 82(3-4):213–244, April 1997.

[4] Matthias M. Waegele, Hoang Q. Doan, and Tanja Cuk. Long-Lived Photoexcited Carrier Dynamics of d–d Excitations in Spinel Ordered Co_3O_4. *The Journal of Physical Chemistry C*, 118(7):3426–3432, February 2014.

[5] Amélie Bordage, Virgile Trannoy, Olivier Proux, Hugo Vitoux, Robinson Moulin, and Anne Bleuzen. In situ site-selective transition metal K-edge XAS: A powerful probe of the transformation of mixed-valence compounds. *Physical Chemistry Chemical Physics*, 17(26):17260–17265, May 2015.

[6] John E. Bertie and Zhida Lan. Infrared Intensities of Liquids XX: The Intensity of the OH Stretching Band of Liquid Water Revisited, and the Best Current Values of the Optical Constants of H_2O(l) at 25°C between 15,000 and 1 cm $^{-1}$. *Applied Spectroscopy*, 50(8):1047–1057, August 1996.

[7] Weihua Liu, Stacey J. Borg, Denis Testemale, Barbara Etschmann, Jean-Louis Hazemann, and Joël Brugger. Speciation and thermodynamic properties for cobalt chloride complexes in hydrothermal fluids at 35–440°C and 600bar: An in-situ XAS study. *Geochimica et Cosmochimica Acta*, 75(5):1227–1248, March 2011.

[8] Xiao-Ke Liu, Weidong Xu, Sai Bai, Yizheng Jin, Jianpu Wang, Richard H. Friend, and Feng Gao. Metal halide perovskites for light-emitting diodes. *Nature Materials*, 20:1–12, September 2020.

[9] Brandon R. Sutherland and Edward H. Sargent. Perovskite photonic sources. *Nature Photonics*, 10(5):295–302, May 2016.

[10] Yanjun Fang, Qingfeng Dong, Yuchuan Shao, Yongbo Yuan, and Jinsong Huang. Highly narrowband perovskite single-crystal photodetectors enabled by surface-charge recombination. *Nature Photonics*, 9(10):679–686, October 2015.

[11] Rui Su, Sanjib Ghosh, Jun Wang, Sheng Liu, Carole Diederichs, Timothy C. H. Liew, and Qihua Xiong. Observation of exciton polariton condensation in a perovskite lattice at room temperature. *Nature Physics*, 16(3):301–306, March 2020.

[12] Hendrik Utzat, Weiwei Sun, Alexander E. K. Kaplan, Franziska Krieg, Matthias Ginterseder, Boris Spokoyny, Nathan D. Klein, Katherine E. Shulenberger, Collin F. Perkinson, Maksym V. Kovalenko, and Moungi G. Bawendi. Coherent single-photon emission from colloidal lead halide perovskite quantum dots. *Science*, 363(6431):1068–1072, March 2019.

[13] Quinten A. Akkerman, Gabriele Rainò, Maksym V. Kovalenko, and Liberato Manna. Genesis, challenges and opportunities for colloidal lead halide perovskite nanocrystals. *Nature Materials*, 17(5):394–405, May 2018.

[14] Samuel D. Stranks, Giles E. Eperon, Giulia Grancini, Christopher Menelaou, Marcelo J. P. Alcocer, Tomas Leijtens, Laura M. Herz, Annamaria Petrozza, and Henry J. Snaith. Electron-Hole Diffusion Lengths Exceeding 1 Micrometer in an Organometal Trihalide Perovskite Absorber. *Science*, 342(6156):341–344, October 2013.

[15] Guichuan Xing, Nripan Mathews, Shuangyong Sun, Swee Sien Lim, Yeng Ming Lam, Michael Grätzel, Subodh Mhaisalkar, and Tze Chien Sum. Long-Range Balanced Electron- and Hole-Transport Lengths in Organic-Inorganic $CH_3NH_3PbI_3$. *Science*, 342(6156):344–347, October 2013.

[16] Laura M. Herz. Charge-Carrier Dynamics in Organic-Inorganic Metal Halide Perovskites. *Annual Review of Physical Chemistry*, 67(1):65–89, February 2016.

[17] Kiyoshi Miyata, Timothy L. Atallah, and X.-Y. Zhu. Lead halide perovskites: Crystalliquid duality, phonon glass electron crystals, and large polaron formation. *Science Advances*, 3(10):e1701469, October 2017.

[18] Alexander N. Beecher, Octavi E. Semonin, Jonathan M. Skelton, Jarvist M. Frost, Maxwell W. Terban, Haowei Zhai, Ahmet Alatas, Jonathan S. Owen, Aron Walsh, and Simon J. L. Billinge. Direct Observation of Dynamic Symmetry Breaking above Room Temperature in Methylammonium Lead Iodide Perovskite. *ACS Energy Letters*, 1(4):880–887, October 2016.

[19] Federica Bertolotti, Loredana Protesescu, Maksym V. Kovalenko, Sergii Yakunin, Antonio Cervellino, Simon J. L. Billinge, Maxwell W. Terban, Jan Skov Pedersen, Norberto

Masciocchi, and Antonietta Guagliardi. Coherent Nanotwins and Dynamic Disorder in Cesium Lead Halide Perovskite Nanocrystals. *ACS Nano*, 11(4):3819–3831, April 2017.

[20] Kiyoshi Miyata, Daniele Meggiolaro, M. Tuan Trinh, Prakriti P. Joshi, Edoardo Mosconi, Skyler C. Jones, Filippo De Angelis, and X.-Y. Zhu. Large polarons in lead halide perovskites. *Science Advances*, 3(8):e1701217, August 2017.

[21] Patrick Cottingham and Richard L. Brutchey. Depressed Phase Transitions and Thermally Persistent Local Distortions in CsPbBr$_3$ Quantum Dots. *Chemistry of Materials*, 30(19):6711–6716, October 2018.

[22] Y. Fujii, S. Hoshino, Y. Yamada, and G. Shirane. Neutron-scattering study on phase transitions of CsPbCl$_3$. *Physical Review B*, 9(10):4549–4559, May 1974.

[23] Maksym V. Kovalenko, Loredana Protesescu, and Maryna I. Bodnarchuk. Properties and potential optoelectronic applications of lead halide perovskite nanocrystals. *Science*, 358(6364):745–750, November 2017.

[24] Constantinos C. Stoumpos, Christos D. Malliakas, John A. Peters, Zhifu Liu, Maria Sebastian, Jino Im, Thomas C. Chasapis, Arief C. Wibowo, Duck Young Chung, Arthur J. Freeman, Bruce W. Wessels, and Mercouri G. Kanatzidis. Crystal Growth of the Perovskite Semiconductor CsPbBr$_3$: A New Material for High-Energy Radiation Detection. *Crystal Growth & Design*, 13(7):2722–2727, July 2013.

[25] Richard J. Worhatch, HyunJeong Kim, Ian P. Swainson, André L. Yonkeu, and Simon J. L. Billinge. Study of Local Structure in Selected Organic–Inorganic Perovskites in the Pm$\overline{3}$m Phase. *Chemistry of Materials*, 20(4):1272–1277, February 2008.

[26] Andrea Bernasconi and Lorenzo Malavasi. Direct Evidence of Permanent Octahedra Distortion in MAPbBr$_3$ Hybrid Perovskite. *ACS Energy Letters*, 2(4):863–868, April 2017.

[27] Omer Yaffe, Yinsheng Guo, Liang Z. Tan, David A. Egger, Trevor Hull, Constantinos C. Stoumpos, Fan Zheng, Tony F. Heinz, Leeor Kronik, Mercouri G. Kanatzidis, Jonathan S. Owen, Andrew M. Rappe, Marcos A. Pimenta, and Louis E. Brus. Local Polar Fluctuations in Lead Halide Perovskite Crystals. *Physical Review Letters*, 118(13):136001, March 2017.

[28] Simon C. Boehme, Stephanie ten Brinck, Jorick Maes, Nuri Yazdani, Felipe Zapata, Kai Chen, Vanessa Wood, Justin M. Hodgkiss, Zeger Hens, Pieter Geiregat, and Ivan Infante. Phonon-Mediated and Weakly Size-Dependent Electron and Hole Cooling in CsPbBr$_3$ Nanocrystals Revealed by Atomistic Simulations and Ultrafast Spectroscopy. *Nano Letters*, 20(3):1819–1829, March 2020.

[29] Thomas R. Hopper, Andrei Gorodetsky, Ahhyun Jeong, Franziska Krieg, Maryna I. Bodnarchuk, Marios Maimaris, Marine Chaplain, Thomas J. Macdonald, Xiaokun Huang, Robert Lovrincic, Maksym V. Kovalenko, and Artem A. Bakulin. Hot Carrier Dynamics in Perovskite Nanocrystal Solids: Role of the Cold Carriers, Nanoconfinement, and the Surface. *Nano Letters*, 20(4):2271–2278, April 2020.

[30] Johannes M. Richter, Federico Branchi, Franco Valduga de Almeida Camargo, Baodan Zhao, Richard H. Friend, Giulio Cerullo, and Felix Deschler. Ultrafast carrier thermalization in lead iodide perovskite probed with two-dimensional electronic spectroscopy. *Nature Communications*, 8(1):376, December 2017.

[31] Giovanni Batignani, Giuseppe Fumero, Ajay Ram Srimath Kandada, Giulio Cerullo, Marina Gandini, Carino Ferrante, Annamaria Petrozza, and Tullio Scopigno. Probing femtosecond lattice displacement upon photo-carrier generation in lead halide perovskite. *Nature Communications*, 9(1):1971, December 2018.

[32] Eugenio Cinquanta, Daniele Meggiolaro, Silvia G. Motti, Marina Gandini, Marcelo J. P. Alcocer, Quinten A. Akkerman, Caterina Vozzi, Liberato Manna, Filippo De Angelis, Annamaria Petrozza, and Salvatore Stagira. Ultrafast THz Probe of Photoinduced Polarons in Lead-Halide Perovskites. *Physical Review Letters*, 122(16):166601, April 2019.

[33] Hélène Seiler, Samuel Palato, Colin Sonnichsen, Harry Baker, Etienne Socie, Dallas P. Strandell, and Patanjali Kambhampati. Two-dimensional electronic spectroscopy reveals liquid-like lineshape dynamics in $CsPbI_3$ perovskite nanocrystals. *Nature Communications*, 10(1):4962, December 2019.

[34] Wei Zhao, Zhengyuan Qin, Chunfeng Zhang, Guodong Wang, Xingcan Dai, and Min Xiao. Coherent exciton-phonon coupling in perovskite semiconductor nanocrystals studied by two-dimensional electronic spectroscopy. *Applied Physics Letters*, 115(24):243101, December 2019.

[35] X.-Y. Zhu and V. Podzorov. Charge Carriers in Hybrid Organic–Inorganic Lead Halide Perovskites Might Be Protected as Large Polarons. *The Journal of Physical Chemistry Letters*, 6(23):4758–4761, December 2015.

[36] Peter Yu and Manuel Cardona. *Fundamentals of Semiconductors: Physics and Materials Properties*. Springer Science & Business Media, April 2010.

[37] Julien Ramade, Léon Marcel Andriambariarijaona, Violette Steinmetz, Nicolas Goubet, Laurent Legrand, Thierry Barisien, Frédérick Bernardot, Christophe Testelin, Emmanuel Lhuillier, Alberto Bramati, and Maria Chamarro. Exciton-phonon coupling in a $CsPbBr_3$ single nanocrystal. *Applied Physics Letters*, 112(7):072104, February 2018.

[38] Adam D. Wright, Carla Verdi, Rebecca L. Milot, Giles E. Eperon, Miguel A. Pérez-Osorio, Henry J. Snaith, Feliciano Giustino, Michael B. Johnston, and Laura M. Herz. Electron–phonon coupling in hybrid lead halide perovskites. *Nature Communications*, 7(1):11755, September 2016.

[39] Kaibo Zheng, Mohamed Abdellah, Qiushi Zhu, Qingyu Kong, Guy Jennings, Charles A. Kurtz, Maria E. Messing, Yuran Niu, David J. Gosztola, Mohammed J. Al-Marri, Xiaoyi Zhang, Tönu Pullerits, and Sophie E. Canton. Direct Experimental Evidence for Photoinduced Strong-Coupling Polarons in Organolead Halide Perovskite Nanoparticles. *The Journal of Physical Chemistry Letters*, 7(22):4535–4539, November 2016.

[40] Cunming Liu, Hsinhan Tsai, Wanyi Nie, David J. Gosztola, and Xiaoyi Zhang. Direct Spectroscopic Observation of the Hole Polaron in Lead Halide Perovskites. *The Journal of Physical Chemistry Letters*, 11(15):6256–6261, August 2020.

[41] Xiaoxi Wu, Liang Z. Tan, Xiaozhe Shen, Te Hu, Kiyoshi Miyata, M. Tuan Trinh, Renkai Li, Ryan Coffee, Shi Liu, David A. Egger, Igor Makasyuk, Qiang Zheng, Alan Fry, Joseph S. Robinson, Burak Smith, Matthew D. and, Hemamala I. Karunadasa, Xijie Wang, Xiaoyang Zhu, Leeor Kronik, Andrew M. Rappe, and Aaron M. Lindenberg. Light-induced picosecond rotational disordering of the inorganic sublattice in hybrid perovskites. *Science Advances*, 3(7):e1602388, July 2017.

[42] Burak Guzelturk, Thomas Winkler, Tim W. J. Van de Goor, Matthew D. Smith, Sean A. Bourelle, Sascha Feldmann, Mariano Trigo, Samuel W. Teitelbaum, Hans-Georg Steinrück, Gilberto A. de la Pena, Roberto Alonso-Mori, Diling Zhu, Takahiro Sato, Hemamala I. Karunadasa, Michael F. Toney, Felix Deschler, and Aaron M. Lindenberg. Visualization of dynamic polaronic strain fields in hybrid lead halide perovskites. *Nature Materials*, 20:1–6, January 2021.

[43] Fabio G. Santomauro, Jakob Grilj, Lars Mewes, Georgian Nedelcu, Sergii Yakunin, Thomas Rossi, Gloria Capano, André Al Haddad, James Budarz, Dominik Kinschel, Dario S. Ferreira, Giacomo Rossi, Mario Gutierrez Tovar, Daniel Grolimund, Valerie Samson, Maarten Nachtegaal, Grigory Smolentsev, Maksym V. Kovalenko, and Majed Chergui. Localized holes and delocalized electrons in photoexcited inorganic perovskites: Watching each atomic actor by picosecond X-ray absorption spectroscopy. *Structural Dynamics*, 4(4):044002, December 2016.

[44] M. Puppin, S. Polishchuk, N. Colonna, A. Crepaldi, D. N. Dirin, O. Nazarenko, R. De Gennaro, G. Gatti, S. Roth, T. Barillot, L. Poletto, R. P. Xian, L. Rettig, M. Wolf, R. Ernstorfer, M. V. Kovalenko, N. Marzari, M. Grioni, and M. Chergui. Evidence of Large Polarons in Photoemission Band Mapping of the Perovskite Semiconductor CsPbBr$_3$. *Physical Review Letters*, 124(20):206402, May 2020.

[45] J. J. Rehr and R. C. Albers. Theoretical approaches to x-ray absorption fine structure. *Reviews of Modern Physics*, 72(3):621–654, July 2000.

[46] Boon K. Teo. *EXAFS: Basic Principles and Data Analysis*. Springer Science & Business Media, December 2012.

[47] Majed Chergui and Eric Collet. Photoinduced Structural Dynamics of Molecular Systems Mapped by Time-Resolved X-ray Methods. *Chemical Reviews*, 117(16):11025–11065, August 2017.

[48] Anne Marie March, Andrew Stickrath, Gilles Doumy, Elliot P. Kanter, Bertold Krässig, Stephen H. Southworth, Klaus Attenkofer, Charles A. Kurtz, Lin X. Chen, and Linda Young. Development of high-repetition-rate laser pump/x-ray probe methodologies for synchrotron facilities. *Review of Scientific Instruments*, 82(7):073110, July 2011.

Bibliography

[49] Anne Marie March, Gilles Doumy, Amity Andersen, Andre Al Haddad, Yoshiaki Kumagai, Ming-Feng Tu, Joohee Bang, Christoph Bostedt, Jens Uhlig, Daniel R. Nascimento, Tadesse A. Assefa, Zoltán Németh, György Vankó, Wojciech Gawelda, Niranjan Govind, and Linda Young. Elucidation of the photoaquation reaction mechanism in ferrous hexacyanide using synchrotron x-rays with sub-pulse-duration sensitivity. *The Journal of Chemical Physics*, 151(14):144306, October 2019.

[50] Franziska Krieg, Stefan T. Ochsenbein, Sergii Yakunin, Stephanie ten Brinck, Philipp Aellen, Adrian Süess, Baptiste Clerc, Dominic Guggisberg, Olga Nazarenko, Yevhen Shynkarenko, Sudhir Kumar, Chih-Jen Shih, Ivan Infante, and Maksym V. Kovalenko. Colloidal $CsPbX_3$ (X = Cl, Br, I) Nanocrystals 2.0: Zwitterionic Capping Ligands for Improved Durability and Stability. *ACS Energy Letters*, 3(3):641–646, March 2018.

[51] Paolo Giannozzi, Stefano Baroni, Nicola Bonini, Matteo Calandra, Roberto Car, Carlo Cavazzoni, Davide Ceresoli, Guido L. Chiarotti, Matteo Cococcioni, Ismaila Dabo, Andrea Dal Corso, Stefano de Gironcoli, Stefano Fabris, Guido Fratesi, Ralph Gebauer, Uwe Gerstmann, Christos Gougoussis, Anton Kokalj, Michele Lazzeri, Layla Martin-Samos, Nicola Marzari, Francesco Mauri, Riccardo Mazzarello, Stefano Paolini, Alfredo Pasquarello, Lorenzo Paulatto, Carlo Sbraccia, Sandro Scandolo, Gabriele Sclauzero, Ari P. Seitsonen, Alexander Smogunov, Paolo Umari, and Renata M. Wentzcovitch. QUANTUM ESPRESSO: A modular and open-source software project for quantum simulations of materials. *Journal of Physics: Condensed Matter*, 21(39):395502, September 2009.

[52] P. Giannozzi, O. Andreussi, T. Brumme, O. Bunau, M. Buongiorno Nardelli, M. Calandra, R. Car, C. Cavazzoni, D. Ceresoli, M. Cococcioni, N. Colonna, I. Carnimeo, A. Dal Corso, S. de Gironcoli, P. Delugas, R. A. DiStasio, A. Ferretti, A. Floris, G. Fratesi, G. Fugallo, R. Gebauer, U. Gerstmann, F. Giustino, T. Gorni, J. Jia, M. Kawamura, H.-Y. Ko, A. Kokalj, E. Küçükbenli, M. Lazzeri, M. Marsili, N. Marzari, F. Mauri, N. L. Nguyen, H.-V. Nguyen, A. Otero-de-la-Roza, L. Paulatto, S. Poncé, D. Rocca, R. Sabatini, B. Santra, M. Schlipf, A. P. Seitsonen, A. Smogunov, I. Timrov, T. Thonhauser, P. Umari, N. Vast, X. Wu, and S. Baroni. Advanced capabilities for materials modelling with Quantum ESPRESSO. *Journal of Physics: Condensed Matter*, 29(46):465901, October 2017.

[53] John P. Perdew, Kieron Burke, and Matthias Ernzerhof. Generalized Gradient Approximation Made Simple. *Physical Review Letters*, 77(18):3865–3868, October 1996.

[54] Andrea Dal Corso. Pseudopotentials periodic table: From H to Pu. *Computational Materials Science*, 95:337–350, December 2014.

[55] Christos Gougoussis, Matteo Calandra, Ari P. Seitsonen, and Francesco Mauri. First-principles calculations of x-ray absorption in a scheme based on ultrasoft pseudopotentials: From α-quartz to high-T_c compounds. *Physical Review B*, 80(7):075102, August 2009.

106

[56] Mathieu Taillefumier, Delphine Cabaret, Anne-Marie Flank, and Francesco Mauri. X-ray absorption near-edge structure calculations with the pseudopotentials: Application to the K edge in diamond and α-quartz. *Physical Review B*, 66(19):195107, November 2002.

[57] K. Gilmore, John Vinson, E. L. Shirley, D. Prendergast, C. D. Pemmaraju, J. J. Kas, F. D. Vila, and J. J. Rehr. Efficient implementation of core-excitation Bethe–Salpeter equation calculations. *Computer Physics Communications*, 197:109–117, December 2015.

[58] Benjamin T. Diroll and Richard D. Schaller. Intraband Cooling in All-Inorganic and Hybrid Organic–Inorganic Perovskite Nanocrystals. *Advanced Functional Materials*, 29(37):1901725, 2019.

[59] Yue Wang, Xiaoming Li, Jizhong Song, Lian Xiao, Haibo Zeng, and Handong Sun. All-Inorganic Colloidal Perovskite Quantum Dots: A New Class of Lasing Materials with Favorable Characteristics. *Advanced Materials*, 27(44):7101–7108, November 2015.

[60] Tasnim Ahmed, Sudipta Seth, and Anunay Samanta. Boosting the Photoluminescence of $CsPbX_3$ (X = Cl, Br, I) Perovskite Nanocrystals Covering a Wide Wavelength Range by Post-synthetic Treatment with Tetrafluoroborate Salts. *Chemistry of Materials*, 30(11):3633–3637, June 2018.

[61] Thomas R. Hopper, Andrei Gorodetsky, Jarvist M. Frost, Christian Müller, Robert Lovrincic, and Artem A. Bakulin. Ultrafast Intraband Spectroscopy of Hot-Carrier Cooling in Lead-Halide Perovskites. *ACS Energy Letters*, 3(9):2199–2205, September 2018.

[62] Benjamin T. Diroll and Richard D. Schaller. Heating and cooling of ligand-coated colloidal nanocrystals in solid films and solvent matrices. April 2019.

[63] David Prendergast and Giulia Galli. X-Ray Absorption Spectra of Water from First Principles Calculations. *Physical Review Letters*, 96(21):215502, May 2006.

[64] Shang-Peng Gao, Chris J. Pickard, Mike C. Payne, Jing Zhu, and Jun Yuan. Theory of core-hole effects in 1s core-level spectroscopy of the first-row elements. *Physical Review B*, 77(11):115122, March 2008.

[65] Akihiro Koide, Yohei Uemura, Daiki Kido, Yuki Wakisaka, Satoru Takakusagi, Bunsho Ohtani, Yasuhiro Niwa, Shunsuke Nozawa, Kohei Ichiyanagi, Ryo Fukaya, Shin-ichi Adachi, Tetsuo Katayama, Tadashi Togashi, Shigeki Owada, Makina Yabashi, Yusaku Yamamoto, Misaki Katayama, Keisuke Hatada, Toshihiko Yokoyama, and Kiyotaka Asakura. Photoinduced anisotropic distortion as the electron trapping site of tungsten trioxide by ultrafast W L_1-edge X-ray absorption spectroscopy with full potential multiple scattering calculations. April 2020.

[66] Thomas J. Penfold, Jakub Szlachetko, Fabio G. Santomauro, Alexander Britz, Wojciech Gawelda, Gilles Doumy, Anne Marie March, Stephen H. Southworth, Jochen Rittmann, Rafael Abela, Majed Chergui, and Christopher J. Milne. Revealing hole trapping in zinc

oxide nanoparticles by time-resolved X-ray spectroscopy. *Nature Communications*, 9(1):478, February 2018.

[67] Wee-Liat Ong, Sara M. Rupich, Dmitri V. Talapin, Alan J. H. McGaughey, and Jonathan A. Malen. Surface chemistry mediates thermal transport in three-dimensional nanocrystal arrays. *Nature Materials*, 12(5):410–415, May 2013.

[68] Benjamin T. Diroll, Arun Mannodi-Kanakkithodi, Maria K. Y. Chan, and Richard D. Schaller. Spectroscopic Comparison of Thermal Transport at Organic–Inorganic and Organic-Hybrid Interfaces Using $CsPbBr_3$ and $FAPbBr_3$ (FA = Formamidinium) Perovskite Nanocrystals. *Nano Letters*, 19(11):8155–8160, November 2019.

[69] David T. Limmer and Naomi S. Ginsberg. Photoinduced phase separation in the lead halides is a polaronic effect. *The Journal of Chemical Physics*, 152(23):230901, June 2020.

[70] Cunming Liu, Yingqi Wang, Huifang Geng, Taishan Zhu, Elif Ertekin, David Gosztola, Sizhuo Yang, Jier Huang, Bin Yang, Keli Han, Sophie E. Canton, Qingyu Kong, Kaibo Zheng, and Xiaoyi Zhang. Asynchronous Photoexcited Electronic and Structural Relaxation in Lead-Free Perovskites. *Journal of the American Chemical Society*, 141(33):13074–13080, August 2019.

[71] Takeshi Egami and Simon J. L. Billinge. *Underneath the Bragg Peaks: Structural Analysis of Complex Materials*. Newnes, December 2012.

[72] M. Hannelore Rittmann-Frank, Chris J. Milne, Jochen Rittmann, Marco Reinhard, Thomas J. Penfold, and Majed Chergui. Mapping of the Photoinduced Electron Traps in TiO_2 by Picosecond X-ray Absorption Spectroscopy. *Angewandte Chemie International Edition*, 53(23):5858–5862, June 2014.

[73] Joseph Puthenpurayil, Oscar Hsu-Cheng Cheng, Tian Qiao, Daniel Rossi, and Dong Hee Son. On the determination of absorption cross section of colloidal lead halide perovskite quantum dots. *The Journal of Chemical Physics*, 151(15):154706, October 2019.

[74] Oana Bunău and Matteo Calandra. Projector augmented wave calculation of x-ray absorption spectra at the $L_{2,3}$. *Physical Review B*, 87(20):205105, May 2013.

[75] Y. P. Varshni. Temperature dependence of the energy gap in semiconductors. *Physica*, 34(1):149–154, January 1967.

[76] Benjamin T. Diroll, Georgian Nedelcu, Maksym V. Kovalenko, and Richard D. Schaller. High-Temperature Photoluminescence of $CsPbX_3$ (X = Cl, Br, I) Nanocrystals. *Advanced Functional Materials*, 27(21):1606750, March 2017.

[77] Giselle A. Elbaz, Wee-Liat Ong, Evan A. Doud, Philip Kim, Daniel W. Paley, Xavier Roy, and Jonathan A. Malen. Phonon Speed, Not Scattering, Differentiates Thermal Transport in Lead Halide Perovskites. *Nano Letters*, 17(9):5734–5739, September 2017.

[78] Tobias Haeger, Maximilian Wilmes, Ralf Heiderhoff, and Thomas Riedl. Simultaneous Mapping of Thermal Conductivity, Thermal Diffusivity, and Volumetric Heat Capacity of Halide Perovskite Thin Films: A Novel Nanoscopic Thermal Measurement Technique. *The Journal of Physical Chemistry Letters*, 10(11):3019–3023, June 2019.

[79] Taame Abraha Berhe, Wei-Nien Su, Ching-Hsiang Chen, Chun-Jern Pan, Ju-Hsiang Cheng, Hung-Ming Chen, Meng-Che Tsai, Liang-Yih Chen, Amare Aregahegn Dubale, and Bing-Joe Hwang. Organometal halide perovskite solar cells: Degradation and stability. *Energy & Environmental Science*, 9(2):323–356, October 2016.

[80] Juan-Pablo Correa-Baena, Michael Saliba, Tonio Buonassisi, Michael Grätzel, Antonio Abate, Wolfgang Tress, and Anders Hagfeldt. Promises and challenges of perovskite solar cells. *Science*, 358(6364):739–744, November 2017.

[81] Pabitra K. Nayak, Suhas Mahesh, Henry J. Snaith, and David Cahen. Photovoltaic solar cell technologies: Analysing the state of the art. *Nature Reviews Materials*, 4(4):269–285, April 2019.

[82] Tomas Leijtens, Giles E. Eperon, Sandeep Pathak, Antonio Abate, Michael M. Lee, and Henry J. Snaith. Overcoming ultraviolet light instability of sensitized TiO_2 with meso-superstructured organometal tri-halide perovskite solar cells. *Nature Communications*, 4(1):2885, December 2013.

[83] Adam H. Slavney, Rebecca W. Smaha, Ian C. Smith, Adam Jaffe, Daiki Umeyama, and Hemamala I. Karunadasa. Chemical Approaches to Addressing the Instability and Toxicity of Lead–Halide Perovskite Absorbers. *Inorganic Chemistry*, 56(1):46–55, January 2017.

[84] Dian Wang, Matthew Wright, Naveen Kumar Elumalai, and Ashraf Uddin. Stability of perovskite solar cells. *Solar Energy Materials and Solar Cells*, 147:255–275, April 2016.

[85] Connor G. Bischak, Craig L. Hetherington, Hao Wu, Shaul Aloni, D. Frank Ogletree, David T. Limmer, and Naomi S. Ginsberg. Origin of Reversible Photoinduced Phase Separation in Hybrid Perovskites. *Nano Letters*, 17(2):1028–1033, February 2017.

[86] Samuel D. Stranks and Henry J. Snaith. Metal-halide perovskites for photovoltaic and light-emitting devices. *Nature Nanotechnology*, 10(5):391–402, May 2015.

[87] Shunsuke Hirotsu, Jimpei Harada, Masashi Iizumi, and Kazuo Gesi. Structural Phase Transitions in $CsPbBr_3$. *Journal of the Physical Society of Japan*, 37(5):1393–1398, November 1974.

[88] A. M. Glazer. Simple ways of determining perovskite structures. *Acta Crystallographica Section A*, 31(6):756–762, May 1975.

[89] Christian Kn Møller. The structure of perovskite-like caesium plumbo trihalides. *Mat. Fys. Medd Danske Vidensk Selsk.*, 32(2), 1959.

[90] Patrick Cottingham and Richard L. Brutchey. On the crystal structure of colloidally prepared $CsPbBr_3$ quantum dots. *Chemical Communications*, 52(30):5246–5249, March 2016.

[91] Oliviero Cannelli, Nicola Colonna, Michele Puppin, Thomas Rossi, Dominik Kinschel, Ludmila Leroy, Janina Loeffler, Anne Marie March, Gilles Doumy, Andre Al Haddad, Ming-Feng Tu, Yoshiaki Kumagai, Donald Walko, Grigory Smolentsev, Franziska Krieg, Simon C. Boehme, Maksym V. Kovalenko, Majed Chergui, and Giulia F. Mancini. Quantifying Photoinduced Polaronic Distortions in Inorganic Lead Halide Perovskites Nanocrystals. *arXiv:2103.02575 [cond-mat]*, March 2021.

[92] Yi Yu, Dandan Zhang, Christian Kisielowski, Letian Dou, Nikolay Kornienko, Yehonadav Bekenstein, Andrew B. Wong, A. Paul Alivisatos, and Peidong Yang. Atomic Resolution Imaging of Halide Perovskites. *Nano Letters*, 16(12):7530–7535, December 2016.

[93] Joost VandeVondele, Matthias Krack, Fawzi Mohamed, Michele Parrinello, Thomas Chassaing, and Jürg Hutter. Quickstep: Fast and accurate density functional calculations using a mixed Gaussian and plane waves approach. *Computer Physics Communications*, 167(2):103–128, April 2005.

[94] Ruidy Nemausat, Christel Gervais, Christian Brouder, Nicolas Trcera, Amélie Bordage, Cristina Coelho-Diogo, Pierre Florian, Aydar Rakhmatullin, Ion Errea, Lorenzo Paulatto, Michele Lazzeri, and Delphine Cabaret. Temperature dependence of X-ray absorption and nuclear magnetic resonance spectra: Probing quantum vibrations of light elements in oxides. *Physical Chemistry Chemical Physics*, 19(8):6246–6256, January 2017.

[95] Ruidy Nemausat, Delphine Cabaret, Christel Gervais, Christian Brouder, Nicolas Trcera, Amélie Bordage, Ion Errea, and Francesco Mauri. Phonon effects on x-ray absorption and nuclear magnetic resonance spectroscopies. *Physical Review B*, 92(14):144310, October 2015.

[96] M. Rodová, J. Brožek, K. Knížek, and K. Nitsch. Phase transitions in ternary caesium lead bromide. *Journal of Thermal Analysis and Calorimetry*, 71(2):667–673, February 2003.

[97] Shunsuke Hirotsu, Tomonobu Suzuki, and Shozo Sawada. Ultrasonic Velocity around the Successive Phase Transition Points of $CsPbBr_3$. *Journal of the Physical Society of Japan*, 43(2):575–582, August 1977.

[98] Jonathon S. Bechtel, John C. Thomas, and Anton Van der Ven. Finite-temperature simulation of anharmonicity and octahedral tilting transitions in halide perovskites. *Physical Review Materials*, 3(11):113605, November 2019.

[99] Ruo Xi Yang and Jonathan M Skelton. Spontaneous Octahedral Tilting in the Cubic Inorganic Cesium Halide Perovskites $CsSnX_3$ and $CsPbX_3$ (X = F, Cl, Br, I). *J. Phys. Chem. Lett.*, 8:4720–4726, September 2017.

[100] G. Shirane. Neutron scattering studies of structural phase transitions at Brookhaven. *Reviews of Modern Physics*, 46(3):437–449, July 1974.

[101] I. P. Swainson, C. Stock, S. F. Parker, L. Van Eijck, M. Russina, and J. W. Taylor. From soft harmonic phonons to fast relaxational dynamics in $CH_3NH_3PbBr_3$. *Physical Review B*, 92(10):100303, September 2015.

[102] John B. Goodenough. Perspective on Engineering Transition-Metal Oxides. *Chemistry of Materials*, 26(1):820–829, January 2014.

[103] Anthony Harriman, Ingrid J. Pickering, John M. Thomas, and Paul A. Christensen. Metal oxides as heterogeneous catalysts for oxygen evolution under photochemical conditions. *Journal of the Chemical Society, Faraday Transactions 1: Physical Chemistry in Condensed Phases*, 84(8):2795–2806, January 1988.

[104] Amy L. Linsebigler, Guangquan Lu, and John T. Yates. Photocatalysis on TiO_2 Surfaces: Principles, Mechanisms, and Selected Results. *Chemical Reviews*, 95(3):735–758, May 1995.

[105] Kevin Sivula and Roel van de Krol. Semiconducting materials for photoelectrochemical energy conversion. *Nature Reviews Materials*, 1(2):15010, February 2016.

[106] Xiaowei Xie, Yong Li, Zhi-Quan Liu, Masatake Haruta, and Wenjie Shen. Low-temperature oxidation of CO catalysed by Co_3O_4 nanorods. *Nature*, 458(7239):746–749, April 2009.

[107] Feng Jiao and Heinz Frei. Nanostructured Cobalt Oxide Clusters in Mesoporous Silica as Efficient Oxygen-Evolving Catalysts. February 2009.

[108] Yongye Liang, Yanguang Li, Hailiang Wang, Jigang Zhou, Jian Wang, Tom Regier, and Hongjie Dai. Co_3O_4 nanocrystals on graphene as a synergistic catalyst for oxygen reduction reaction. *Nature Materials*, 10(10):780–786, October 2011.

[109] W. L. Roth. The magnetic structure of Co_3O_4. *Journal of Physics and Chemistry of Solids*, 25(1):1–10, January 1964.

[110] Jia Chen, Xifan Wu, and Annabella Selloni. Electronic structure and bonding properties of cobalt oxide in the spinel structure. *Physical Review B*, 83(24):245204, June 2011.

[111] Kwang Joo Kim and Young Ran Park. Optical investigation of charge-transfer transitions in spinel Co_3O_4. *Solid State Communications*, 127(1):25–28, June 2003.

[112] K. M. E. Miedzinska, B. R. Hollebone, and J. G. Cook. An assigment of the optical absorption spectrum of mixed valence Co_3O_4 spinel films. *Journal of Physics and Chemistry of Solids*, 48(7):649–656, January 1987.

[113] L. Qiao, H. Y. Xiao, H. M. Meyer, J. N. Sun, C. M. Rouleau, A. A. Puretzky, D. B. Geohegan, I. N. Ivanov, M. Yoon, W. J. Weber, and M. D. Biegalski. Nature of the band gap and origin of the electro-/photo-activity of Co_3O_4. *Journal of Materials Chemistry C*, 1(31):4628–4633, July 2013.

[114] Chang-Ming Jiang, L. Robert Baker, J. Matthew Lucas, Josh Vura-Weis, A. Paul Alivisatos, and Stephen R. Leone. Characterization of Photo-Induced Charge Transfer and Hot Carrier Relaxation Pathways in Spinel Cobalt Oxide (Co_3O_4). *The Journal of Physical Chemistry C*, 118(39):22774–22784, October 2014.

[115] Somnath Biswas, Jakub Husek, and L. Robert Baker. Elucidating ultrafast electron dynamics at surfaces using extreme ultraviolet (XUV) reflection–absorption spectroscopy. *Chemical Communications*, 54(34):4216–4230, April 2018.

[116] L. Robert Baker, Chang-Ming Jiang, Stephen T. Kelly, J. Matthew Lucas, Josh Vura-Weis, Mary K. Gilles, A. Paul Alivisatos, and Stephen R. Leone. Charge Carrier Dynamics of Photoexcited Co_3O_4 in Methanol: Extending High Harmonic Transient Absorption Spectroscopy to Liquid Environments. *Nano Letters*, 14(10):5883–5890, October 2014.

[117] B. L. Henke, E. M. Gullikson, and J. C. Davis. X-Ray Interactions: Photoabsorption, Scattering, Transmission, and Reflection at E = 50-30,000 eV, Z = 1-92. *Atomic Data and Nuclear Data Tables*, 54(2):181–342, July 1993.

[118] R. Dietsch, Th. Holz, H. Mai, M. Panzner, and S. Völlmar. Pulsed laser deposition (PLD) — an advanced state for technical applications. *Optical and Quantum Electronics*, 27(12):1385–1396, December 1995.

[119] V G Hadjiev, M N Iliev, and I V Vergilov. The Raman spectra of Co_3O_4. *Journal of Physics C: Solid State Physics*, 21(7):L199–L201, March 1988.

[120] Alyssa Mock, Rafał Korlacki, Chad Briley, Derek Sekora, Tino Hofmann, Peter Wilson, Alexander Sinitskii, Eva Schubert, and Mathias Schubert. Anisotropy, band-to-band transitions, phonon modes, and oxidation properties of cobalt-oxide core-shell slanted columnar thin films. *Applied Physics Letters*, 108(5):051905, February 2016.

[121] T. Yu, Y. W. Zhu, X. J. Xu, Z. X. Shen, P. Chen, C.-T. Lim, J. T.-L. Thong, and C.-H. Sow. Controlled Growth and Field-Emission Properties of Cobalt Oxide Nanowalls. *Advanced Materials*, 17(13):1595–1599, July 2005.

[122] W. B. White and B. A. DeAngelis. Interpretation of the vibrational spectra of spinels. *Spectrochimica Acta Part A: Molecular Spectroscopy*, 23(4):985–995, April 1967.

[123] D. C. Koningsberger and R. Prins. X-ray absorption: Principles, applications, techniques of EXAFS, SEXAFS, and XANES. 1988.

[124] H Hedayat, C J Sayers, A Ceraso, J van Wezel, S R Clark, C Dallera, G Cerullo, E Da Como, and E Carpene. Investigation of the non-equilibrium state of strongly correlated materials by complementary ultrafast spectroscopy techniques. *New Journal of Physics*, 23(3):033025, March 2021.

[125] H. J. Zeiger, J. Vidal, T. K. Cheng, E. P. Ippen, G. Dresselhaus, and M. S. Dresselhaus. Theory for displacive excitation of coherent phonons. *Physical Review B*, 45(2):768–778, January 1992.

[126] R. R. Alfano and S. L. Shapiro. Optical Phonon Lifetime Measured Directly with Picosecond Pulses. *Physical Review Letters*, 26(20):1247–1251, May 1971.

[127] E. Baldini, A. Mann, L. Benfatto, E. Cappelluti, A. Acocella, V. M. Silkin, S. V. Eremeev, A. B. Kuzmenko, S. Borroni, T. Tan, X. X. Xi, F. Zerbetto, R. Merlin, and F. Carbone. Real-time observation of phonon-mediated σ-π interband scattering in MgB_2. *Physical Review Letters*, 119(9):097002, August 2017.

[128] S. Borroni, E. Baldini, V. M. Katukuri, A. Mann, K. Parlinski, D. Legut, C. Arrell, F. van Mourik, J. Teyssier, A. Kozlowski, P. Piekarz, O. V. Yazyev, A. M. Oleś, J. Lorenzana, and F. Carbone. Coherent generation of symmetry-forbidden phonons by light-induced electron-phonon interactions in magnetite. *Physical Review B*, 96(10):104308, September 2017.

[129] M. F. DeCamp, D. A. Reis, P. H. Bucksbaum, and R. Merlin. Dynamics and coherent control of high-amplitude optical phonons in bismuth. *Physical Review B*, 64(9):092301, August 2001.

[130] T. E. Stevens, J. Kuhl, and R. Merlin. Coherent phonon generation and the two stimulated Raman tensors. *Physical Review B*, 65(14):144304, March 2002.

[131] Jagdeep Shah. *Ultrafast Spectroscopy of Semiconductors and Semiconductor Nanostructures.* Springer Science & Business Media, November 2013.

[132] Peter T Landsberg. *Recombination in semiconductors.* Cambridge University Press, 2003.

[133] G. C. Cho, W. Kütt, and H. Kurz. Subpicosecond time-resolved coherent-phonon oscillations in GaAs. *Physical Review Letters*, 65(6):764–766, August 1990.

[134] Lisa Dhar, John A. Rogers, and Keith A. Nelson. Time-resolved vibrational spectroscopy in the impulsive limit. *Chemical Reviews*, 94(1):157–193, January 1994.

[135] R. Merlin. Generating coherent THz phonons with light pulses. *Solid State Communications*, 102(2):207–220, April 1997.

[136] Gerald Auböck, Cristina Consani, Roberto Monni, Andrea Cannizzo, Frank van Mourik, and Majed Chergui. Femtosecond pump/supercontinuum-probe setup with 20 kHz repetition rate. *Review of Scientific Instruments*, 83(9):093105, September 2012.

[137] Edoardo Baldini, Andreas Mann, Simone Borroni, Christopher Arrell, Frank van Mourik, and Fabrizio Carbone. A versatile setup for ultrafast broadband optical spectroscopy of coherent collective modes in strongly correlated quantum systems. *Structural Dynamics*, 3(6):064301, November 2016.

[138] Chavdar Slavov, Helvi Hartmann, and Josef Wachtveitl. Implementation and Evaluation of Data Analysis Strategies for Time-Resolved Optical Spectroscopy. *Analytical Chemistry*, 87(4):2328–2336, February 2015.

[139] Ivo H. M. van Stokkum, Delmar S. Larsen, and Rienk van Grondelle. Global and target analysis of time-resolved spectra. *Biochimica et Biophysica Acta (BBA) - Bioenergetics*, 1657(2):82–104, July 2004.

[140] Robert D. Cowan. *The Theory of Atomic Structure and Spectra*. University of California Press, September 1981.

[141] Pieter Glatzel and Uwe Bergmann. High resolution 1s core hole X-ray spectroscopy in 3d transition metal complexes—electronic and structural information. *Coordination Chemistry Reviews*, 249(1):65–95, January 2005.

[142] Camila Bacellar, Dominik Kinschel, Giulia F. Mancini, Rebecca A. Ingle, Jérémy Rouxel, Oliviero Cannelli, Claudio Cirelli, Gregor Knopp, Jakub Szlachetko, Frederico A. Lima, Samuel Menzi, Georgios Pamfilidis, Katharina Kubicek, Dmitry Khakhulin, Wojciech Gawelda, Angel Rodriguez-Fernandez, Mykola Biednov, Christian Bressler, Christopher A. Arrell, Philip J. M. Johnson, Christopher J. Milne, and Majed Chergui. Spin cascade and doming in ferric hemes: Femtosecond X-ray absorption and X-ray emission studies. *Proceedings of the National Academy of Sciences*, 117(36):21914–21920, September 2020.

[143] Dominik Kinschel, Camila Bacellar, Oliviero Cannelli, Boris Sorokin, Tetsuo Katayama, Giulia F. Mancini, Jérémy R. Rouxel, Yuki Obara, Junichi Nishitani, Hironori Ito, Terumasa Ito, Naoya Kurahashi, Chika Higashimura, Shotaro Kudo, Theo Keane, Frederico A. Lima, Wojciech Gawelda, Peter Zalden, Sebastian Schulz, James M. Budarz, Dmitry Khakhulin, Andreas Galler, Christian Bressler, Christopher J. Milne, Thomas Penfold, Makina Yabashi, Toshinori Suzuki, Kazuhiko Misawa, and Majed Chergui. Femtosecond X-ray emission study of the spin cross-over dynamics in haem proteins. *Nature Communications*, 11(1):4145, August 2020.

[144] Michael W. Mara, Ryan G. Hadt, Marco Eli Reinhard, Thomas Kroll, Hyeongtaek Lim, Robert W. Hartsock, Roberto Alonso-Mori, Matthieu Chollet, James M. Glownia, Silke Nelson, Dimosthenis Sokaras, Kristjan Kunnus, Keith O. Hodgson, Britt Hedman, Uwe Bergmann, Kelly J. Gaffney, and Edward I. Solomon. Metalloprotein entatic control of ligand-metal bonds quantified by ultrafast x-ray spectroscopy. *Science*, 356(6344):1276–1280, June 2017.

[145] Wenkai Zhang, Roberto Alonso-Mori, Uwe Bergmann, Christian Bressler, Matthieu Chollet, Andreas Galler, Wojciech Gawelda, Ryan G. Hadt, Robert W. Hartsock, Thomas Kroll, Kasper S. Kjær, Katharina Kubiček, Henrik T. Lemke, Huiyang W. Liang, Drew A. Meyer, Martin M. Nielsen, Carola Purser, Joseph S. Robinson, Edward I. Solomon, Zheng Sun, Dimosthenis Sokaras, Tim B. van Driel, György Vankó, Tsu-Chien Weng, Diling Zhu, and Kelly J. Gaffney. Tracking excited-state charge and spin dynamics in iron coordination complexes. *Nature*, 509(7500):345–348, May 2014.

[146] Frederico A. Lima, Christopher J. Milne, Dimali CV Amarasinghe, Mercedes Hannelore Rittmann-Frank, Renske M. van der Veen, Marco Reinhard, Van-Thai Pham, Susanne Karlsson, Steven L. Johnson, and Daniel Grolimund. A high-repetition rate scheme for synchrotron-based picosecond laser pump/x-ray probe experiments on chemical and biological systems in solution. *Review of Scientific Instruments*, 82(6):063111, June 2011.

[147] A. Galler, W. Gawelda, M. Biednov, C. Bomer, A. Britz, S. Brockhauser, T.-K. Choi, M. Diez, P. Frankenberger, M. French, D. Görries, M. Hart, S. Hauf, D. Khakhulin, M. Knoll, T. Korsch, K. Kubicek, M. Kuster, P. Lang, F. Alves Lima, F. Otte, S. Schulz, P. Zalden, and C. Bressler. Scientific instrument Femtosecond X-ray Experiments (FXE): Instrumentation and baseline experimental capabilities. *Journal of Synchrotron Radiation*, 26(5):1432–1447, September 2019.

[148] A. Mozzanica, M. Andrä, R. Barten, A. Bergamaschi, S. Chiriotti, M. Brückner, R. Dinapoli, E. Fröjdh, D. Greiffenberg, F. Leonarski, C. Lopez-Cuenca, D. Mezza, S. Redford, C. Ruder, B. Schmitt, X. Shi, D. Thattil, G. Tinti, S. Vetter, and J. Zhang. The JUNGFRAU Detector for Applications at Synchrotron Light Sources and XFELs. *Synchrotron Radiation News*, 31(6):16–20, November 2018.

[149] G. Palmer, M. Kellert, J. Wang, M. Emons, U. Wegner, D. Kane, F. Pallas, T. Jezynski, S. Venkatesan, D. Rompotis, E. Brambrink, B. Monoszlai, M. Jiang, J. Meier, K. Kruse, M. Pergament, and M. J. Lederer. Pump–probe laser system at the FXE and SPB/SFX instruments of the European X-ray Free-Electron Laser Facility. *Journal of Synchrotron Radiation*, 26(2):328–332, March 2019.

[150] M. Altarelli. The European X-ray free-electron laser facility in Hamburg. *Nuclear Instruments and Methods in Physics Research Section B: Beam Interactions with Materials and Atoms*, 269(24):2845–2849, December 2011.

[151] Dmitry Khakhulin, Florian Otte, Mykola Biednov, Christina Bömer, Tae-Kyu Choi, Michael Diez, Andreas Galler, Yifeng Jiang, Katharina Kubicek, Frederico Alves Lima, Angel Rodriguez-Fernandez, Peter Zalden, Wojciech Gawelda, and Christian Bressler. Ultrafast X-ray Photochemistry at European XFEL: Capabilities of the Femtosecond X-ray Experiments (FXE) Instrument. *Applied Sciences*, 10(3):995, January 2020.

[152] M. Liebel, C. Schnedermann, T. Wende, and P. Kukura. Principles and Applications of Broadband Impulsive Vibrational Spectroscopy. *The Journal of Physical Chemistry A*, 119(36):9506–9517, September 2015.

Bibliography

[153] F.J. Harris. On the use of windows for harmonic analysis with the discrete Fourier transform. *Proceedings of the IEEE*, 66(1):51–83, January 1978.

[154] O. Matsuda, O. B. Wright, D. H. Hurley, V. E. Gusev, and K. Shimizu. Coherent Shear Phonon Generation and Detection with Ultrashort Optical Pulses. *Physical Review Letters*, 93(9):095501, August 2004.

[155] Pascal Ruello and Vitalyi E. Gusev. Physical mechanisms of coherent acoustic phonons generation by ultrafast laser action. *Ultrasonics*, 56:21–35, February 2015.

[156] C. Thomsen, J. Strait, Z. Vardeny, H. J. Maris, J. Tauc, and J. J. Hauser. Coherent Phonon Generation and Detection by Picosecond Light Pulses. *Physical Review Letters*, 53(10):989–992, September 1984.

[157] Gerald Auböck and Majed Chergui. Sub-50-fs photoinduced spin crossover in $[Fe(bpy)_3]^{2+}$. *Nature Chemistry*, 7(8):629–633, August 2015.

[158] Ch. Bressler, C. Milne, V.-T. Pham, A. ElNahhas, R. M. van der Veen, W. Gawelda, S. Johnson, P. Beaud, D. Grolimund, M. Kaiser, C. N. Borca, G. Ingold, R. Abela, and M. Chergui. Femtosecond XANES Study of the Light-Induced Spin Crossover Dynamics in an Iron(II) Complex. *Science*, 323(5913):489–492, January 2009.

[159] Andrea Cannizzo, Ana Maria Blanco-Rodríguez, Amal El Nahhas, Jakub Šebera, Stanislav Záliš, Antonín Vlček, and Majed Chergui. Femtosecond Fluorescence and Intersystem Crossing in Rhenium(I) Carbonyl-Bipyridine Complexes. *Journal of the American Chemical Society*, 130(28):8967–8974, July 2008.

[160] Wojciech Gawelda, Andrea Cannizzo, Van-Thai Pham, Frank van Mourik, Christian Bressler, and Majed Chergui. Ultrafast Nonadiabatic Dynamics of $[Fe^{II}(bpy)_3]^{2+}$ in Solution. *Journal of the American Chemical Society*, 129(26):8199–8206, July 2007.

[161] J. Zaanen, G. A. Sawatzky, and J. W. Allen. Band gaps and electronic structure of transition-metal compounds. *Physical Review Letters*, 55(4):418–421, July 1985.

[162] Eric V Anslyn and Dennis A Dougherty. *Modern physical organic chemistry*. University science books, 2006.

[163] Ahmed H. Zewail. Femtochemistry: Atomic-Scale Dynamics of the Chemical Bond Using Ultrafast Lasers (Nobel Lecture). *Angewandte Chemie International Edition*, 39(15):2586–2631, August 2000.

[164] Majed Chergui and Ahmed H. Zewail. Electron and X-Ray Methods of Ultrafast Structural Dynamics: Advances and Applications. *ChemPhysChem*, 10(1):28–43, January 2009.

[165] Manfred Eigen. Immeasurably fast reactions. *Nobel Lecture*, 11:1963–1979, 1967.

[166] W. J. Gettins and Evan Wyn-Jones. *Techniques and Applications of Fast Reactions in Solution: Proceedings of the NATO Advanced Study Institute on New Applications of Chemical Relaxation Spectrometry and Other Fast Reaction Methods in Solution, Held at the University College of Wales, Aberystwyth, September 10–20, 1978*, volume 50. Springer Science & Business Media, 2012.

[167] R. M. Ballew, J. Sabelko, C. Reiner, and M. Gruebele. A single-sweep, nanosecond time resolution laser temperature-jump apparatus. *Review of Scientific Instruments*, 67(10):3694–3699, October 1996.

[168] Omar F. Mohammed, Peter C. Samartzis, and Ahmed H. Zewail. Heating and Cooling Dynamics of Carbon Nanotubes Observed by Temperature-Jump Spectroscopy and Electron Microscopy. *Journal of the American Chemical Society*, 131(44):16010–16011, November 2009.

[169] Robert Callender and R. Brian Dyer. Probing protein dynamics using temperature jump relaxation spectroscopy. *Current Opinion in Structural Biology*, 12(5):628–633, October 2002.

[170] Martin Gruebele, Jobiah Sabelko, Richard Ballew, and John Ervin. Laser Temperature Jump Induced Protein Refolding. *Accounts of Chemical Research*, 31(11):699–707, November 1998.

[171] Deyong Li, Yunliang Li, Hao Li, Xianyou Wu, Qingxu Yu, and Yuxiang Weng. A Q-switched Ho:YAG laser assisted nanosecond time-resolved T-jump transient mid-IR absorbance spectroscopy with high sensitivity. *Review of Scientific Instruments*, 86(5):053105, May 2015.

[172] Satoshi Ashihara, Nils Huse, Agathe Espagne, Erik T. J. Nibbering, and Thomas Elsaesser. Ultrafast structural dynamics of water induced by dissipation of vibrational energy. *The Journal of Physical Chemistry A*, 111(5):743–746, February 2007.

[173] Zhaohui Wang, Yoonsoo Pang, and Dana D. Dlott. Hydrogen-Bond Disruption by Vibrational Excitations in Water. *The Journal of Physical Chemistry A*, 111(17):3196–3208, May 2007.

[174] Hairong Ma, Chaozhi Wan, Aiguo Wu, and Ahmed H. Zewail. DNA folding and melting observed in real time redefine the energy landscape. *Proceedings of the National Academy of Sciences*, 104(3):712–716, January 2007.

[175] Hairong Ma, Chaozhi Wan, and Ahmed H. Zewail. Ultrafast T-Jump in Water: Studies of Conformation and Reaction Dynamics at the Thermal Limit. *Journal of the American Chemical Society*, 128(19):6338–6340, May 2006.

[176] Christian Bressler, Rafael Abela, and Majed Chergui. Exploiting EXAFS and XANES for time-resolved molecular structures in liquids. *Zeitschrift für Kristallographie*, 223(4-5/2008), January 2008.

Bibliography

[177] M. Chergui. Picosecond and femtosecond X-ray absorption spectroscopy of molecular systems. *Acta Crystallographica Section A*, 66(2):229–239, March 2010.

[178] Majed Chergui. Emerging photon technologies for chemical dynamics. *Faraday Discussions*, 171(0):11–40, August 2014.

[179] Majed Chergui and Eric Collet. Photoinduced Structural Dynamics of Molecular Systems Mapped by Time-Resolved X-ray Methods. *Chemical Reviews*, 117(16):11025–11065, August 2017.

[180] Bernd Winter and Manfred Faubel. Photoemission from Liquid Aqueous Solutions. *Chemical Reviews*, 106(4):1176–1211, April 2006.

[181] G. Gavrila, K. Godehusen, C. Weniger, E. T. J. Nibbering, T. Elsaesser, W. Eberhardt, and P. Wernet. Time-resolved X-ray absorption spectroscopy of infrared-laser-induced temperature jumps in liquid water. *Applied Physics A*, 96(1):11–18, July 2009.

[182] Dolev Rimmerman, Denis Leshchev, Darren J. Hsu, Jiyun Hong, Irina Kosheleva, and Lin X. Chen. Direct Observation of Insulin Association Dynamics with Time-Resolved X-ray Scattering. *The Journal of Physical Chemistry Letters*, 8(18):4413–4418, September 2017.

[183] Dolev Rimmerman, Denis Leshchev, Darren J. Hsu, Jiyun Hong, Baxter Abraham, Irina Kosheleva, Robert Henning, and Lin X. Chen. Insulin hexamer dissociation dynamics revealed by photoinduced T-jumps and time-resolved X-ray solution scattering. *Photochemical & Photobiological Sciences*, 17(7):874–882, July 2018.

[184] Hyun Sun Cho, Friedrich Schotte, Valentyn Stadnytskyi, Anthony DiChiara, Robert Henning, and Philip Anfinrud. Dynamics of Quaternary Structure Transitions in R-State Carbonmonoxyhemoglobin Unveiled in Time-Resolved X-ray Scattering Patterns Following a Temperature Jump. *The Journal of Physical Chemistry B*, 122(49):11488–11496, December 2018.

[185] Michael C. Thompson, Benjamin A. Barad, Alexander M. Wolff, Hyun Sun Cho, Friedrich Schotte, Daniel M. C. Schwarz, Philip Anfinrud, and James S. Fraser. Temperature-jump solution X-ray scattering reveals distinct motions in a dynamic enzyme. *Nature Chemistry*, 11(11):1058–1066, November 2019.

[186] Pujing Pan and Nicholas J Susak. Co(II)-chloride and -bromide complexes in aqueous solutions up to 5 m NaX and 90°C: Spectrophotometric study and geological implications. *Geochimica et Cosmochimica Acta*, 53(2):327–341, February 1989.

[187] Hairong Ma, Chaozhi Wan, and Ahmed H. Zewail. Dynamics of ligand substitution in labile cobalt complexes resolved by ultrafast T-jump. *Proceedings of the National Academy of Sciences*, 105(35):12754–12757, September 2008.

118

[188] Kenji Waizumi, Takahisa Kouda, Atsuhiro Tanio, Nobuhiro Fukushima, and Hitoshi Ohtaki. Structural Studies on Saturated Aqueous Solutions of Manganese(II), Cobalt(II), and Nickel(II) Chlorides by X-ray Diffraction. *Journal of Solution Chemistry*, 28(2):83–100, February 1999.

[189] S. F. Levochkin, P. R. Smirnov, and V. N. Trostin. D-Structure of Aqueous Solutions of Cobalt(II) Nitrate at 298 and 323 K by X-Ray Diffraction. *Russian Journal of General Chemistry*, 75(8):1180–1185, August 2005.

[190] Owen G. Holmes and Donald S. McClure. Optical Spectra of Hydrated Ions of the Transition Metals. *The Journal of Chemical Physics*, 26(6):1686–1694, June 1957.

[191] Masahito Uchikoshi. Determination of the Distribution of Cobalt-Chloro Complexes in Hydrochloric Acid Solutions at 298 K. *Journal of Solution Chemistry*, 47(12):2021–2038, December 2018.

[192] Masahito Uchikoshi and Kozo Shinoda. Determination of structures of cobalt(II)-chloro complexes in hydrochloric acid solutions by X-ray absorption spectroscopy at 298 K. *Structural Chemistry*, 30(3):945–954, June 2019.

[193] José Ojeda, Christopher A. Arrell, Luca Longetti, Majed Chergui, and Jan Helbing. Charge-transfer and impulsive electronic-to-vibrational energy conversion in ferricyanide: Ultrafast photoelectron and transient infrared studies. *Physical Chemistry Chemical Physics*, 19(26):17052–17062, June 2017.

[194] Fabian Rupp, Katharina Chevalier, Michèle Graf, Markus Schmitz, Harald Kelm, Anneken Grün, Manuel Zimmer, Markus Gerhards, Christoph van Wüllen, Hans-Jörg Krüger, and Rolf Diller. Spectroscopic, Structural, and Kinetic Investigation of the Ultrafast Spin Crossover in an Unusual Cobalt(II) Semiquinonate Radical Complex. *Chemistry – A European Journal*, 23(9):2119–2132, November 2017.

[195] Luisa Ferrari, Mauro Satta, Amedeo Palma, Lorenzo Di Mario, Daniele Catone, Patrick O'Keeffe, Nicola Zema, Tommaso Prosperi, and Stefano Turchini. A Fast Transient Absorption Study of Co(AcAc$_3$). *Frontiers in Chemistry*, 7, May 2019.

[196] Marco Reinhard, Gerald Auböck, Nicholas A. Besley, Ian P. Clark, Gregory M. Greetham, Magnus W. D. Hanson-Heine, Raphael Horvath, Thomas S. Murphy, Thomas J. Penfold, Michael Towrie, Michael W. George, and Majed Chergui. Photoaquation Mechanism of Hexacyanoferrate(II) Ions: Ultrafast 2D UV and Transient Visible and IR Spectroscopies. *Journal of the American Chemical Society*, 139(21):7335–7347, May 2017.

[197] Alan G. Joly and Keith A. Nelson. Metal carbonyl photochemistry in organic solvents: Femtosecond transient absorption and preliminary resonance Raman spectroscopy. *Chemical Physics*, 152(1):69–82, April 1991.

Bibliography

[198] Yao Liu, David B. Turner, Tanya N. Singh, Alfredo M. Angeles-Boza, Abdellatif Chouai, Kim R. Dunbar, and Claudia Turro. Ultrafast Ligand Exchange: Detection of a Pentaco-ordinate Ru(II) Intermediate and Product Formation. *Journal of the American Chemical Society*, 131(1):26–27, January 2009.

[199] Maria Ekimova, Wilson Quevedo, Manfred Faubel, Philippe Wernet, and Erik T. J. Nib-bering. A liquid flatjet system for solution phase soft-x-ray spectroscopy. *Structural Dynamics*, 2(5):054301, August 2015.

[200] Jake D. Koralek, Jongjin B. Kim, Petr Brůža, Chandra B. Curry, Zhijiang Chen, Hans A. Bechtel, Amy A. Cordones, Philipp Sperling, Sven Toleikis, Jan F. Kern, Stefan P. Moeller, Siegfried H. Glenzer, and Daniel P. DePonte. Generation and characterization of ultrathin free-flowing liquid sheets. *Nature Communications*, 9(1):1353, April 2018.

Oliviero Cannelli
Curriculum Vitae

EPFL SB ISIC LSU - CH H1 535
1015 Lausanne, Switzerland
☎ (+41) 21 693 04 56
✉ oliviero.cannelli@epfl.ch
date of birth: 07/05/1992

Current Research Interest and Experience

Physical Chemistry, Condensed Phase Dynamics, Solar Materials and Light Harvesting Photo-Physics, Excited State Dynamics, Molecular Physics, (Bio)Chemical Reaction Dynamics, Ultrafast Optical Pump-Probe Spectroscopy, Ultrafast X-Ray Techniques

---

Education and Related Activities

January 2017-Present	**PhD in Physics**, *École Polytechnique Fédérale de Lausanne (EPFL)*, *Supervisor: Prof. Majed Chergui, EPFL, Co-supervisor: Prof. Giulia F. Mancini, University of Pavia.*
October 2016	**Specialized II Cycle Diploma**, *Scuola Normale Superiore (SNS), Pisa.*
October 2016	**Master degree in Physical Chemistry (110/110 cum laude)**, *University of Pisa, Supervisor: Prof. Chiara Cappelli, SNS.*
July 2014	**Bachelor degree in Chemistry (110/110 cum laude)**, *Sapienza*, University of Rome, *Supervisor: Prof. Robertino Zanoni, Sapienza - University of Rome.*
July 2011	**Scientific high school diploma (100/100)**, *Liceo Terenzio Mamiani, Rome.*

Prizes and Remarks

June 2021	**Journal of the American Chemical Society Supplementary Cover**, *Quantifying Photoinduced Polaronic Distortions in Inorganic Lead Halide Perovskites Nanocrystals.*
November 2019	**Structual Dynamics Cover**, *Toward time-resolved laser T-jump/X-ray probe spectroscopy in aqueous solutions.*
September 2019	**Swiss Chemical Society Fall Meeting**, *Best Oral Presentation.*
December 2017	**Scuola Normale Superiore**, *Official Speaker Graduation Cerimony.*
October 2014	**Scuola Normale Superiore scholarship**, *National Competition*, Scuola Normale Superiore di Pisa, *Scholarship Duration: Two Years.*
October 2011	**PLS scholarship award (National Program scientific degrees)**, *National Competition*, Italian Chemical Society, *Scholarship Duration: Three Years.*

Publications

O. Cannelli, N. Colonna, M. Puppin, T. Rossi, D. Kinschel, L. Leroy, J. Loeffler, A. M. March, G. Doumy, A. Al Haddad, M.-F. Tu, Y. Kumagai, D. Walko, G. Smolentsev, F. Krieg, S. C. Boehme, M. V. Kovalenko, M. Chergui, G. F. Mancini, "Quantifying Photoinduced Polaronic Distortions in Inorganic Lead Halide Perovskites Nanocrystals", *Journal of the American Chemical Society*, 143, 24, (**2021**).
Editor's Highlight and cover

C. Bacellar, D. Kinschel, **O. Cannelli**, B. Sorokin, T. Katayama, G. F. Mancini, J. R. Rouxel, Y. Obara, J. Nishitani, H. Ito, T. Ito, N. Kurahashi, C. Higashimura, S. Kudo, C. Cirelli, G. Knopp, K. Nass, P. J. M. Johnson, A. Wach, J. Szlachetko, F. A. Lima, C. J. Milne, M. Yabashi, T. Suzuki, K. Misawacand, M. Chergui, "Femtosecond X-ray spectroscopy of haem proteins", *Faraday Discussions*, 228, (**2021**).

O. Cannelli, T. Rossi, D. Kinschel, J. Budarz, J. Löffler, A. M. March, G. Doumy, A. Al Haddad, M.-F. Tu, Y. Kumagai, D. Walko, G. Smolentsev, F. Krieg, M. V. Kovalenko, G. F. Mancini, and M. Chergui, "Element-Selective Probing of Photo-Driven Structural Changes in All-Inorganic Lead Perovskites", *International Conference on Ultrafast Phenomena* (**2020**).

C. Bacellar, D. Kinschel, G. F. Mancini, R. A. Ingle, J. Rouxel, **O. Cannelli**, C. Cirelli, G. Knopp, J. Szlachetko, F. A. Lima, S. Menzi, G. Pamfilidis, K. Kubicek, D. Khakhulin, W. Gawelda, A. Rodriguez-Fernandez, M. Biednov, C. Bressler, C. A. Arrell, P. J. M. Johnson, C. Milne, and M. Chergui, "Heme Doming in Ferric Cytochrome c: Femtosecond X-ray Absorption and X-ray Emission Studies", *International Conference on Ultrafast Phenomena* (**2020**).

D. Kinschel, C. Bacellar, **O. Cannelli**, B. Sorokin, T. Katayama, G. F. Mancini, J. R. Rouxel, Y. Obara, J. Nishitani, H. Ito, T. Ito, N. Kurahashi, C. Higashimura, S. Kudo, T. Keane, F. A. Lima, W. Gawelda, P. Zalden, S. Schulz, J. M. Budarz, D. Khakhulin, A. Galler, C. Bressler, C. J. Milne, T. Penfold, M. Yabashi, T. Suzuki, K. Misawa, M. Chergui, "Femtosecond X-ray emission study of the spin cross-over dynamics in haem proteins", *Nature Communications*, 11, 4145 (**2020**).
Editor's Highlight

C. Bacellar, D. Kinschel, G. F. Mancini, R. A. Ingle, J. Rouxel, **O. Cannelli**, C. Cirelli, G. Knopp, J. Szlachetko, F. A. Lima, S. Menzi, G. Pamfilidis, K. Kubicek, D. Khakhulin, W. Gawelda, A. Rodriguez-Fernandez, M. Biednov, C. Bressler, C. A. Arrell, P. J. M. Johnson, C. J. Milne, M. Chergui, "Spin cascade and doming in ferric hemes: Femtosecond X-ray absorption and X-ray emission studies", *Proceedings of the National Academy of Sciences*, 117.36, 21914-21920 (**2020**).

T. C. Rossi, D. Grolimund, **O. Cannelli**, G. F. Mancini, C. Bacellar, D. Kinschel, J. R. Rouxel, N. Ohannessian, D. Pergolesi and M. Chergui, "X-ray absorption linear dichroism at the Ti K-edge of rutile (001) TiO_2 single crystal", *Journal of Synchrotron Radiation*, 27.2, 425-435 (**2020**).

O. Cannelli, C. Bacellar, R. A. Ingle, R. Bohinc, D. Kinschel, B. Bauer, D. S. Ferreira, D. Grolimund, G. F. Mancini, M. Chergui, "Toward time-resolved laser T-jump/X-ray probe spectroscopy in aqueous solutions", *Structural Dynamics*, 6.6, 064303 (**2019**).
Editor's Highlight and cover

E. Baldini, A. Dominguez, T. Palmieri, **O. Cannelli**, A. Rubio, P. Ruello M. Chergui, "Exciton control in a room temperature bulk semiconductor with coherent strain pulses", *Science Advances*, 5.11, eaax2937 (**2019**).

T. C. Rossi, D. Grolimund, M. Nachtegaal, **O. Cannelli**, G. F. Mancini, C. Bacellar, D. Kinschel, J. R. Rouxel, N. Ohannessian, D. Pergolesi, T. Lippert, M. Chergui, "X-ray absorption linear dichroism at the Ti K edge of anatase TiO_2 single crystals", *Physical Review B*, 100.24, 245207 (**2019**).

B. Carlotti, A. Cesaretti, **O. Cannelli**, T. Giovannini, C. Cappelli, C. Bonaccorso, C. G. Fortuna, F. Elisei, A. Spalletti, "Evaluation of Hyperpolarizability from the Solvatochromic Method: Thiophene Containing Push–Pull Cationic Dyes as a Case Study", *The Journal of Physical Chemistry C*, 122.4, 2285–2296 (**2018**).

O. Cannelli, T. Giovannini, A. Baiardi, B. Carlotti, F. Elisei, C. Cappelli, "Understanding the interplay between the solvent and nuclear rearrangements in the negative solvatochromism of a push–pull flexible quinolinium cation", *Physical Chemistry Chemical Physics*, 19.48, 32544-32555 (**2017**).

A. Motta, **O. Cannelli**, A. Boccia, R. Zanoni, M. Raimondo, A. Caldarelli, F. Veronesi, "A Mechanistic Explanation of the Peculiar Amphiphobic Properties of Hybrid Organic–Inorganic Coatings by Combining XPS Characterization and DFT Modeling", *ACS applied materials & interfaces*, 7.36, 19941–19947 (**2015**).

Oral Presentations

June 2020 **MUST - Final Review Panel**, *"Towards time-resolved laser T-jump/X-ray absorption probe spectroscopy"*, Online, *Switzerland*.

November 2019 **Seminar@ELETTRA**, *"Towards time-resolved laser T-jump/X-ray absorption probe spectroscopy"*, Trieste, *Italy*.
Invited Talk

September 2019 **SXR2019 - Beating the Complexity of Matter through the Selectivity of X-rays - Dynamic Pathways in Multidimensional Landscapes**, *"Towards time-resolved laser T-jump/X-ray absorption probe spectroscopy"*, Berlin, *Germany*.

September 2019 **Swiss Chemical Society Fall Meeting 2019**, *"Towards time-resolved laser T-jump/X-ray absorption probe spectroscopy"*, Zurich, *Switzerland*.

July 2018 **XAFS - 17th International Conference on X-ray Absorption Fine Structure**, *"Element-selective probing of the photo-induced charge carriers in inorganic lead perovskites"*, Krakow, *Poland*.

Poster Presentations

February 2021 **Time resolved imaging of photo-induced dynamics: Faraday Discussion**, *"Quantifying Photoinduced Polaronic Distortions in Inorganic Lead Halide Perovskites Nanocrystals"*, Online, *UK*.

November 2020 **UP2020**, *"Element-Selective Probing of Photo-Driven Structural Changes in All-Inorganic Lead Perovskites"*, Online, *China*.

June 2019 **ICUSD**, *"Towards time-resolved laser T-jump X-ray absorption probe spectroscopy"*, Daejeon, *South Korea*.

February 2019 **LACUS Day**, *"Towards time-resolved laser T-jump X-ray absorption probe spectroscopy"*, Lausanne, *Switzerland*.

November 2018 **ISUS**, *"Time-resolved element selective probing of photo-induced charge carriers in inorganic lead perovskites"*, Lausanne, *Switzerland*.

September 2018 **SCS Fall Meeting**, *"Time-resolved element selective probing of photo-induced charge carriers in inorganic lead perovskites"*, Lausanne, *Switzerland*.

Selected Large Scale Facility Experiments

November 2019	**Free Electron laser Radiation for Multidisciplinary Investigations (FERMI)**, *"Charge carrier dynamics in spinel Co_3O_4 probed by resonant EUV transient grating spectroscopy"*, Trieste, *Italy*.
October 2019	**European X-ray Free-Electron Laser (EXFEL)**, *"Single-shot visualization of the multi-centre ultrafast response in photoexcited spinel Co_3O_4 by femtosecond non-resonant XES and diffraction"*, Hamburg, *Germany*.
January 2019	**SwissFEL**, *"Energy vs Electron Transfer Tryptophan-to-Heme in Cytochrome C"*, Villigen, *Switzerland*.
April 2018	**Swiss Light Source (SLS)**, *"Establishing the laser T-jump approach for picosecond hard X-ray absorption studies of (bio) chemical reactions"*, Villigen, *Switzerland*.
December 2017	**SPring-8 Angstrom Compact Free Electron Laser (SACLA)**, *"Correlated spin and structural dynamics in the recombination of nitric oxide (NO) to deoxy-Myoglobin in physiological media"*, Hyogo, *Japan*.
June 2017	**Advanced Photon Source (APS)**, *"Mapping photoinduced charge carrier dynamics in inorganic perovskite semiconductor nanoparticles using time-resolved X-ray absorption and emission spectroscopies"*, Argonne, *Illinois (USA)*.

Teaching Experience

General Physics III (Electromagnetism), General Physics IV (Quantum Mechanics), Electronic Spectroscopy, Ultrafast Phoenomena

Languages

Italian	Native
English	Advanced
French	Intermediate
German	Beginner

Computer Skills

Programming Languages	Python, Matlab, Bash
Typesetting	MS Office, LaTeX
Operating Systems	Windows, Mac OS X, Linux